

# Search for Terrestrial Gamma-ray Flashes in AGILE data by correlation with ground-based lightning measurements

Master Thesis in Space Physics  
by  
Anders Lindanger



Department of Physics and Technology  
University of Bergen  
Norway

June 1, 2018



# Acknowledgements

First and foremost I want to thank my supervisor Associate Professor Martino Marisaldi for excellent guidance, support, and inspiration. I always found his office door to be open. I would also like to thank Kjetil Albrechtsen, Professor Nikolai Østgaard, and Professor Kjellmar Oksavik for additional support and excellent advice during these two years.

Furthermore, I'd like to thank the AGILE Science Data Center and the World Wide Lightning Location Network for providing the data used in this thesis.

I thank my fellow students Chris, Daniel, Helge, Håkon, Karl, Magnus and Viljar for coordinated breaks and lots of good stories through five years of studies. I would also like to thank Astrid, Bjørn, Helene, Kristian, Nini, Ragnar, and Roger.

Finally, I would like to thank Christina and my family for their support, inspiration, and understanding.

Anders Lindanger  
Bergen, 01.06.2018



# Abstract

Terrestrial Gamma-ray Flashes (TGFs) are sub-millisecond bursts of high energy photons, associated with lightning flashes produced inside thunderstorms. The Astro-Rivelatore Gamma a Immagini Leggero (AGILE) satellite is one of the few satellites capable of detecting these events.

Comparing gamma-ray measurements by AGILE and lightning detected by the World Wide Lightning Location Network (WWLLN), it is possible to identify TGF candidates based only on time correlation between gamma-ray and lightning data. This new algorithm is not biased by previous selection criteria, e.g. spectral hardness ratio, and can therefore find new candidates which have been overlooked before. Similar procedures have already been successfully applied to data from the Fermi and RHESSI satellites. The ultimate goal is to contribute to answering the question: how common are TGFs?

Using five different datasets collected by the Mini-Calorimeter (MCAL) and the Gamma-ray Imaging Detector (GRID), between January 2008 and April 2018, a list of new TGF candidates has been obtained. The datasets are differentiated by detector attributes and variable timing accuracy. Due to a degradation of the onboard GPS timing accuracy in July 2015, the absolute timing accuracy went from  $\mu\text{s}$  to  $\text{ms}$  level. By assuming perfect time correlation between the WWLLN match and the TGF, these TGF candidates are used to improve the  $\text{ms}$  timing accuracy of the AGILE data after 2015 to  $\sim 100\mu\text{s}$ . A total of 439 TGF candidates are identified in the MCAL data between 23.03.15 - 14.04.18, where 396 of them are not published before.



# List of Abbreviations

<b>AC</b>	Anti-coincidence (system)
<b>ADELE</b>	The Airborne Detector for Energetic Lightning Emission
<b>AGILE</b>	Astro-rivelatore Gamma a Immagini LEggero
<b>ASDC</b>	AGILE Science Data Center
<b>ASIM</b>	Atmosphere-Space Interactions Monitor
<b>BATSE</b>	Burst and Transient Source Experiment
<b>BGO</b>	Bismuth Germanate Oxide
<b>CA</b>	Cloud to Air (lightning)
<b>CC</b>	Cloud to cloud (lightning)
<b>CG</b>	Cloud to ground (lightning)
<b>CGRO</b>	Compton Gamma-Ray Observatory
<b>CZT</b>	Cadmium Zinc Telluride
<b>EIWG</b>	Earth-Ionospheric waveguide
<b>FOV</b>	Field Of View
<b>GRBM</b>	Gamma-ray Burst Monitor (BeppoSAX)
<b>GBM</b>	Gamma-ray Burst Monitor (Fermi)
<b>GRB</b>	Gamma-ray bursts
<b>GRID</b>	Gamma-Ray Imaging Detector
<b>HF</b>	High Frequency
<b>IC</b>	Intra cloud (lightning)
<b>ISS</b>	International Space Station
<b>LAD</b>	Large Area Detectors
<b>LF</b>	Low Frequency
<b>MCAL</b>	Mini-Calorimeter
<b>MF</b>	Medium Frequency
<b>NLDN</b>	National Lightning Detection Network
<b>RHESSI</b>	Reuven Ramaty High Energy Solar Spectroscopic Imager

**SD** Spectroscopy Detector

**Super-AGILE** Hard X-ray Imager

**TGF** Terrestrial gamma-ray flash

**TOA** Time of arrival

**TOGA** Time Of Group Arrival

**TRMM-LIS** Tropical Rainfall Measuring Mission Lightning Imaging Sensor

**VLF** Very Low Frequency

**WWLLN** World Wide Lightning Location Network



# Contents

<b>1</b>	<b>Introduction</b>	<b>9</b>
<b>2</b>	<b>Theory</b>	<b>11</b>
2.1	Thunderclouds . . . . .	11
2.1.1	Lightning Discharges . . . . .	12
2.2	Streamers and Leaders . . . . .	12
2.2.1	Streamers . . . . .	13
2.2.2	Leaders . . . . .	13
2.3	Lightning Detection by Radio Waves . . . . .	14
2.4	Production of Terrestrial Gamma-Ray Flashes . . . . .	14
2.4.1	Runaway Electrons . . . . .	14
2.4.2	Relativistic Runaway Electron Avalanches . . . . .	15
2.4.3	Relativistic Feedback Mechanism . . . . .	16
2.4.4	Thermal Runaway Mechanism . . . . .	17
<b>3</b>	<b>Observations of Terrestrial Gamma-ray Flashes</b>	<b>19</b>
3.1	BATSE . . . . .	20
3.2	RHESSI . . . . .	21
3.3	AGILE . . . . .	21
3.4	Fermi . . . . .	22
3.5	ADELE . . . . .	22
3.6	ASIM . . . . .	22
3.7	Others . . . . .	23
3.8	TGF correlation to ground-detected lightning . . . . .	23
3.9	TGF source altitudes and energy spectrum . . . . .	24
<b>4</b>	<b>Instruments and Datasets</b>	<b>27</b>
4.1	The World Wide Lightning Location Network . . . . .	27
4.2	The AGILE mission and Detectors . . . . .	29
4.2.1	The Anti-Coincidence system . . . . .	29
4.2.2	The Mini-Calorimeter . . . . .	30
4.2.3	The Gamma-Ray Imaging Detector . . . . .	31
4.3	The AGILE datasets . . . . .	31
4.3.1	GRID period . . . . .	32
4.3.2	AC-ON period . . . . .	32
4.3.3	REF period . . . . .	32
4.3.4	DRIFT period . . . . .	32
4.3.5	3D-FIX period . . . . .	33
4.4	Satellite position . . . . .	34
<b>5</b>	<b>Method</b>	<b>37</b>

5.1	Reduction of dataset size . . . . .	37
5.2	Propagation time of photons associated to TGF . . . . .	40
5.2.1	Propagation time accuracy . . . . .	41
5.3	Stacking analysis . . . . .	43
5.4	Search for clusters . . . . .	44
5.5	Expected number of WWLLN detections in the TGF field of view, and distance from sub-satellite point . . . . .	46
5.5.1	Expected number of WWLLN detections in the TGF field of view . . . . .	46
5.5.2	Distance between WWLLN detection and sub-satellite point . . . . .	47
<b>6</b>	<b>Results and Discussions</b>	<b>49</b>
6.1	GRID period . . . . .	49
6.1.1	Stacking analysis . . . . .	50
6.1.2	Distance between the sub-satellite point and WWLLN detections . . . . .	50
6.1.3	Reconstruction of particle direction . . . . .	51
6.2	AC-ON period . . . . .	52
6.2.1	Stacking analysis . . . . .	53
6.2.2	Distance between the sub-satellite point and WWLLN detections . . . . .	54
6.3	REF period . . . . .	55
6.3.1	Stacking analysis . . . . .	55
6.3.2	Identifying TGFs using the search for cluster analysis . . . . .	57
6.3.3	Distance between the sub-satellite point and WWLLN detections . . . . .	59
6.3.4	TGF-lightning ratio in the REF period . . . . .	61
6.3.5	Timing offset analysis . . . . .	62
6.4	DRIFT period . . . . .	63
6.4.1	Stacking analysis . . . . .	64
6.4.2	Identifying TGFs using the search for cluster analysis . . . . .	64
6.4.3	Distance between the sub-satellite point and WWLLN detections . . . . .	66
6.4.4	Comparing the background in REF and DRIFT periods . . . . .	67
6.4.5	Timing offset analysis . . . . .	70
6.5	3D-FIX period . . . . .	71
6.5.1	Identifying TGFs using the search for cluster analysis . . . . .	72
6.5.2	Timing offset analysis . . . . .	73
6.6	Global and monthly distribution of all TGF candidates . . . . .	75
<b>7</b>	<b>Summary and Outlook</b>	<b>79</b>

# Chapter 1

## Introduction

Terrestrial Gamma-ray Flashes (TGF) are sub-millisecond bursts of very energetic photons (up to  $\sim 40$  MeV) produced in the Earth's atmosphere, and associated to lightning flashes and thunderstorm activity [Dwyer *et al.*, 2012]. The first TGFs were observed by the Compton Gamma-ray Observatory (CGRO) in 1991. While looking for cosmic gamma-ray bursts, it also detected short-duration gamma-ray bursts originating from the Earth. These findings were reported by Fishman *et al.* [1994], who also linked the gamma-ray bursts to thunderstorm activity.

CGRO detected on average less than one TGF per month during its nine years of operation. It detected only very bright TGFs as the detector trigger window was long compared to the typical sub-millisecond duration of TGFs. In 2002, the Reuven Ramaty High Energy Solar Spectroscopic Imager (RHESSI) was launched to study solar flares, but also detected 0.43 TGFs per day during the first years of operation [Grefenstette *et al.*, 2009].

In 2008, the satellite Fermi was launched. The first Fermi TGF catalog reports an average detection rate of 2.2 TGFs per day [Roberts *et al.*, 2018].

As TGFs seem to be correlated with lightning flashes, and there are approximately 45 lightning discharges per second on Earth [Rakov and Uman, 2003, p. 43], TGFs were viewed as a rare phenomena with a very low TGF-lightning ratio. However, Østgaard *et al.* [2012] suggested, using data from RHESSI and Fermi, that there might be a weak population of TGFs not yet detected from space, due to e.g., the satellite's low sensitivity. They suggested that maybe all lightning flashes produce a TGF.

There are two methods in TGF searching algorithms. The first is based on standard selection criteria, e.g. spectral hardness ratio, using gamma-ray data only. The second is based on time correlation of satellite counts with radio waves from lightning discharges. The first approach biases the TGF population towards bright events, possibly neglecting observationally faint TGFs. However, the last approach is dependent on having an associated lightning detection, detected by a ground-based lightning network. The last approach has been applied to both the RHESSI and Fermi data, identifying new weak TGFs which have been overlooked by previous standard search algorithms [Østgaard *et al.*, 2015; Smith *et al.*, 2016]. Although new TGFs were identified, Smith *et al.* [2016] concluded that a large population of weak TGFs is improbable.

The Astro-Rivelatore Gamma a Immagini Leggero (AGILE), launched in 2007 and dedicated to gamma-ray astrophysics, is able to detect up to 3 TGFs per day, using standard selection algorithms [Marisaldi *et al.*, 2015]. However, a lightning based search for TGFs has not been systematically applied to the AGILE datasets. This is the aim of this thesis.

The new TGFs, identified by correlation with lightning detections, will not be biased by previous selection criteria, and will provide a basis for developing better search algorithms in the future.

This thesis will provide a detailed analysis of five different AGILE datasets between January 2008 and April 2018, differentiated by detector type and onboard timing accuracy, which deteriorated from  $\mu\text{s}$  level to ms accuracy, due to a degradation of the onboard GPS in July 2015. A detailed description of the AGILE datasets is found in Section 4.3.

A TGF candidate is defined as a burst of photons associated  $\pm 500 \mu\text{s}$  with respect to the lightning detection, corrected for the propagation time of the photons. A total of 439 TGF candidates are identified between 23.03.15 and 14.04.18, where 396 of them have not been published before.

The TGFs, identified after the degradation of the onboard GPS, are used successfully to improve the satellite onboard timing accuracy from several ms accuracy to  $\sim 100 \mu\text{s}$ , assuming a perfect correlation with the associated lightning detections.

Plots and lists of the 439 TGF candidates identified, are found in the open git repository "[https://github.com/andersbhm/Software\\_master\\_thesis](https://github.com/andersbhm/Software_master_thesis)", together with software written during this thesis.

This thesis is structured as follows: Chapter 2 and 3 introduce the theory and describes the space missions leading to the discovery of TGFs. Chapter 4 describes the instruments and outlines the different datasets. Chapter 5 explains the methods developed to identify the TGFs. Chapter 6 discusses and presents the results of the analysis, and Chapter 7 provides a summary and ideas for future work.

# Chapter 2

## Theory

This chapter will present the theoretical background necessary to understand this thesis, namely; thunderclouds, lightning flashes, lightning detection by radio waves, and the production mechanisms of Terrestrial Gamma-ray Flashes. As thunderclouds and lightning flashes themselves are not the main topic of this thesis, we will just provide a short introduction.

### 2.1 Thunderclouds

Clouds are generally composed of ice crystals and water droplets. The forming of fair-weather clouds occur when rising warm air cools faster than the surrounding air. When the air cools, the moisture in the air condensates and forms water droplets. A thundercloud develops from a fair-weather cloud when the rising air cools *slower* than the surroundings. This happens when the rising air is sufficiently moist. Also, the decrease in the ambient temperature with altitude needs to get cooler by at least  $6\text{ }^{\circ}\text{C}/\text{km}$ . As the temperature decreases with altitude in the troposphere, and starts to increase in the stratosphere, the tropopause generally marks the upper limit for a thundercloud. The tropopause altitude varies between 8 km and 18 km, depending on season and latitude [Rakov and Uman, 2003, p. 68].

As the temperature decreases with altitude, the water particles go through different phases. Between  $0\text{ }^{\circ}\text{C}$  and  $-40\text{ }^{\circ}\text{C}$ , some particles start to freeze, and some remain supercooled up to  $-40\text{ }^{\circ}\text{C}$ . All particles are frozen below  $-40\text{ }^{\circ}\text{C}$ . When supercooled water particles collide with ice crystals, they can freeze on impact. These particles are called graupels and grow from  $\mu\text{m}$  to cm scale. When the graupels grow, they start to fall due to their increased mass. The falling graupels then collide with rising ice and supercooled particles, following the warm air updraft, and become charged through the triboelectric effect. The triboelectric effect is the electrical charging of materials when they are in frictional contact with each other.

Based on the experiments by Takahashi [1978] and Jayaratne *et al.* [1983], graupels are considered the most likely source of charge generation in thunderclouds. The experiments show that charge and polarity are dependent mainly on water content and temperature. The experiments could predict the typical polarity of charge regions at a given temperature in a thundercloud.

The charge distribution in thunderclouds is often approximated using a simple tripole model, illustrated in Figure 2.1. The reality is more complicated, but the tripole model is

generally accepted as a good approximation [Williams, 1989]. The tripole model consists of an upper positive (UP) charge layer, a main negative (MN) charge layer, and a low positive (LP) charge layer. The UP charge layer and the MN charge layer have the same charge magnitude, and the LP charge layer has a much lower charge magnitude.

According to *Rakov and Uman* [2003], p. 83, the maximum electric field measured in thunderclouds are in the range 1 kV/cm to 4 kV/cm. The measurements are done using a balloon or an aircraft.

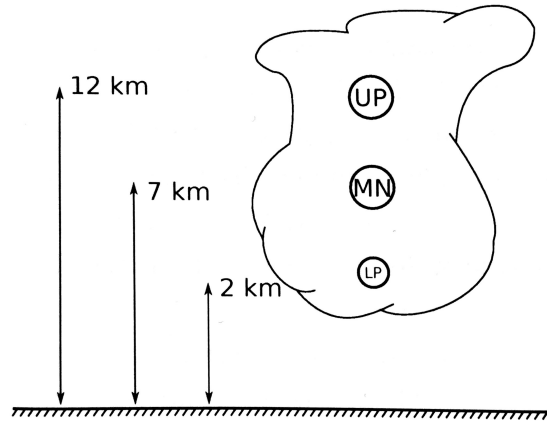


Figure 2.1: Illustration of the tripole model. Figure from *Skeltved* [2018].

### 2.1.1 Lightning Discharges

We will use the following terminology in this thesis: A lightning discharge, whether it strikes the ground or not, is termed a lightning flash. A lightning flash that involves an object in the atmosphere or the ground, is termed a lightning strike.

Lightning flashes can be divided into four groups: cloud-to-ground (CG) lightning, intra cloud (IC) lightning, cloud-to-cloud (CC) lightning and cloud-to-air (CA) lightning. *Rakov and Uman* [2003], p. 4, states that roughly 75 % of Earth’s lightning are IC lightning. The remaining lightning flashes are mainly CG, while CC and CA are rare. It is the +IC lightning that is most likely related to TGFs observed from space [*Shao et al.*, 2010; *Lu et al.*, 2010]. This lightning discharge typically develops from the MN charge region toward the UP charge region.

## 2.2 Streamers and Leaders

An essential part of discharge theory is the so-called streamers and leaders. Streamers and leaders are related to the mechanisms of discharge processes and the initiation of lightning flashes.

*Rakov and Uman* [2003], p. 5, define the difference between leaders and streamers as follows: "Any self-propagating electrical discharge creating a channel with an electrical conductivity of the order of  $10^4$  S/m (comparable to that of carbon) is called a leader. Streamers, on the other hand, are characterized by much lower electrical conductivity; the air behind the streamer tip remains essentially an insulator."

### 2.2.1 Streamers

The process of streamer developing starts with an electron avalanche. The energy of an electron increase with the electric field strength. An electron avalanche may start if the energy of an electron is larger than the ionization energy of air. ( $\sim 12$  eV for oxygen and  $\sim 16$  eV for nitrogen.) Inelastic collisions between the electrons and atoms may excite or ionize the atoms. If the number of ionizing collisions is larger than the number of electron attachments, there is an electron avalanche. In an electron avalanche, the number of electrons, as a function of distance, is given by

$$n = e^{(\alpha-\eta)z} \quad (2.1)$$

where  $n$  is the number of electrons,  $\alpha$  is the number of ionizing collisions per unit length,  $\eta$  is the number of attachments per unit length, and  $z$  is the distance along the electric field. The electric field required for  $\alpha = \eta$  is called the conventional breakdown threshold, and is assumed to be  $E_k \approx 32$  kV/cm [Moss *et al.*, 2006].

As the number of electrons,  $n$ , increases with distance,  $z$ , the electric field of the avalanche increases. At some critical distance  $z_c$ , the local electric field of the avalanche is larger than  $E_k$ . If the local electric field of the streamer is larger than  $E_k$  at a distance  $z_c$ , the streamer is self-sustained. The number of electrons necessary to create such an electric field is known as the Raether-Meek criterion, and is in the order of  $n \approx 10^8 - 10^9$  electrons. If we assume the streamer is a point charge, we obtain the critical distance,  $z_c$ , by the equation

$$\frac{1}{4\pi\epsilon_0} \frac{ne}{z_c^2} = E_k \quad (2.2)$$

where  $n = 10^8$ ,  $E_k = 32$  kV/cm,  $e$  is the elementary charge and  $\epsilon_0$  is the permittivity of free space. Solving for  $z_c$ , we get 200  $\mu\text{m}$ , which is the boundary of the streamer's active region.

If the electric field increases, the number of streamers increases. This forms the start of a leader channel.

### 2.2.2 Leaders

As each streamer is weakly conductive and their current is low, they have to increase in numbers to turn into a leader channel. Then their combined conductivity and current will form a conductive channel. This is the case in a sufficiently high electric field.

*Raizer* [1991] p. 364 defines a leader as a thin, highly ionized, highly conductive channel that grows along a path prepared by preceding streamers. He also states that "The leader head, like a metallic tip, is a source of exceptionally strong electric field and thus sends out streamers that fan out and prepare the initial electron density."

It is a leader that is visible during a CG lightning flash. The highly conducting channel transports charge between the cloud and the ground, due to the potential difference.

## 2.3 Lightning Detection by Radio Waves

Lightning flashes emit electromagnetic waves in a wide range of frequencies. The radio waves emitted are often referred to as "sferics". The frequency range of sferics is typically Very Low Frequency (VLF) but can extend up to Low Frequency (LF) and above [Rakov and Uman, 2003, p. 432]. These sferics are possible to measure at great distances because the Earth's ionosphere acts as a wave guide, meaning that the radio waves are reflected between the ionosphere and Earth's surface. The ionosphere ranges from  $\sim 60$  km to  $\sim 1000$  km, and consists of particles ionized by the radiation from the Sun. The radio waves propagating along the Earth-Ionospheric waveguide (EIWG) are called skywaves, and waves that propagate along the surface of the Earth, are called groundwaves. Skywaves use more time, as they propagate over a longer distance.

The lightning location can be triangulated based on the difference in time of arrival (TOA). The TOA is determined by the first microseconds of the sharp wave train, associated with groundwaves. The Medium Frequency (MF) band is used to avoid the skywaves in the VLF band arriving slightly later. As groundwaves do not travel long distances, a dense network of ground stations separated by a few hundred km at the most, is needed [Dowden *et al.*, 2002]. Location accuracy down to a few hundred meters is possible.

The highest power spectral density of lightning radiation is in the VLF band (3 - 30 kHz). VLF waves propagate thousands of km as skywaves, and are therefore possible to detect easily with a lightning network much less dense than groundwave networks working in the MF band. The problem arises as the initial sharp pulse of the lightning flash disperses as it travels through the EIWG, leading to no sharp onset of the wavefront, leading to low timing accuracy, and therefore low location accuracy. The World Wide Lightning Location Network (WWLLN) solves this by using the whole dispersed wave train, and measures the rate of change of the spheric phase with respect to frequency, to find the so-called time of group arrival (TOGA). They define the TOGA as the instant when the least squares regression line of phase, as a function of frequency, over a specified band, has zero slope. For a lightning flash to be detected by WWLLN, it needs to be detected by at least five separate stations [Dowden *et al.*, 2002].

## 2.4 Production of Terrestrial Gamma-Ray Flashes

### 2.4.1 Runaway Electrons

C.T.R. Wilson discovered in 1924 that electrons might obtain high energies from static electric fields in air [Wilson, 1924]. This is when the force from an electric field exceeds the friction force the electron experiences due to collisions. This is called the runaway electron mechanism.

The friction force in air is dependent on the kinetic energy of the electron. In Figure 2.2, the kinetic energy of the electron is on the x-axis and the friction force experienced by the electron is on the y-axis. The solid horizontal line, associated with  $eE$ , is the rate of energy gain from a strong electric field. For an electron to runaway it needs an initial energy larger than  $\varepsilon_{th}$  in this scenario. These electrons are called "seed electrons" and may originate from radioactive decay or cosmic rays. It is clear that  $\varepsilon_{th}$  rapidly decreases with increasing electric field. If the electric field is equal to the so-called thermal runaway threshold,  $E_c$ , all free electrons will run away. The minimum electric field needed to sustain



runaway electrons is called the break-even field. The theoretical value of the break-even field is  $E_b = 2.18 \text{ kV/cm}$ .

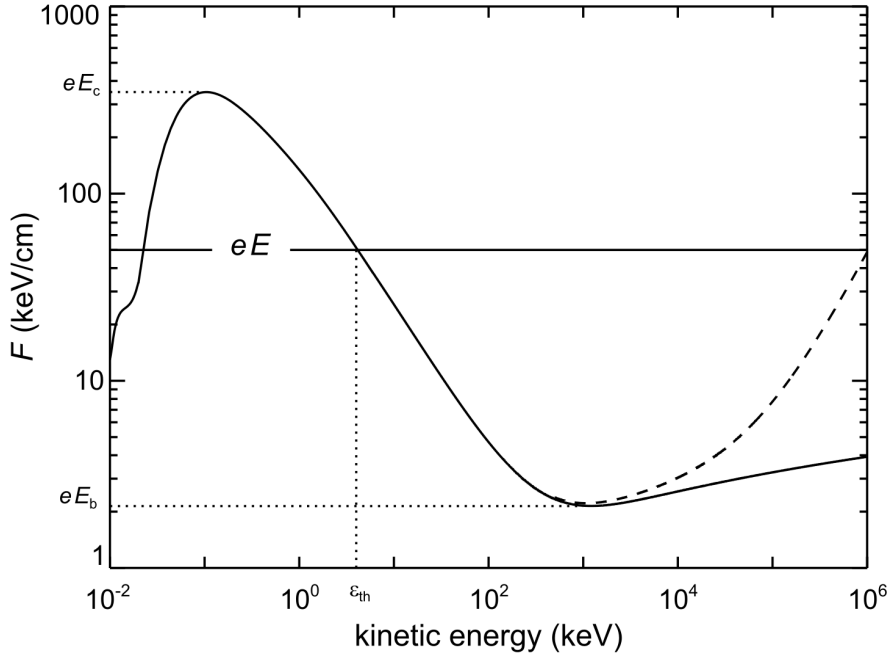


Figure 2.2: The dynamic friction force,  $F$ , of electrons in air at ground pressure. The dashed line to the right indicates effects of bremsstrahlung emission. This is a simplification of a figure in *Moss et al.* [2006]. Figure from *Dwyer et al.* [2012].

## 2.4.2 Relativistic Runaway Electron Avalanches

Relativistic runaway electron avalanches (RREA) occur when the runaway electrons undergo avalanche multiplication due to Møller scattering. (Møller scattering is electron-electron elastic scattering.) The scattered electron could have high enough energy and run away. This was shown by *Gurevich et al.* [1992]. *Dwyer* [2003] found, using a 3-D Monte Carlo simulation, that the break-even field is  $E_b = 2.84 \text{ kV/cm}$ , about 30 % higher than  $2.18 \text{ kV/cm}$ . Using a GEANT4 Monte Carlo code, *Skeltved et al.* [2014] are in agreement with *Dwyer* [2003]. These electric fields scale with air density, and these values refer to the density of air at sea level.  $E_b$  is comparable to the maximum electric fields measured in thunderclouds mentioned in Section 2.1.

The results of a RREA simulation is often represented using the avalanche length  $\lambda$ , also called e-folding length. The avalanche length is the length needed for a total number of electrons to increase by the number  $e$  ( $\approx 2.718$ ). The number of electrons,  $N_{RE}$ , present in an avalanche after some length,  $z$ , is approximated with Equation 2.3.

$$N_{RE} = N_0 e^{z/\lambda} \quad (2.3)$$

where  $N_0$  is the number of seed electrons, and  $z$  is the distance from the start of the avalanche. In *Dwyer* [2003]; *Dwyer et al.* [2012], the avalanche length,  $\lambda$ , is estimated as

$$\lambda \approx \frac{7.2 \text{ MeV}}{eE - F}, \quad 3 \leq E \leq 30 \text{ kV/cm} \quad (2.4)$$

where  $E$  is the electric field, and  $F = 0.276 \text{ MeV/m}$  is an approximation for the average energy loss rate experienced by the minimum ionizing electrons [Dwyer, 2003; Coleman and Dwyer, 2006]. Equation 2.4 and the results from different simulations are shown in Figure 2.3.

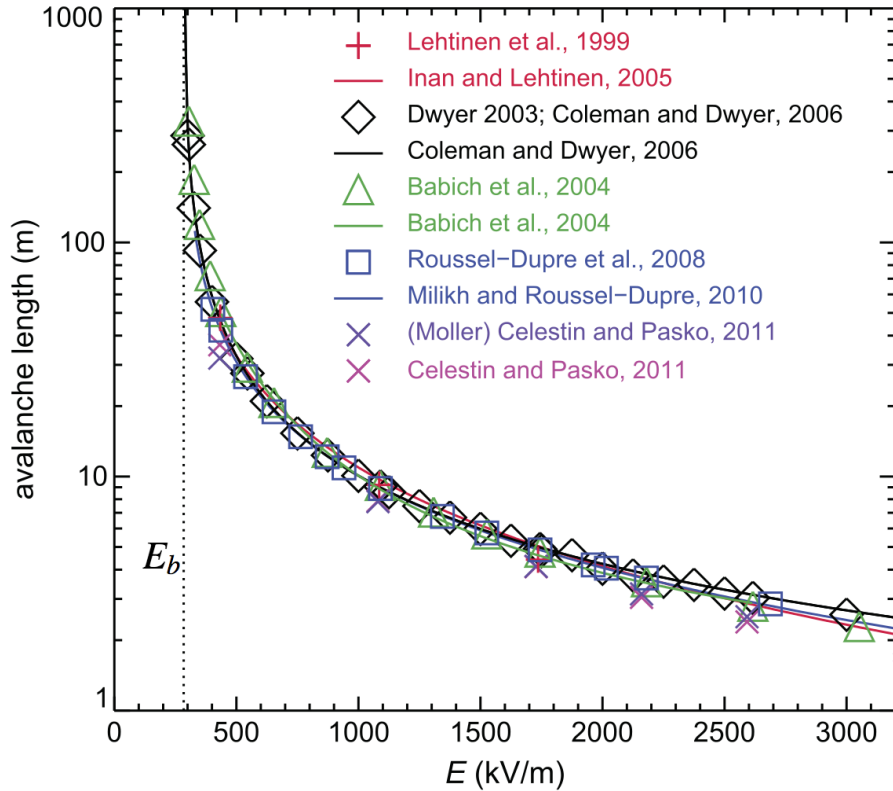


Figure 2.3: Electric field at sea level, and the avalanche length,  $\lambda$ . The data points are for several authors, and Equation 2.4 is represented as a black line. The break-even electric field,  $E_b = 2.84 \text{ kV/cm}$ , is represented as the vertical dotted line. Adapted from [Dwyer et al., 2012].

### 2.4.3 Relativistic Feedback Mechanism

The relativistic feedback mechanism was proposed by Dwyer [2003] in addition to RREA. The mechanism involves feedback effects from high energy photons and positrons, and is illustrated in Figure 2.4. The figure is partially results from a Monte Carlo simulation; A 1 MeV seed electron in  $X = 0$  and  $Z = 300$ , starts an avalanche of runaway electrons. The avalanche emits X-rays by bremsstrahlung, that may either pair-produce or Compton backscatter in air. The positrons created from the pair-production is accelerated in the opposite direction with respect to the electrons. These positrons may propagate to the start of the avalanche region and produce secondary runaway electrons. It is possible for positrons to travel several km as the positron annihilation cross-section decreases with energy, and they quickly accelerate to tens of MeV [Dwyer et al., 2012; Karwasz et al., 2002]. New electrons are produced in the avalanche region by hard elastic scattering (i.e. Bhabha scattering) with atomic electrons in air (right in Figure 2.4). A backscattered photon from the bremsstrahlung may also produce secondary electrons via Compton scattering or photoelectric absorption (left in Figure 2.4). This process repeats itself and results in more avalanches. The timescale of the relativistic feedback mechanism is in tens of microsecond [Dwyer, 2003].

The energetic seed electron, needed for the relativistic feedback mechanism to occur, may be supplied from radioactive decays, cosmic-rays, or so-called thermal runaway electrons accelerated by a local electric field higher than  $E_c$  in Figure 2.2. The thermal runaway mechanism is discussed in the next section.

*Dwyer and Smith* [2005] found that a TGF source would require a production of  $\sim 10^{16} - 10^{17}$  runaway electrons to match the measured fluences of gamma-rays at 600 km altitude. *Dwyer* [2008] argued that RREA is limited to a maximum production of  $10^5$  electrons. As the relativistic feedback mechanism is capable of increasing the number of electrons up to a factor  $10^{13}$  [*Dwyer et al.*, 2012], this mechanism is able to explain the large fluences measured from TGFs.

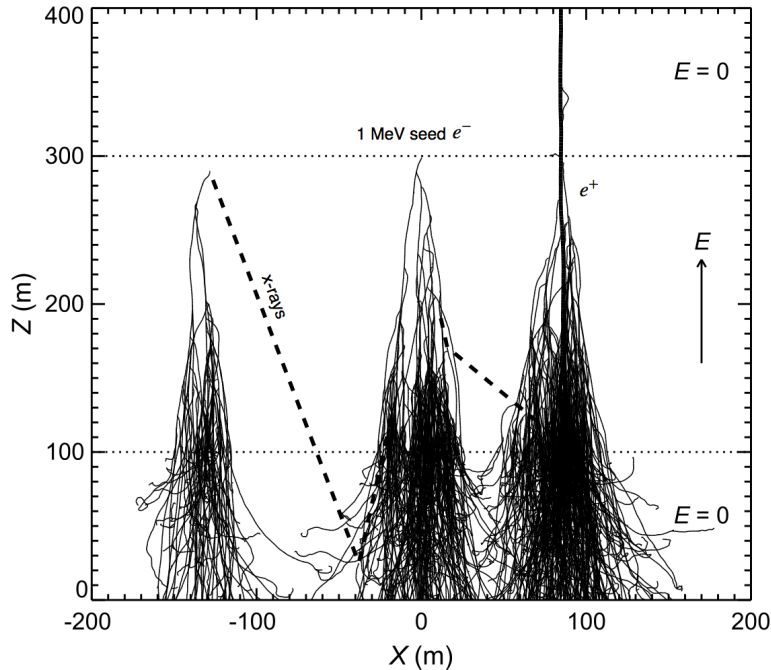


Figure 2.4: Partial results from a Monte Carlo simulation of the relativistic feedback mechanism. Light dark tracks are runaway electrons, the dark track is a positron, and the dashed lines are X-rays. The horizontal dotted lines show the boundaries of the electric field volume ( $E = 10$  kV/cm). Adapted from *Dwyer* [2003].

#### 2.4.4 Thermal Runaway Mechanism

*Moss et al.* [2006] proposed an alternative to the relativistic feedback mechanism. They found that electrons in streamer tips in front of a leader can be accelerated to energies of hundreds of keV to tens of MeV. These electrons are called thermal runaway electrons because the electric field is higher than  $E_c$  in Figure 2.2. This mechanism does not need any seed electrons as the high electric field will accelerate low energy electrons to high energies. *Celestin and Pasko* [2011], using a Monte Carlo simulation, reported runaway electrons from the streamer tip with energies up to 100 keV. Most of the electrons had an energy of 65 keV.

The number of energetic electrons in this mechanism is  $10^{17}$ , which is consistent with typical electron numbers involved in the production of TGFs [*Celestin and Pasko*, 2011]. The thermal runaway mechanism, has no need for further multiplication by the relativistic feedback mechanism discussed in the previous section.



## Chapter 3

# Observations of Terrestrial Gamma-ray Flashes

In this chapter, we will outline the discovery of TGFs, and briefly describe the space missions observing them. In Table 3.1, a summary of main characteristics of selected space missions is shown. In Figure 3.1, the effective area as a function of energy for RHESSI, AGILE and Fermi are shown. In the end, we will discuss the TGF correlation to lightning flashes, and constraints on the energy spectrum and production altitudes.

Table 3.1: Main characteristics of RHESSI, AGILE, Fermi and ASIM

	<b>RHESSI</b>	<b>AGILE MCAL</b>	<b>Fermi GBM</b>	<b>ASIM</b>
<b>Operative</b>	2002 -	2007 -	2008 -	2018 -
<b>Orbit altitude and inclination</b>	38° 600 km	2.5° 540 km	26° 540 km	51° 400 km
<b>Detector type</b>	HPGe	CsI(Tl) scintillator with solid state readout	NaI and BGO scintillator with PMT	CZT matrix and BGO scintillator with PMT
<b>Energy range</b>	0.003 - 20 MeV	0.35 - 100 MeV	0.015 - 40 MeV	0.015 - 40 MeV
<b>Effective area for typical TGF energy spectrum</b>	260 cm <sup>2</sup>	220 cm <sup>2</sup>	160 cm <sup>2</sup> (1xBGO)	900 cm <sup>2</sup>
<b>Acquisition type</b>	continuous	triggered	triggered/continuous	triggered
<b>TGFs/year</b>	~ 340	~ 800	~ 800	-

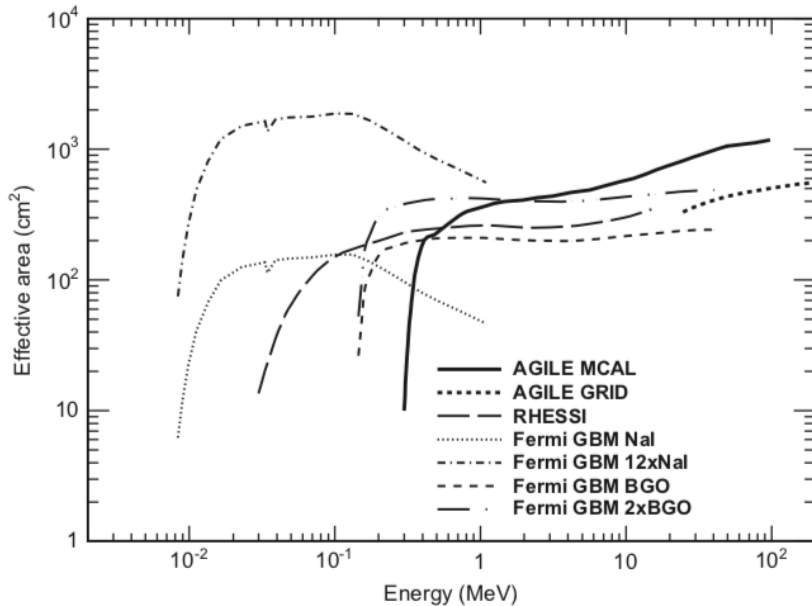


Figure 3.1: Effective area as a function of energy for AGILE, RHESSI and Fermi. Figure from *Marisaldi et al.* [2013].

### 3.1 BATSE

The first TGFs detected were reported by *Fishman et al.* [1994]. They identified 12 "intense Gamma-Ray Flashes" in data between 1991 and 1993, from the Burst and Transient Source Experiment (BATSE). The instrument was onboard the Compton Gamma-Ray Observatory (CGRO) and was launched 5th April in 1991 to an orbit of  $\sim 450$  km altitude, with an inclination of  $28.5^\circ$ . BATSE had 8 sets of scintillators located on every corner of CGRO facing outwards. As the scintillators together covered most of the whole sky, X-rays and gamma-rays were usually detected by at least four detectors. The relative observed intensity between the detectors could be used to triangulate the direction of the incoming photons. The Large Area Detectors (LAD) were made of NaI with a typical energy range of 28 - 1800 keV [*Preece et al.*, 1999]. The effective area was  $2.025 \text{ cm}^2$ , and it was 1.27 cm thick. The Spectroscopy Detector (SD) was also part of each module and was a cylinder of NaI with 12.7 cm in diameter and 7.6 cm thick [*Dwyer et al.*, 2012]. In the literature, the BATSE TGFs is from the LAD data, but SD detected TGFs as well.

BATSE was designed to detect celestial gamma-ray sources. The trigger sampling time onboard BATSE was 64 ms, and as TGFs have a typical duration of hundreds of  $\mu\text{s}$ , only the brightest TGFs were detected. This was pointed out by *Fishman et al.* [1994] saying that "It is likely that many other weaker events of similar origin go undetected because of the trigger criteria implemented by the experiment."

In Figure 3.2, the 12 events reported in *Fishman et al.* [1994] are shown. The events lasted from  $\sim 0.1$  to 2ms. *Fishman et al.* [1994] also suggested that the source of the short gamma-ray bursts detected by BATSE could be bremsstrahlung produced by high energetic electrons. They also pointed out that the TGFs were linked to thunderstorms, providing cloud images associated with two of the TGF events. BATSE detected a total of 78 TGFs during 9 years of operation [*NASA*, Accessed 14.05.2018].

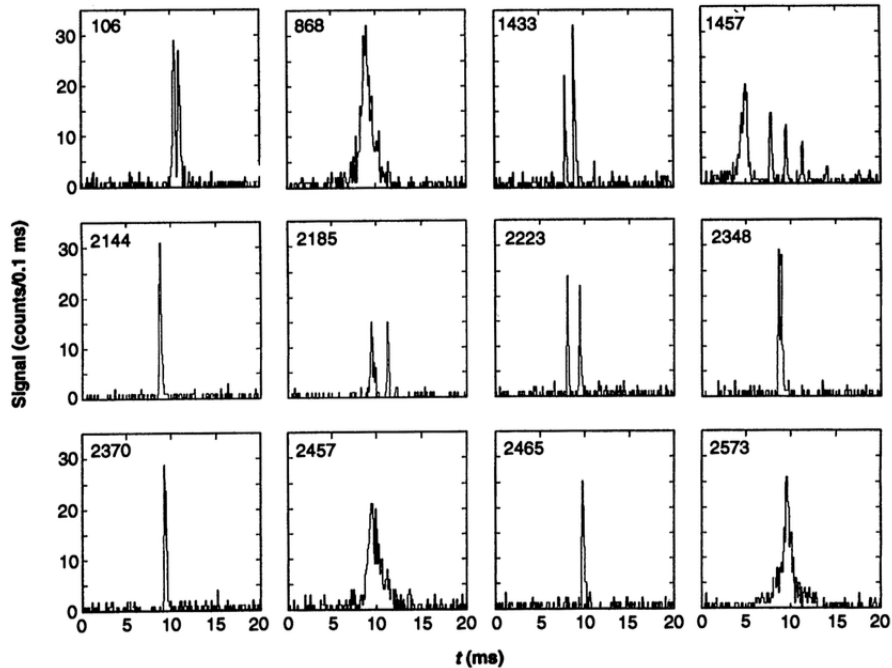


Figure 3.2: 12 TGFs detected by BATSE. Time is arbitrary, and the bin size is 0.1 ms. Typical durations are  $\sim 0.1$  to 2 ms. Figure from *Fishman et al.* [1994].

### 3.2 RHESSI

The Reuven Ramaty High Energy Solar Spectroscopic Imager (RHESSI) was the next mission to report detections of TGFs after BATSE. RHESSI was launched 5th February 2002 to an orbit of  $\sim 600$  km altitude, with an inclination of  $38^\circ$ . RHESSI is still operating at the time of writing. The only instrument onboard is an array of nine hyper-pure germanium detectors with an energy range of 3 keV to 17 MeV. All energies above 17 MeV are measured in an overflow channel [*Smith et al.*, 2002].

RHESSI continuously collects data, while BATSE had a trigger system. This makes it possible to search for weak TGFs in the RHESSI data telemetered to ground. *Dwyer and Smith* [2005] used the observed TGF energy spectrum by RHESSI to confine the source altitude to between 15 and 21 km.

*Grefenstette et al.* [2009] presented the first RHESSI TGF catalog, containing 820 TGFs detected between March 2002 to February 2008. *Gjesteland et al.* [2012] later developed a new TGF search algorithm. For the period 2004 to 2006, they reported that they found more than twice the number of TGFs as reported by *Grefenstette et al.* [2009].

### 3.3 AGILE

The Astrorivelatore Gamma a Immagini Leggero (AGILE) is a satellite by the Italian Space Agency and is providing the data used in this thesis. It was launched 23rd April 2007 in an equatorial orbit with an inclination of  $2.5^\circ$ , and an altitude of  $\sim 535$  km [*Tavani et al.*, 2009]. The main purpose of the satellite is gamma-ray astrophysics. The detector detecting most TGFs is the Mini-Calorimeter (MCAL). Like BATSE, MCAL is triggered. There are several trigger sampling times, and they range from  $293 \mu\text{s}$  to 8 s [*Marisaldi et al.*,

2014]. As TGFs are very brief,  $\sim 100 \mu\text{s}$ , the lower trigger sampling time increases the instrument sensitivity to TGFs. AGILE’s detectors and datasets are discussed thoroughly in Section 4.2 and 4.3.

### 3.4 Fermi

The Fermi Gamma-ray Space Telescope is a satellite launched 11th June 2008 with an inclination of  $25.6^\circ$ , and an altitude of 565 km [Briggs *et al.*, 2010]. Fermi is still operative at the time of writing. There are two instruments onboard designed to detect cosmic gamma-ray sources; The Large Area Telescope (LAT) and the Gamma-ray Burst Monitor (GBM). The GBM consists of 12 NaI scintillators with an energy range of  $\sim 8 \text{ keV}$  to  $\sim 1 \text{ MeV}$ , and two Bismuth Germanate Oxide (BGO) with an energy range of  $\sim 200 \text{ keV}$  to  $\sim 40 \text{ MeV}$  [Briggs *et al.*, 2010].

The GBM is triggered with a sampling time of 16 ms, compared to BATSE’s 64 ms [Meegan *et al.*, 2009]. During the first year of observation, Fermi detected 12 TGFs. The trigger logic was then changed and now data are acquired continuously. The first Fermi GBM TGF catalog consists of 4144 TGFs, between 11th July 2008 and 31st July 2016 [Roberts *et al.*, 2018].

### 3.5 ADELE

The Airborne Detector for Energetic Lightning Emission (ADELE) is a gamma-ray detector suite, designed to be hosted onboard an aircraft, flying over thunderstorms. During a campaign, it flew within 10 km radial distance over a thunderstorm with over 1000 lightning flashes detected by several lightning networks. They detected only one TGF [Smith *et al.*, 2011]. The authors concluded from this that the TGF-lightning ratio is between 0.1 % and 1 %.

Bowers *et al.* [2018], using ADELE data, reported the detection of bremsstrahlung coincident with a nearby lightning detection. They conclude that this is the first experimental evidence of radiation from a backward positron beam created by the forward electron beam from a TGF according to RREA theory.

### 3.6 ASIM

The Atmosphere-Space Interactions Monitor (ASIM) was launched 2. April 2018 and was mounted to the Columbus module on the International Space Station (ISS). This is the first instrument specifically designed to observe TGFs. Onboard there is an X-ray detector, gamma-ray detector, two cameras and two photometers [Skogseide *et al.*, 2012]. The X-ray detector is a Cadmium Zinc Telluride (CZT) semiconductor with an energy range of 15-400 keV. The gamma-ray detector is a BGO scintillator with an energy range of up to 40 MeV. The effective area of the CZT and BGO combined is  $\sim 900 \text{ cm}^2$  [ESA, Accessed 20.05.2018]. These detectors combined provide a tool for observing TGFs and lightning flashes from space. At the time of writing, ASIM is still in the commissioning phase.



### 3.7 Others

In addition to the missions mentioned, *Ursi et al.* [2017] found 12 TGF candidates in the BeppoSAX data archive. BeppoSAX is an Italian/Dutch satellite dedicated to high-energy astrophysics, and was operative between 1996 and 2002. The instrument detecting the TGFs was the Gamma-ray Burst Monitor (GRBM). The GRBM consisted of four CsI(Tl) scintillators, with an energy range of 40 keV to 700 keV. The sampling time to trigger was 7.8 ms – 4 s, which is too long to be sensitive to TGFs.

TGFs are also possible to be detected from ground. *Tran et al.* [2015] and *Hare et al.* [2016] reported the observation of TGFs by several different ground based detectors in Florida.

### 3.8 TGF correlation to ground-detected lightning

Two of the first 12 TGFs observed by *Fishman et al.* [1994], were linked to thunderstorms using satellite images. As it is discussed below, the association with thunderstorm activity is now established, but the exact processes are not completely understood.

*Inan et al.* [1996] measured radio waves, so-called sferics, associated to lightning (see Section 2.3), and provided evidence of thunderstorms close to the assumed origin of the two TGFs reported in *Fishman et al.* [1994]. One of them had a  $\pm 1.5$  ms association between the sferic and the TGF.

When *Smith et al.* [2005] found that RHESSI detected between 10 and 20 TGFs per month, the TGF-lightning correlation study could continue. *Cummer et al.* [2005] confirmed *Inan et al.* [1996] by analyzing 26 TGFs observed by RHESSI. 13 of these TGFs had sferics associated with them within -3 and +1 ms. All the 13 discharges had positive polarity. They reported that these sferics occurred within  $\sim 300$  km from RHESSI's sub-satellite point.

In a more extensive study, *Inan et al.* [2006] found that 76 % of the TGFs detected in the sub-satellite point region of RHESSI had sferics associated with them within few ms.

*Lu et al.* [2010] investigated a TGF detected by RHESSI on 26th July 2008. The radio signals from the TGF were also detected by the North Alabama Lightning Mapping Array (LMA). They showed that the TGF was produced by an intra cloud (IC) lightning flash between the main negative (MN) (8.5 km) and upper positive (UP) (13 km) charge layers, close to the RHESSI sub-satellite point. This was confirmed by *Shao et al.* [2010] using the Los Alamos Sferic Array. The TGF associated sferic had signatures like an +IC flash at an altitude between 10.5 to 14.1 km. An +IC flash develops from the MN charge region and transports electrons up to the UP charge region.

*Collier et al.* [2011] analyzed 972 TGFs detected by RHESSI and found 93 WWLLN matches. Most of the TGFs occurred within 500 km from the sub-satellite point, and a few TGFs occurred at larger distances.

*Cummer et al.* [2011] analyzed the count rates from two TGFs detected by Fermi and the magnetic fields produced by associated lightning flashes. They suggested that sferics generated may be produced by the TGFs themselves. *Østgaard et al.* [2013] suggested the same.

*Briggs et al.* [2013] reported that, after they identified more TGFs in the Fermi data, about one-third of the new TGFs had WWLLN matches. *Connaughton et al.* [2013] found that

the WWLLN TGF detection rate depends strongly on the duration of TGF. 50 % of brief TGFs had WWLLN matches, and longer TGFs had less than 10 % WWLLN matches.

*Mezentsev et al.* [2016] used TGFs detected by RHESSI, WWLLN, and sferics recorded at Duke University. Sometimes there are two TGFs associated with the same sferic. These events are called a double TGF. In all of the 16 double TGFs analyzed, the sferic was associated with the last of the two TGFs. There is no clear explanation for this yet.

*Østgaard et al.* [2015] and *Smith et al.* [2016] searched for weak TGFs in the RHESSI data, using a search algorithm based only on TGF counts associated with WWLLN sferics. Although *Østgaard et al.* [2015] identified 141–191 new weak TGFs in the RHESSI data between 2002 and 2012, *Smith et al.* [2016] conclude that their combined results strongly indicate that TGFs are rare.

*McTague et al.* [2015], using a similar approach as *Østgaard et al.* [2015] and *Smith et al.* [2016], found no weak TGFs in the Fermi GBM data.

The AGILE data is the only mission for which a systematic search of lightning associated counts has not been done yet. This is the intent of this thesis. *Marisaldi et al.* [2013] reported no association with WWLLN in the AGILE data between 2009 and 2012. *Marisaldi et al.* [2015] found that 14 % of the TGFs in the period between 23rd March and 24th July 2015, had WWLLN matches. The increased TGF-lightning ratio is due to an AGILE configuration change discussed in Section 4.2.1.

### 3.9 TGF source altitudes and energy spectrum

The production altitude has been discussed in the literature since TGFs were discovered by *Fishman et al.* [1994]. The TGF production altitude was long assumed to be above 30 km, and that TGFs were connected to phenomenas like sprites [*Inan et al.*, 1996]. *Cummer et al.* [2005], using sferics associated with TGF observations by RHESSI, suggested that the production altitude was below 30 km. *Dwyer and Smith* [2005] and *Carlson et al.* [2007] found, using Monte Carlo simulations, that a source altitude of TGFs between 15 - 21 km is consistent with the observed energy spectrum by satellites. For the top of thunderstorms, an altitude of 15 km is not unusual at low latitudes. (See Section 2.1.) *Lu et al.* [2010] and *Shao et al.* [2010] reported that the MN charge layer and UP charge layer were between 8.9 km and 14 km. *Cummer et al.* [2014] reported a TGF source altitude around 12 km.

In Figure 3.3, the energy spectrum of superposed TGF counts from RHESSI are shown. Note that the maximum energy range of RHESSI is  $\sim 20$  MeV (discussed in Section 3.2). The energy spectrum range from a few 10 keV to  $\sim 40$  MeV [*Dwyer and Smith*, 2005; *Smith et al.*, 2005; *Briggs et al.*, 2010; *Marisaldi et al.*, 2010a]. *Tavani et al.* [2011] reported maximum energies of 100 MeV associated to TGFs. However, this result can partly be explained as pile-up, (i.e. energies from several photons counted as one photon) due to the high fluxes of photons associated with TGFs [*Marisaldi et al.*, 2018].

The typical time duration of TGFs is 100 – 250  $\mu$ s [*Gjesteland et al.*, 2010; *Fishman et al.*, 2011; *Marisaldi et al.*, 2015].

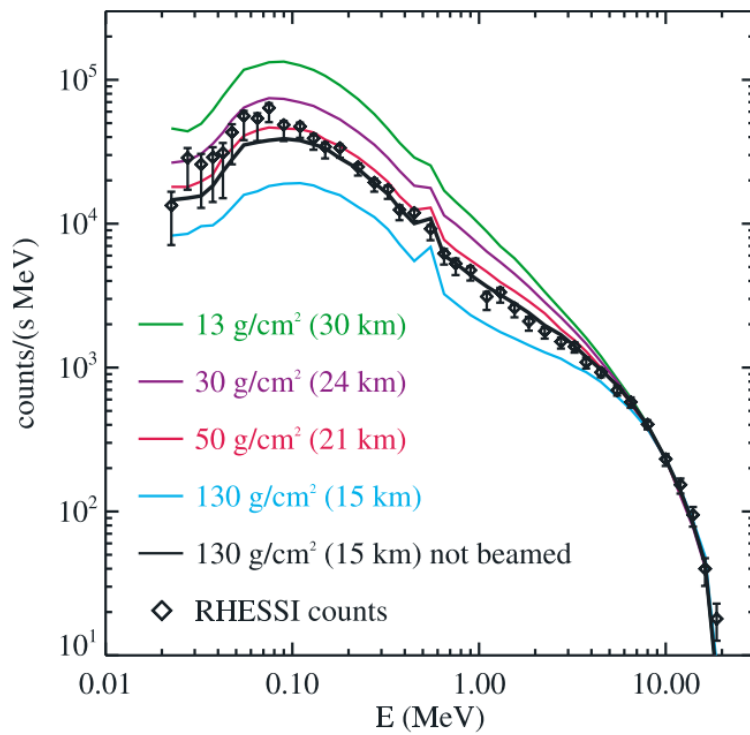


Figure 3.3: Energy spectrum of superposed TGF counts from RHESSI, and Monte Carlo simulated RREA spectrum for different altitudes. Figure from *Dwyer and Smith* [2005].



# Chapter 4

## Instruments and Datasets

This chapter describes the instruments and outlines the different datasets which have been used in this thesis. The WWLLN dataset contains lightning detections, the MCAL and GRID datasets contain measurements from the satellite AGILE, and the last dataset is the satellite position of AGILE.

### 4.1 The World Wide Lightning Location Network

The World Wide Lightning Location Network (WWLLN) is a global lightning detection network based on Time Of Group Arrival (TOGA). (Explained in Section 2.3.) There are 70 stations around the world detecting VLF radio waves from lightning flashes [Hutchins *et al.*, 2013]. The number of stations has grown from 18 stations in 2004, to 70 stations in 2013 [Mallick *et al.*, 2014]. In Table 4.1, the total number of WWLLN detections between 2008 and 2017 is shown.

Abarca *et al.* [2010] reported a detection efficiency for CG flashes "from 3.88 % in 2006–2007 to 10.30 % in 2008–2009", using the National Lightning Detection Network (NLDN) as reference. Rudlosky and Shea [2013] reported that the detection efficiency "steadily improves from 6 % during 2009 to 9.2 % during 2012", using the Tropical Rainfall Measuring Mission Lightning Imaging Sensor (TRMM-LIS) instrument as reference. These WWLLN efficiencies are for the United States.

Hutchins *et al.* [2012] pointed out that WWLLN does not observe lightning with the same detection efficiency everywhere. This can be due to the density of the WWLLN stations, and the strong effect orography and ionospheric conditions have on the EIWG. The WWLLN detection efficiency also depends on the local time as sunlight affects the ionospheric conditions. Bürgesser [2017], with results in agreement with Rudlosky and Shea [2013], estimated a WWLLN detection efficiency with values in the range of 1 % - 10 % for continental regions and 20 % for oceanic regions.

In Figure 4.1 the *relative* detection efficiency and WWLLN stations are shown. It shows that the station density, and therefore the detection efficiency, is better in the United

Table 4.1: Total number of WWLLN detections per year from 2008 to 2017.

Year	2008	2009	2010	2011	2012	2013	2014	2015	2016	2017
Number of WWLLN detections in millions	78	115	139	153	189	210	228	226	212	207

States, the Pacific Ocean and Indonesia, compared to Africa.

All the papers above report that the detection efficiency is dependent on the strength of the lightning flash. The minimum detectable energy is a function of time and position, and the WWLLN station threshold. The station threshold is adjusted according to the background VLF signal. The threshold is varying slowly during the day, and if the station detects many strokes at a given time, the threshold increases.

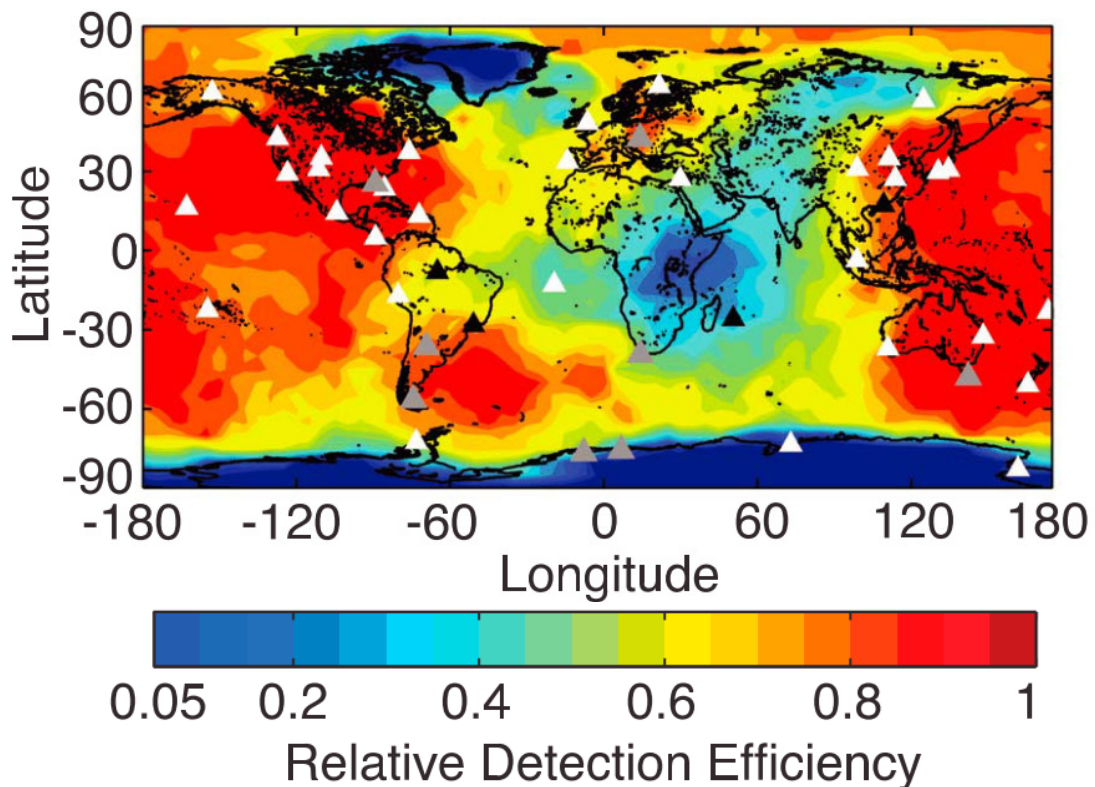


Figure 4.1: Relative detection efficiency for the WWLLN network 16. June 2010. Operational WWLLN stations are shown as white triangles, non-operational in black, and partly active in grey. Figure from *Hutchins et al. [2012]*.

*Abarca et al. [2010]* found that the location of the lightning flash has a bias in the northward and westward direction. In the northward direction, the average error is 4.03 km, and in the westward direction, the error is 4.98 km. *Østgaard et al. [2013]* use a location uncertainty of 15 km. We will use the location uncertainty used by *Østgaard et al. [2013]* in this thesis.

The WWLLN dataset consist of trigger times, each representing a detection of a sferic, for each day. The data used in this analysis has an ASCII file with time, latitude and longitude of each sferic detected for each day. The data is not entirely sorted in time. WWLLN data are provided to Birkeland Centre for Space Science through a subscription service.

## 4.2 The AGILE mission and Detectors

The Astro-rivelatore Gamma a Immagini LEggero (AGILE) is a satellite owned and operated by the Italian Space Agency. It is designed to observe distant gamma-ray sources. It was launched on 23rd April 2007 in an equatorial orbit with an inclination angle of  $2.47^\circ$ , and an average altitude of 535 km [Tavani *et al.*, 2009]. AGILE's energy range and excellent timing resolution also makes it one of few satellites capable of detecting TGFs.

There are three instruments onboard AGILE. The Gamma-Ray Imaging Detector (GRID), the hard X-ray Imager (Super-AGILE) and the Mini-Calorimeter (MCAL). A plastic anti-coincidence (AC) shield surrounds the payload. In this analysis, the MCAL and GRID instruments have been the sources of data. The hard X-ray Imager has not been used. In Figure 4.2a a schematic of the payload is shown.

The data acquisition onboard AGILE is inhibited during passage through the South Atlantic Anomaly. This is done due to limited available telemetry.

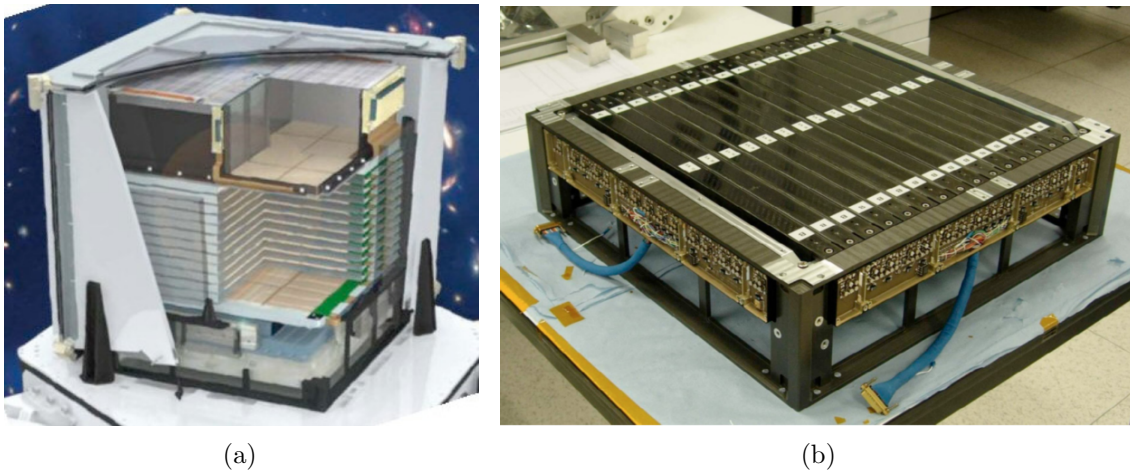


Figure 4.2: a) Schematic view of the scientific instruments onboard AGILE. The picture shows, from top to bottom, the hard X-ray Imager, GRID, and MCAL. There are no electronics shown, and the AC-system is partially displayed. The cube weighs about 100 kg, and each side is about 60 cm long. b) The MCAL detector, showing the top plane of the two orthogonal planes of CsI(Tl) scintillator bars. Both pictures are taken from Tavani *et al.* [2009].

### 4.2.1 The Anti-Coincidence system

The anti-coincidence (AC) system surrounds all the detectors onboard AGILE, and its aim is to efficiently reject charged particle background. Although the AC-system is designed to reject charged particles, it has a non-negligible sensitivity to hard X-rays. The default AC time window is  $4.5 \mu\text{s}$ , but as the AC-system is paralyzable, the AC time window can extend up to larger values in the case of high fluxes. To enhance the detection of TGFs, the AC-system was disabled for MCAL on 23rd March 2015 [Marisaldi *et al.*, 2015]. This was done since the AC-system prevented events with duration shorter than  $\sim 100 \mu\text{s}$  to be detected, due to deadtime induced by the AC-system.

## 4.2.2 The Mini-Calorimeter

The Mini-Calorimeter (MCAL) is a gamma-ray detector originally designed to detect cosmic gamma-ray bursts (GRB). It consists of 30 CsI(Tl) scintillator bars placed in two orthogonal layers (see Figure 4.2b). Each bar has a size of  $15 \times 23 \times 375 \text{ mm}^3$ . At the two ends of each scintillator, a PIN photodiode is reading the scintillation light. The intensity of the scintillation light is a function of the position of interaction along the bar, and the energy of the incoming particle. MCAL has an energy range from 300 keV to 100 MeV, and a thickness of 1.5 radiation lengths [Labanti *et al.*, 2009]. One radiation length is the mean distance which a high energy electron travels before losing  $1/e$  of its energy by bremsstrahlung, and  $7/9$  of the mean free path for pair production by a high energy photon [Segre, 1965]. The absolute time accuracy is  $\sim 2 \mu\text{s}$  [Labanti *et al.*, 2009].

MCAL can be operated in two different data acquisition modes, and both modes can be active at the same time. The two different modes are called "GRID mode" and "BURST mode" [Labanti *et al.*, 2009].

In GRID mode, MCAL is part of the GRID detector. Another part of the GRID, the Silicon Tracker (ST), issues a trigger to MCAL, and signals from all the 30 scintillator bars are collected. The deadtime for the GRID is  $\sim 100 - 200 \mu\text{s}$  due to the data readout of the ST.

The mode used in this analysis is the BURST mode. In BURST mode each bar acts an independent detector with an average deadtime of  $20 \mu\text{s}$ . The deadtime is the time after a detection of a particle or photon, that the detector takes to recover before it can detect another count. It includes the time needed for data readout. In a short burst of photons, depending on the flux, if some bars are down because of deadtime, the other bars are capable of detecting new photons. BURST mode is triggered, meaning the data is not a continuous data flow.

The trigger logic acts on time windows from  $293 \mu\text{s}$  to  $8 \text{ s}$  [Marisaldi *et al.*, 2014]. For TGF search, the relevant time windows are  $293 \mu\text{s}$ ,  $1 \text{ ms}$ , and  $16 \text{ ms}$ . The static thresholds, i.e. the minimum of counts needed to issue a trigger, are 8, 10 and 41 counts, respectively [Marisaldi *et al.*, 2014, 2015]. After a trigger, data  $\pm 1 \text{ sec}$ , with respect to the trigger time, is sent to telemetry.

The only parameters used in this analysis, are the time of arrival and the calculated energy of the photons.

### MCAL Gamma-ray Detection

This section is based on Appendix A in Labanti *et al.* [2009].

When gamma particles interact with a scintillated crystal, they produce secondary electrons through photoelectric effect, Compton scattering and pair production. These secondary electrons lose all their kinetic energy, almost at the same time, through collisions with the molecules in the scintillation crystal. The (scintillation) light is generated from the de-excitation of the electrons and is proportional to the incoming energy of the gamma particle. The intensity of the scintillated light is given by

$$I(x) = I_0 e^{-\alpha x} + I_{\text{offset}} \quad (4.1)$$

where  $I(x)$ ,  $I_0$ ,  $\alpha$ ,  $I_{\text{offset}}$  is the intensity after some distance  $x$ , the intensity at  $x = 0$ ,



the attenuation coefficient and the equivalent intensity from e.g. electronics offset signal, respectively.

The scintillation light is detected by a photodiode. A photodiode is a pn-junction operated in reverse bias. When a photon hits the depletion region, it generates a charge pulse by the photoelectric effect. The total charge in the pulse is therefore proportional to the energy of the incoming photon.

Let us consider a scintillation bar of length  $L$  and a photodiode at each end of the bar at position  $-L/2$  and  $L/2$ . The reference frame is centered at the middle of the bar. The photodiodes are called PD-1 and PD-2. They have an offset  $O_1$  and  $O_2$ , and a gain  $u_{0,1}$  and  $u_{0,2}$ , from the electronic chains. If a particle with energy  $E$  is hitting the bar at position  $x$ , the output from the two photodiodes, in an energy unit, is given by

$$U_1(x, E) = O_1 + u_{0,1}Ee^{-\alpha_1(x+L/2)} \quad (4.2)$$

$$U_2(x, E) = O_2 + u_{0,2}Ee^{-\alpha_2(L/2-x)} \quad (4.3)$$

where  $\alpha_1$  and  $\alpha_2$  are the attenuation coefficients of side 1 and 2.

If we assume that  $\alpha_1 = \alpha_2 = \alpha$  we get

$$x = \frac{1}{2\alpha} \left( \ln \left( \frac{U_2 - O_2}{U_1 - O_1} \right) + \ln \left( \frac{u_{0,1}}{u_{0,2}} \right) \right) \quad (4.4)$$

$$E = \frac{e^{\alpha L/2}}{\sqrt{u_{0,1}u_{0,2}}} \sqrt{(U_1 - O_1)(U_2 - O_2)} \quad (4.5)$$

The parameters  $O_1$ ,  $O_2$ ,  $u_{0,1}$ ,  $u_{0,2}$ ,  $\alpha_1$ ,  $\alpha_2$  have been measured during ground calibration campaigns.  $E$  is the reconstructed photon energy used in this thesis.

### 4.2.3 The Gamma-Ray Imaging Detector

The Gamma-ray Imaging Detector (GRID) consists of a Silicon-Tungsten tracker (ST), MCAL and the AC-system. The GRID has an energy range from 30 MeV to 50 GeV. The deadtime is  $\sim 100 - 200 \mu\text{s}$  and the absolute time resolution is  $\sim 2 \mu\text{s}$  [Tavani *et al.*, 2009]. The deadtime is induced by the data readout. The AC-system is always active on the GRID. The ST detection principle is based on photon conversion into positron-electron pairs. The positrons and electrons leave tracks in position sensitive layers made of silicon micro strip detectors. From these detections it is possible to 3D reconstruct the particle paths and calculate the direction of the incoming photon. The GRID is not triggered like MCAL, but has a continuous data acquisition.

## 4.3 The AGILE datasets

A summary of the AGILE datasets, used in this thesis, is shown in Table 4.2. The characteristics of the datasets, regarding the TGF analysis, depends on the absolute timing accuracy, and if the AC-system is disabled or not. There are two critical dates: 23.03.2015 when the AC was disabled for MCAL, and July 2015 when an issue with the onboard GPS caused a degradation of the AGILE timing performance, resulting in a lower absolute onboard timing accuracy.

In the period before 23.03.2015, the AC-system was enabled for MCAL, and the absolute timing accuracy was on microsecond level. In case of large gamma-ray fluxes, the AC-system induces up to 100 – 200  $\mu$ s deadtime for MCAL, making it inefficient at TGF detection. The best period searching for TGFs in the MCAL data, is between the AC-system was disabled, until the GPS failure. After the GPS failure, the absolute timing of the clock onboard AGILE started to have an offset in absolute time which changed with time.

The AGILE data are available from the AGILE Science Data Center (ASDC). For MCAL, each contact is saved as a file including different quantities. (The contact number is the number of orbits the satellite has done and it identifies univocally the datafiles where AGILE observations are stored.) The quantities used in the MCAL data are the onboard time, total energy of photon and Contact. The GRID data is available in the Flexible Image Transport System (FITS) data format. The quantities used for the GRID are onboard time and Contact.

### 4.3.1 GRID period

The GRID data used in this analysis are from 01.06.2008 - 23.06.2015. This is before the GPS failure, and therefore the absolute timing is always on  $\mu$ s level. The AC-system is always active on the GRID.

### 4.3.2 AC-ON period

In the period after the launch of AGILE, until July 2015, the absolute onboard timing accuracy is on  $\mu$ s level, and the AC-system is active on both the GRID and MCAL. This period is called "AC-ON" from now on. As mentioned in Section 4.2.1, the AC-system prevents brief duration events, such as TGFs, to be detected by MCAL. During this period the average TGF detection rate according to *Marisaldi et al.* [2014] is  $\sim 0.3$  TGFs/day. The exact period analyzed is 17.01.2008 00:00:00 - 22.03.2015 23:59:59.

### 4.3.3 REF period

The reference (REF) period, 23rd March - 24th June 2015, is considered the best dataset to search for TGFs, as the absolute timing accuracy is accurate at  $\mu$ s level, and the AC-system is disabled. *Marisaldi et al.* [2015] reports a total of 279 TGFs in this period, which is a detection rate increase from 0.3 TGFs/day to 3 TGFs/day compared to when the AC-system was active. The detection algorithm used in *Marisaldi et al.* [2015] is independent of WWLLN matches and described in *Marisaldi et al.* [2014]. The exact period analyzed is 23.03.2015 00:00:00 - 23.06.2015 23:59:59.

### 4.3.4 DRIFT period

In July 2015, an issue with the onboard GPS caused a degradation of the AGILE  $\mu$ s timing performance. The onboard timing accuracy is essentially dependent on the number of satellite the GPS is able to lock in. This period is called the "DRIFT period" from now on, because the onboard time started "drifting". The drift is a systematic offset in time that remains constant for periods between days and weeks, and then suddenly "jumps" to a different value. This is illustrated in Figure 4.3, where  $\Delta t$  is the timing offset.

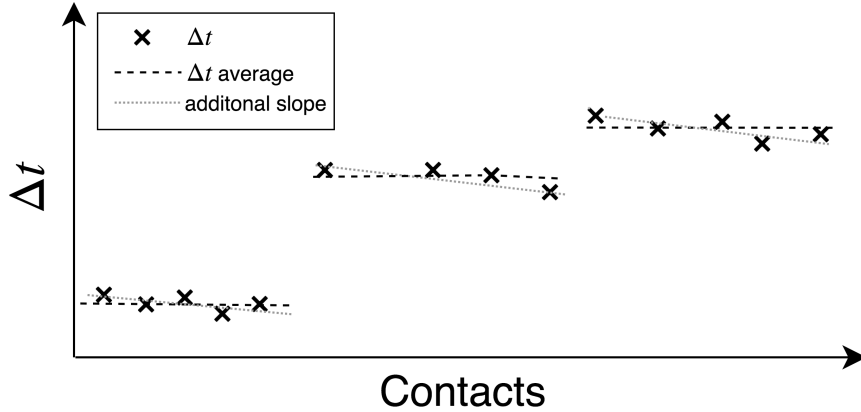


Figure 4.3: Illustration of the time drift. The Xs are the timing offset between computer commands. The average of these is indicated with a dotted black line. The additional grey slope is the additional drift discovered in this analysis, discussed in Section 6.5.

It is possible to make a crude timing correction of the offset, using housekeeping data. The spacecraft’s main computer is an independent system from the payload computer, and therefore has its own clock. This clock is synchronized to UTC during each ground station contact (once every orbit). In the spacecraft computer there are loaded time-tagged telecommands which will be executed at a specific time during the next orbit. After execution, the payload computer returns a report including execution time in its corrupted time reference frame. Let us say that the spacecraft computer tells the payload computer, to execute a command at 12:03:50 UTC. The moment after, the spacecraft computer receives a report from the payload computer that it executed the command at 12:06:55 UTC. This tells us that the payload onboard time has a 3 minute and 5 second offset ( $\Delta t$  in Figure 4.3). This time difference is accurate down to  $\sim 100$  ms. As there are several of these commands in each so-called Contact, (which is the orbit number counting from the first orbit AGILE did,) the average of these timing differences is the best estimate of the offset for that particular Contact. This is accurate down to a few ms, leaving a statistical error of 1-5 ms. The DRIFT dataset analyzed in this thesis has been corrected for this timing offset.

As the time accuracy is low, the detection of TGFs associated to lightning could not be done based only on time correlation at  $\mu$ s level. A new method was developed based on increased flux, or "clusters", associated with TGFs. A threshold is selected to reject likely background fluctuations to enhance the signal to noise ratio. This is described further in Section 5.4. The exact period analyzed is 01.01.2016 00:00:00 - 09.11.2017 10:09:10.

#### 4.3.5 3D-FIX period

After the DRIFT period, the GPS partly recovered, meaning that the GPS calculates the 3D satellite position correctly (3D-FIX), and the timing accuracy should be normal (i.e.  $\sim \mu$ s). But for still unknown reasons, the onboard time data, received in telemetry, is still affected by an offset. The onboard time is number of second and microsecond since 01.01.2004. The "seconds" is called the integer part and the "microseconds" is the fractional part. The integer part is affected by an offset (like the DRIFT period) however, as the fractional onboard time, which is reset every second by the GPS signal, is in a different computer register, it is expected that the fractional time is back to the  $\sim \mu$ s accuracy, as in the REF period. The offset with respect to UTC therefore should always

be only an integer number of seconds. The correctness of this statement can only be checked by an external source, such as TGFs association to sferics. The exact period analyzed is 17.01.2018 23:34:57 - 14.04.2018 23:15:26.

Table 4.2: Main characteristics of the different datasets used in this work.

Instrum.	Name	Date	AC	Timing accuracy
GRID	GRID	01.06.2008 – 23.06.2015	on	2 $\mu$ s
MCAL	AC-ON	17.01.2008 – 22.03.2015	on	2 $\mu$ s
MCAL	REF	23.03.2015 – 23.06.2015	off	2 $\mu$ s
MCAL	DRIFT	01.01.2016 – 09.11.2017	off	$\sim$ 1-5 ms
MCAL	3D-FIX	17.01.2018 – 14.04.2018	off	2 $\mu$ s (to be verified)

## 4.4 Satellite position

The position of AGILE is computed using "build\_AGILE\_position\_files\_2.py" available in the git repository [https://github.com/andersbhm/Software\\_master\\_thesis](https://github.com/andersbhm/Software_master_thesis). The software computes AGILE's position for every second and saves it to a file. It uses Two-line element set (TLE), and information about the Earth rotational axis. TLE is a data format used for giving information of an object orbiting the Earth. It is produced by NORAD and based on radar observations. The TLE data is retrieved from [www.space-track.org](http://www.space-track.org). Information about the Earth rotational axis is retrieved from [www.iers.org](http://www.iers.org).

Before the GPS failure, the GPS provided accurate position information included in the AGILE data files. After the failure, the position had to be calculated using TLE. For consistency, it was chosen to use only TLE for the different datasets in this thesis.

Figure 4.4 and 4.5 show AGILE's latitude and altitude as a function of time. The altitude is decreasing due to the atmospheric drag experienced by low orbit satellites. The span in altitude reflects the normal variation between apogee and perigee for a non-perfectly circular orbit.

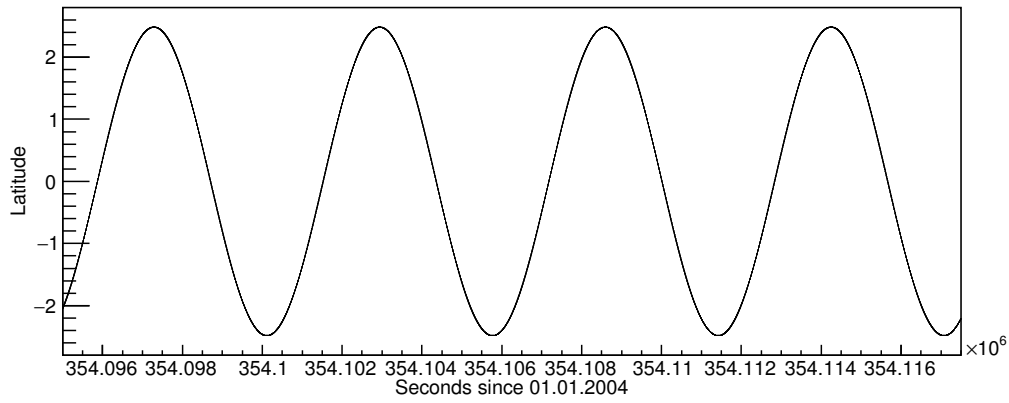


Figure 4.4: AGILE's latitude, as a function of time, for a few orbits.

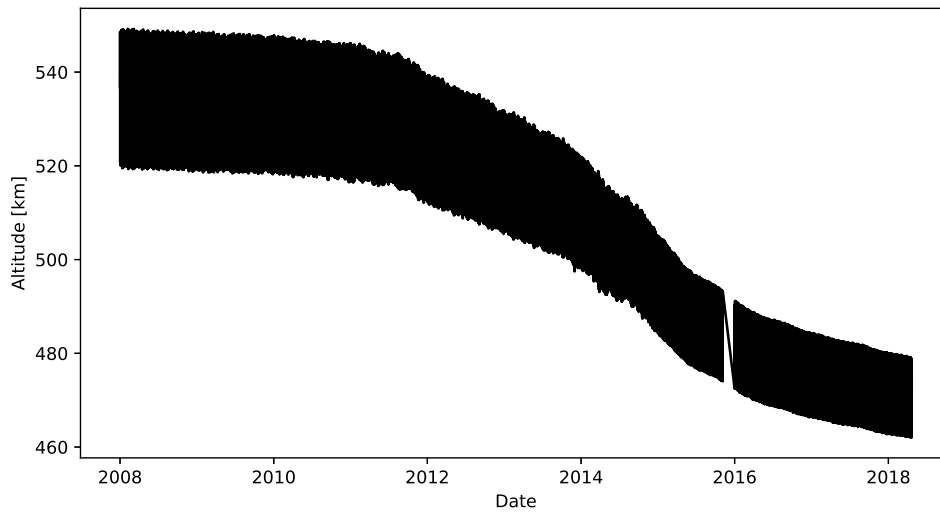


Figure 4.5: The altitude of AGILE as a function of time. There is a data gap at the end of 2015 as we did not calculate the position for these dates.



# Chapter 5

## Method

This chapter describes the method and algorithms used in this analysis. The method consists of 3 steps: 1) dataset reduction, 2) stacking analysis, and 3) search for clusters. Step 1 and 2 are applied to all datasets, while step 3 is not applied to the GRID as the GRID does not have clusters associated with TGFs. This is because of its energy range (30 MeV to 50 GeV) and deadtime ( $\sim 200 \mu\text{s}$ ) preventing it detecting TGFs as closely separated burst of counts.

All software written for this chapter is found in the git repository [https://github.com/andersbhm/Software\\_master\\_thesis](https://github.com/andersbhm/Software_master_thesis). The software is written in Python or C++ using the ROOT analysis framework available from <https://root.cern.ch>.

### 5.1 Reduction of dataset size

The first part of the data analysis consists of reducing the complete dataset to a smaller dataset for more efficient analysis. The motivation is only to keep MCAL data when there is WWLLN data, and only keep WWLLN data when there is MCAL data. The MCAL data is triggered, which means that data is sparse and can effectively be used to reduce WWLLN and position data. The reduction of the datasets is described below in step 1 to 5.

1. Reduce AGILE position file to keep position data in a time window  $\pm 6\text{s}$  around each MCAL measurement.
2. Use the reduced AGILE position file to reduce WWLLN lightning data in a time window  $\pm 20\text{s}$  around AGILE position file and a maximum distance of 1000 km within the sub-satellite point.
3. Remove WWLLN detections which are closer in time than one time bin ( $100 \mu\text{s}$ ), corrected for propagation time. This is done to avoid counting the same lightning twice as a TGF candidate.
4. For every WWLLN detection left, keep only MCAL measurements in a time window  $\pm 3\text{s}$  and  $\pm 100\text{ms}$  around each lightning and save to two different files, called "histo tree" and "photon WWLLN match" in the software. Background data were selected in a time window +3.2 to +3.7 seconds with respect to each lightning, and saved in a separate file.

5. As the two similar WWLLN detections are removed according to step 3 (100  $\mu$ s), but the "photon WWLLN match" file keeps MCAL counts  $\pm 100$  ms around each WWLLN detection, there are sometimes counts associated to more than one WWLLN detection. These count duplicates in the "photon WWLLN match" and the "background" file are removed so that each unique count is associated to the closest in time WWLLN detection.

The software for step 1-5 is found in the git repository in the folder "reducing\_data".

The time windows selected in step 1 and 2 are exaggerated to be on the safe side and could have been smaller. Every new file after each step is sorted by increasing time. This is to make it easier to write the software.

In step 2, a maximum distance between the WWLLN detection and the sub-satellite point is selected to be 1000 km (see Figure 5.1b). The field of view of MCAL, looking down on Earth, has a radius of  $\sim 2400$  km. (This is for an altitude of 500 km and the radius of the Earth at the equator.) The selected 1000 km radius is based on *Connaughton et al.* [2010]; *Cohen et al.* [2010]; *Cummer et al.* [2005] which found most WWLLN matches within 300 km from the sub-satellite point. Only *Cohen et al.* [2010] found some matches up to 1000 km. The 1000 km radius is from now on referred to as the "TGF FOV" (TGF field of view).

In step 3, it is taken into account that WWLLN sometimes detects the same lightning flash several times. Two WWLLN detections, close enough in time and location to be associated with the same counts detected by AGILE, would result in a detection of two TGFs instead of one. Therefore, if two lightning flashes are closer in time and location than one time bin (100  $\mu$ s) in the stacking analysis, only one is kept for further analysis. This is done by taking the difference of ( $time_{lightning} + time_{propagation\ time}$ ) for lightning 1 and lightning 2, and keeping only one of them if the difference is less than 100  $\mu$ s.

In step 1 the AGILE position file is reduced to less than 8 percent of original size. In step 2 the WWLLN data is reduced to less than 1 percent of its original size. The result after step 5 is three different files shown in Table 5.1.



Table 5.1: Reduced datasets originating from full AGILE and WWLLN datasets.

File	Time window centred around WWLLN detection	Parameters
Background	+3.2 to +3.7 s	Onboard time, photon propagation time, time of WWLLN lightning
photon WWLLN match	$\pm 100$ ms	Onboard time, photon propagation time, time of WWLLN lightning, longitude and latitude of sub- satellite point and WWLLN lightning, satellite altitude, contact, distance between lightning and sub-satellite point, total energy of photon
histo tree	$\pm 3$ s	Onboard time, photon propagation time, time of WWLLN lightning, longitude and latitude of WWLLN lightning, total energy of photon

## 5.2 Propagation time of photons associated to TGF

Finding the propagation time between the lightning and the satellite can be done using the haversine formula, solved for distance, and the law of cosine. The haversine formula gives the distance between two points on a sphere using latitude and longitude. Historically it has been used by sailors to calculate distances. Since AGILE has an equatorial orbit, a sphere is used as a model for the Earth, instead of an ellipsoid.

The haversine formula is given in Equation 5.1.

$$S = 2R \arcsin \left( \sqrt{\sin^2 \left( \frac{\psi_2 - \psi_1}{2} \right) + \cos(\psi_1) \cos(\psi_2) \sin^2 \left( \frac{\lambda_2 - \lambda_1}{2} \right)} \right) \quad (5.1)$$

where  $\psi_1, \psi_2, \lambda_1, \lambda_2$  are latitude and longitude, in radians, of point 1 and 2. The distance  $S$  is the great circle arc length between two points.

The law of cosines gives

$$d^2 = (R + h_{sat})^2 + (R + h_L)^2 - 2(R + h_{sat})(R + h_L) \cos(\theta) \quad (5.2)$$

where  $R$  is the radius of the Earth and  $h_{sat}, h_L$  are the altitude of the satellite and the lightning. The distance between the lightning and the satellite is  $d$ .  $\theta$  is the angle between the two points, with origin in the center of the Earth. See Figure 5.1a for a visual view of all the variables.

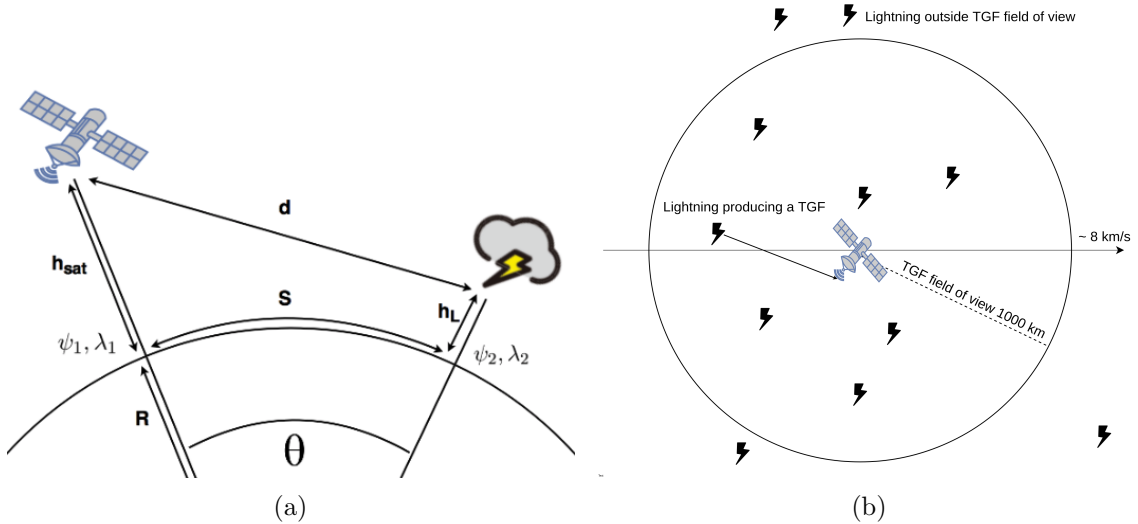


Figure 5.1: a) Illustration of all variables needed to calculate propagation time of photons, using latitude,  $\psi$ , and longitude,  $\lambda$ . b) Illustration of a satellite moving over the Earth's surface. The TGF FOV indicates the maximum radius from the sub-satellite point the WWLLN detection can be, to be included in the data analysis.

Using  $S = R\theta$  gives us  $\theta$ , which is used in Equation 5.2 to solve for  $d$ . Then the propagation time is given by

$$t_{propagation} = d/c \quad (5.3)$$

where  $c$  is the speed of light.

### 5.2.1 Propagation time accuracy

The distance photons travel from the TGF to AGILE,  $d$ , is given in Equation 5.2. The uncertainty of  $d$  is then

$$\Delta d = \sqrt{\left(\left(\frac{\partial d}{\partial h_{sat}} \Delta h_{sat}\right)^2 + \left(\frac{\partial d}{\partial h_L} \Delta h_L\right)^2 + \left(\frac{\partial d}{\partial S} (\Delta S_{sat} + \Delta S_L)\right)^2\right)} \quad (5.4)$$

where  $h_{sat}$  is the altitude of AGILE,  $h_L$  is production altitude of TGFs, and  $S$  is the distance between the sub-satellite point and the WWLLN detection.  $\Delta h_{sat}$  is the uncertainty of the satellite altitude,  $\Delta h_L$  is the uncertainty of the production altitude of the TGFs,  $\Delta S_{sat}$  is the uncertainty of the sub-satellite point, and  $\Delta S_L$  is the uncertainty of the location of the WWLLN detection.

By comparing the calculated TLE satellite position of AGILE with the onboard GPS position in the reference period, an average error of 2 km is found.  $\Delta S_{sat}$  and  $\Delta h_{sat}$  is then

$$2 \text{ km} = \sqrt{\Delta x^2 + \Delta y^2 + \Delta z^2} = \sqrt{3\Delta x^2} \Rightarrow \Delta x = \frac{2 \text{ km}}{\sqrt{3}} = \Delta h_{sat} = \Delta S_{sat} \quad (5.5)$$

assuming independent position error.

The location uncertainty of WWLLN detections is estimated to be 15 km (see Section 4.1).  $\Delta S_L$  is then given by

$$15 \text{ km} = \sqrt{\Delta x^2 + \Delta y^2} = \sqrt{2\Delta x^2} \Rightarrow \Delta x = \frac{15 \text{ km}}{\sqrt{2}} = \Delta S_L \quad (5.6)$$

assuming independent location uncertainty on a surface.

From Section 3.9, the production altitude uncertainty of TGFs is assumed to be

$$\Delta h_L \approx 3 \text{ km} \quad (5.7)$$

For typical numbers,  $h_{sat} = 500 \text{ km}$  and  $h_L = 15 \text{ km}$ , the propagation time uncertainty is shown in Figure 5.2. As most of the TGFs are within 500 km from the sub-satellite point (see Figure 6.13 or *Connaughton et al.* [2010]; *Cohen et al.* [2010]; *Cummer et al.* [2005]), the propagation time uncertainty is

$$\Delta t_{propagation} = \Delta d/c \approx 30 \text{ } \mu\text{s} \quad (5.8)$$

or less.

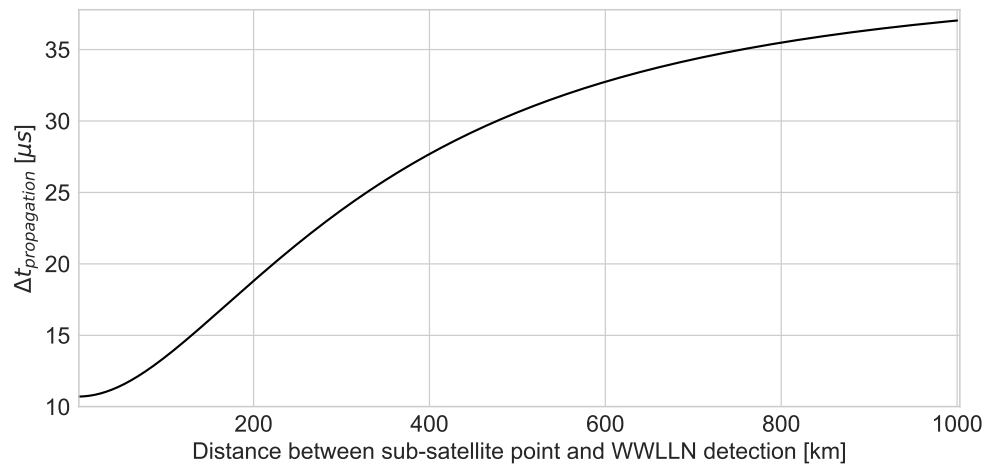


Figure 5.2: The uncertainty in propagation time,  $\Delta t_{propagation} = \Delta d/c$  as a function of the distance  $S$ .

### 5.3 Stacking analysis

Stacking analysis is done in order to find counts that are associated to TGFs too weak to be detected as stand-alone events. This is because these weak TGFs are not significant over the background fluctuations. Figure 5.3 shows a simple illustration of the idea of stacking analysis. Each light curve, associated to lightning, is stacked on top of each other in a stackplot. A light curve is a histogram with counts in the y-axis and time on the x-axis. The time difference between counts detected by AGILE and the WWLLN detection, corrected for propagation time, is referred to as " $\delta t$ " in the rest of this thesis. If  $\delta t = 0$  in Equation 5.9, there is a perfect correlation between the lightning flash and the incoming photon detected by the satellite. If lightning flashes are directly correlated to gamma-ray production, the stackplot should show a statistically significant excess of counts close to  $\delta t = 0$ .

$$\delta t = time_{satellite} - time_{propagation} - time_{lightning} \quad (5.9)$$

The stacking analysis algorithm is described below.

1. For every unique WWLLN detection, create a histogram/light curve with counts according to Equation 5.9.
2. Sum every light curve to a stackplot.

As TGFs have a typical duration of hundreds of microsecond, the lower and higher boundary of the histogram in step 1, is  $\pm 100$  ms.

The uncertainty in  $\delta t$  is a combination of uncertainty in the absolute time of AGILE, WWLLN and the propagation time of the photons. The absolute time uncertainty of AGILE is neglectable as it is  $\sim 2 \mu\text{s}$  [Labanti *et al.*, 2009]. (This is not the case for the DRIFT dataset as the absolute time accuracy of AGILE is on millisecond level.) We also neglect the difference between the speed of light in vacuum and through the atmosphere above 15 km toward space. The bin size is selected to be  $100 \mu\text{s}$ , larger than the uncertainty of  $\delta t$  which is  $\sim 30 \mu\text{s}$ , as discussed in Section 5.2.1.

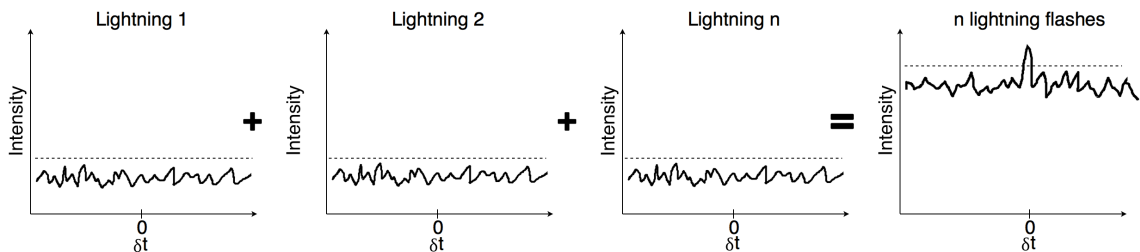


Figure 5.3: Simple illustration of the stacking analysis. The dotted line represents  $3\sigma$  significance level.

## 5.4 Search for clusters

As mentioned in Section 4.3.4, after 1st July 2015 an issue with the onboard GPS caused a degradation of the AGILE  $\mu\text{s}$  timing performance. Stacking analysis relies on timing accuracy at microsecond level to be effective. Otherwise, any potential significant number of counts is spread over a large time interval resulting in a signal not significant above the background fluctuations. A new algorithm was then developed assuming that a TGF should be seen as an increased flux of counts, or a "cluster of photons" in a light curve. The idea is to look at lightcurves and only keep histogram bars with large counts per 100  $\mu\text{s}$ . This is possible as the relative timing accuracy is still at  $\mu\text{s}$  level, and that the absolute timing offset is systematic. The offset is on few millisecond level when corrected by the AGILE team using housekeeping data. The absolute timing offset is constant between days and weeks, and then jump to a new offset.

The cluster algorithm is described below and also as an illustration in Figure 5.4.

1. Build a light curve for each WWLLN detection in the photon WWLLN match file. Do this for the background file too. (Figure 5.4a)
2. Build the distribution of number of counts per 100  $\mu\text{s}$  bin for each light curve. Do this for the background file too. (Figure 5.4b)
3. Stack the distributions of counts per 100  $\mu\text{s}$  bin for both background and WWLLN. (Figure 5.4c)
4. Set a threshold based on signal vs. background. (Figure 5.4c)
5. Build a new histogram using only stacked events with counts per 100  $\mu\text{s}$  bin higher than the selected threshold. (Figure 5.4d)

What is regarded as the signal associated to the WWLLN detection, in Figure 5.4c, is determined by the lower and higher boundary of the light curve histogram plotted in step 1 (Figure 5.4a). This limit is dependent on the duration of the TGF and the absolute timing uncertainty of AGILE. When different light curves with different time drifts are stacked, the final distributions is a combination of several normal distributions with different peaks. The lower and higher boundary of the light curve histogram (Figure 5.4a) is therefore chosen to be 0.5 ms or 100 ms, depending on the onboard timing accuracy in the dataset.

In step 3, the events with highest counts per 100  $\mu\text{s}$  bin are probably associated to a TGF, as TGFs are events with high intensity.

In step 4, the threshold is selected based on the highest signal to noise ratio. The ratio is between the integrals of the TGF signal and the background signal, integrated from the threshold to 20 counts per 100  $\mu\text{s}$ .

In step 5, these events are stackplotted, to see the correlation with WWLLN.  $\delta t$ , in step 5 and Figure 5.4d, is approximated by the middle of the bin with the highest number of counts in Figure 5.4a. This means that  $\delta t$  is a rather crude estimation ( $\sim 100 \mu\text{s}$  accuracy) compared to e.g. a Gaussian fit to the light curve.

When the TGF candidates are identified, they are plotted as a light curve and energy vs. time scatterplot, using the time and position of the lightning flash and the satellite, and the measurements from the original MCAL data. The software is found in the git repository and named "plotting TGF candidates". The light curve for each TGF candidate, for the different datasets, is found in the folder "Lightcurves".

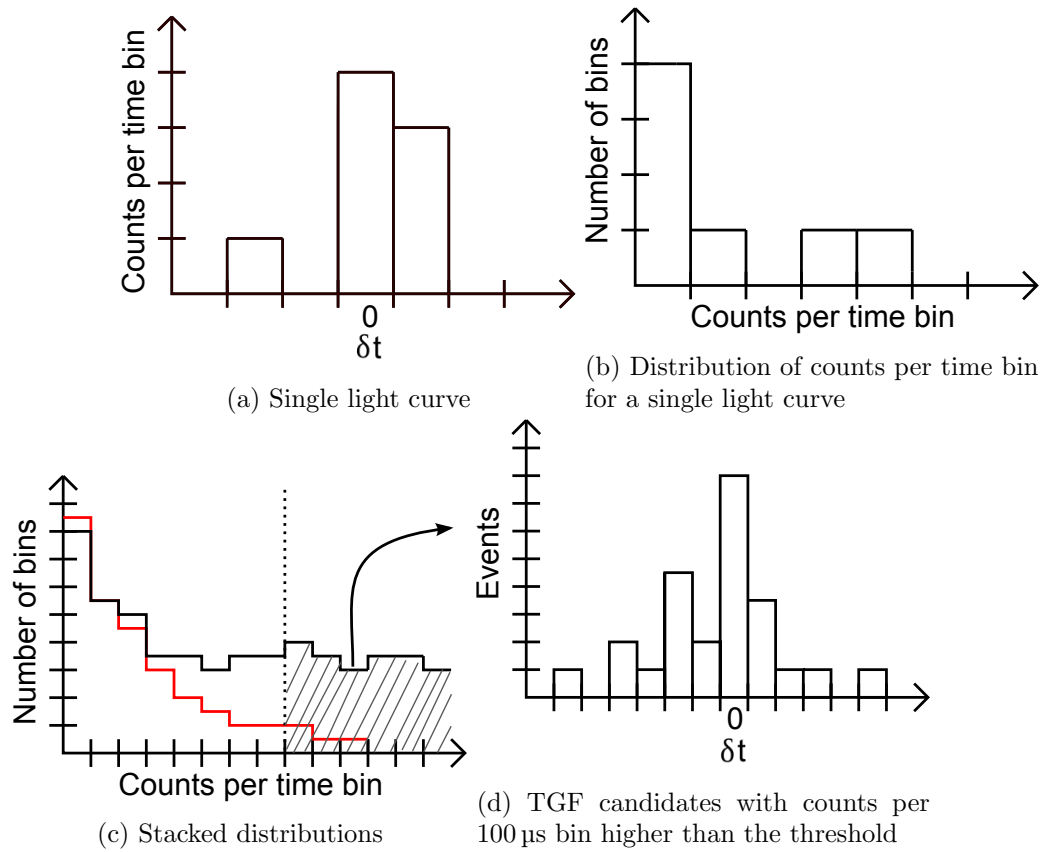


Figure 5.4: a) A single light curve. b) Distribution of counts for the single light curve. c) Superposed distributions of counts per bin associated to a lightning flash in black, and superposed distributions of background in red. A threshold is indicated by a dotted line. d) Distribution of events with counts per time bin over the chosen threshold.

## 5.5 Expected number of WWLLN detections in the TGF field of view, and distance from sub-satellite point

### 5.5.1 Expected number of WWLLN detections in the TGF field of view

The following calculations are motivated by being able to provide a consistency check, so that the total number of WWLLN detections in the TGF FOV, should be consistent with the numbers calculated below.

The expected number of WWLLN detections in the TGF FOV, for a specific time interval, is the ratio of the "TGF FOV area", and the area covered by WWLLN, times the total number of WWLLN detections in that time interval.

The area of the TGF FOV is

$$A_{\text{TGF}} = \pi r^2 \quad (5.10)$$

where  $r = 1000$  km.

As most WWLLN detections are between  $\pm 40^\circ$  latitude in Figure 5.5, the area of the spherical segment covered by WWLLN is estimated by

$$A_{\text{WWLLN}} = 2(2\pi R^2 \sin \psi) \quad (5.11)$$

where  $R$  is the radius of the Earth, and  $\psi = 40^\circ$ . The ratio is then

$$\frac{A_{\text{TGF}}}{A_{\text{WWLLN}}} = \frac{r^2}{4R^2 \sin \psi} \approx \frac{1}{105} \quad (5.12)$$

That is, if the total number of WWLLN detections during some time is 10 000, the expected number of WWLLN detections in the TGF FOV is 95.

As AGILE orbits the Earth, any longitudinal difference in the WWLLN detections, is smoothed out.

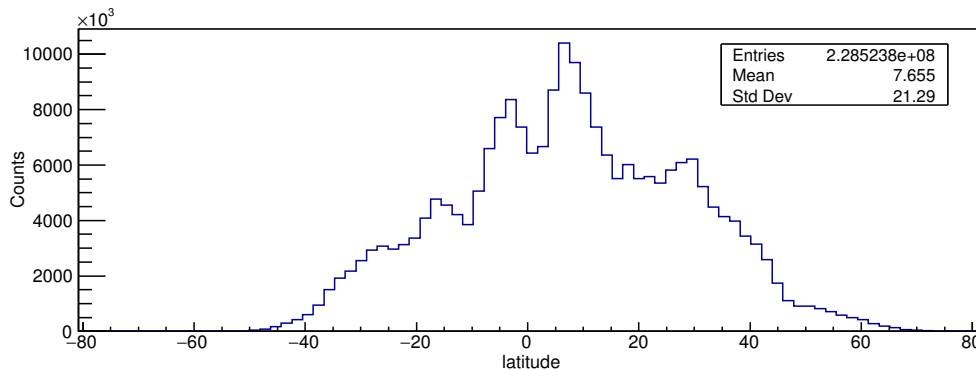


Figure 5.5: Latitude distribution of the WWLLN data for the year 2014.



## 5.5.2 Distance between WWLLN detection and sub-satellite point

In Section 3.8, the distance between the sub-satellite point and the WWLLN detection associated to a TGF is discussed. In this section we will show the distribution for *all* WWLLN detections with respect to the sub-satellite point. We will use the distribution for all WWLLN detections in the TGF FOV, and compare it to the distribution of TGF associated WWLLN detections in the next chapter: "Results and Discussions".

For all WWLLN detections inside the TGF FOV in the REF period, the distance from the sub-satellite point to the WWLLN detection is shown in Figure 5.6. This was expected to be a flat distribution, since the satellite position and the lightning detection are uncorrelated. From the figure, it is clear that there are more WWLLN detections far away than close to AGILE's sub-satellite point

The reason why there are more WWLLN detections far away, than close to AGILE's sub-satellite point, is shown in Figure 5.7. As AGILE's inclination angle is  $2.47^\circ$ , (also see Figure 4.4), the satellite will spend most of its time closer to  $0^\circ$  latitude. Then, according to Figure 5.7, most WWLLN detection is far away, than close to the sub-satellite point.

The bin size in Figure 5.6 is chosen so that the circular area corresponding to each bin is constant. This binning is the same for all "distance between sub-satellite point and WWLLN detection plots" in the Results chapter. The binning is obtained as follows:  $A_1 = \pi r_1^2 = \pi(r_2^2 - r_1^2) = \pi(r_3^2 - r_2^2) = \dots$  and so forth, where  $r_1$  is selected. In general  $A_n = \pi(r_n^2 - r_{(n-1)}^2)$ . Solving each equation for increasing  $r_n$  gives that  $r_n = \sqrt{(n+1)r_1^2}$ . Proving that the area of each bin always is constant:  $A_1 = \pi r_1^2 = A_n = \pi(r_n^2 - r_{(n-1)}^2) = \pi((n+1)r_1^2 - (n+1-1)r_1^2) = \pi(nr_1^2 + r_1^2 - nr_1^2) = \pi r_1^2$

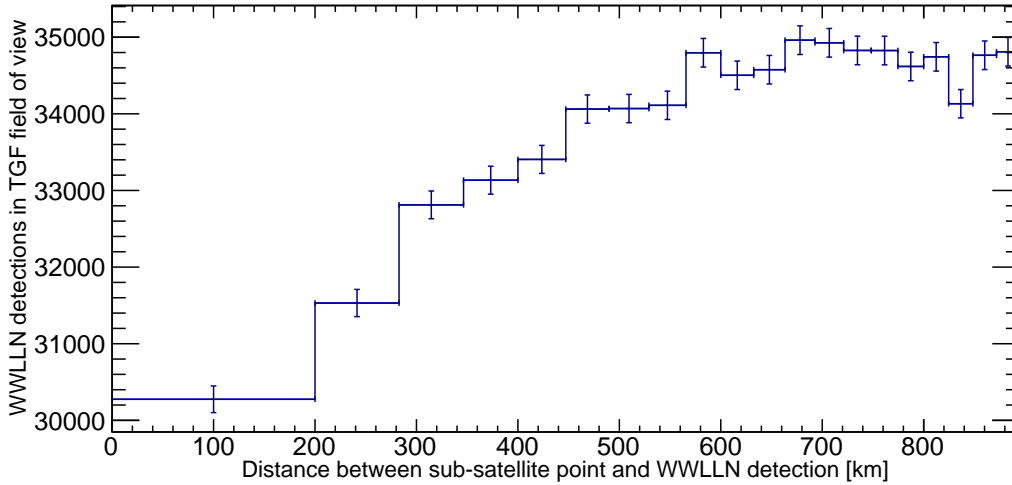


Figure 5.6: Number of WWLLN detections, as a function of distance from sub-satellite point to WWLLN detection, for the REF period.

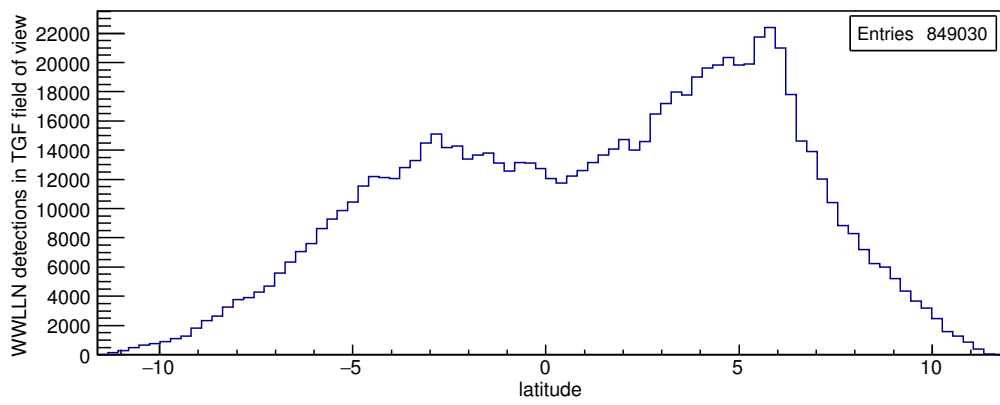


Figure 5.7: WWLLN detections, inside the TGF FOV, as a function of latitude for the REF period.

# Chapter 6

## Results and Discussions

This chapter describes the results from the GRID, AC-ON, REF, DRIFT and 3D-FIX period. A summary of the number of TGF candidates is given in Table 7.1. The TGF light curves and energy vs. time scatter plots, are found in the git repository "[https://github.com/andersbhm/Software\\_master\\_thesis](https://github.com/andersbhm/Software_master_thesis)" in the folder "Lightcurves".

### 6.1 GRID period

As mentioned in Section 4.2.3, the Gamma-Ray Imaging Detector (GRID) has an energy range from 30 MeV to 50 GeV, and a continuous data acquisition. The absolute timing accuracy is on  $\sim \mu\text{s}$  level, and the AC-system is always active on the GRID. The GRID period is between 01.06.2008 and 23.06.2015.

In this period, the WWLLN data includes  $1.22 \times 10^9$  detections. There are  $\sim 15.5$  million WWLLN detections in AGILE's TGF FOV. (This number is in the same order of magnitude as expected from Section 5.5.)  $\sim 4.5$  million of these WWLLN detections occur with a  $|\delta t| \leq 100$  ms (Equation 5.9) between the GRID and WWLLN detection. This is 29% of the total WWLLN detections in the TGF FOV. The number of WWLLN detections, and the GRID observing time is shown in Table 6.1.

The GRID observation time is estimated by binning the GRID data in a histogram with a bin size of 1 s. The number of filled bins is multiplied by 1 s to get the total observation time. The bin size of 1 s is selected as the average count rate is  $\sim 8$  cts/s. The observation time may be overestimated by 1 %. This is estimated by counting every time there are several empty bins after each other. The number of overestimated time in seconds is given by two times the number of empty bins periods, times the bin size.

Table 6.1: WWLLN and GRID data.

Number of WWLLN detections below satellite	Number of WWLLN detections associated with a GRID count	Total GRID observing time
15 539 760	4 554 872	116 630 888 sec

### 6.1.1 Stacking analysis

A stackplot of the GRID data for the 4 554 872 associated WWLLN detections is shown in Figure 6.1. There is no significant peak above the background. This can be explained by 1) the readout deadtime: only one photon can be detected for a 100  $\mu\text{s}$  long TGF. 2) energy range of the GRID: few photons are expected above  $\sim 30$  MeV from a TGF.

*Briggs et al.* [2013] found a TGF-lightning ratio of  $\sim 3.8 \times 10^{-4}$ . As there are 15.5 million WWLLN detections below the satellite during GRID observation, we should expect  $15.5 \times 10^6 \times 3.8 \times 10^{-4} = 5.9 \times 10^3$  TGFs. *Marisaldi et al.* [2010b] found 8 TGFs with GRID photons, compared to TGFs 119 with MCAL in the same period. This gives us a GRID efficiency of 6.7%, hence  $5.9 \times 10^3 \times 0.067 = 397$  expected TGF detections with GRID. As GRID is detecting only one photon from each TGF, we should see a signal of  $397/\sqrt{4050} = 6\sigma$ . However, high energy photons are expected to come from lightning close to the sub-satellite point (distance within  $\sim 400$  km). Expected amount of lightning producing photons detected by GRID is then  $15.5 \times 10^6 \times \frac{400^2}{1000^2} = 2.48 \times 10^6$ . Then the expected number of GRID photons is  $2.48 \times 10^6 \times 3.8 \times 10^{-4} \times 0.067 = 63$ . Which is  $1\sigma$ .

Shown in Figure 6.1, and given the calculation above, the stacking analysis is not identifying TGFs in the GRID dataset. Other selection strategies, like direction reconstruction, should be considered to enhance the signal to noise ratio.

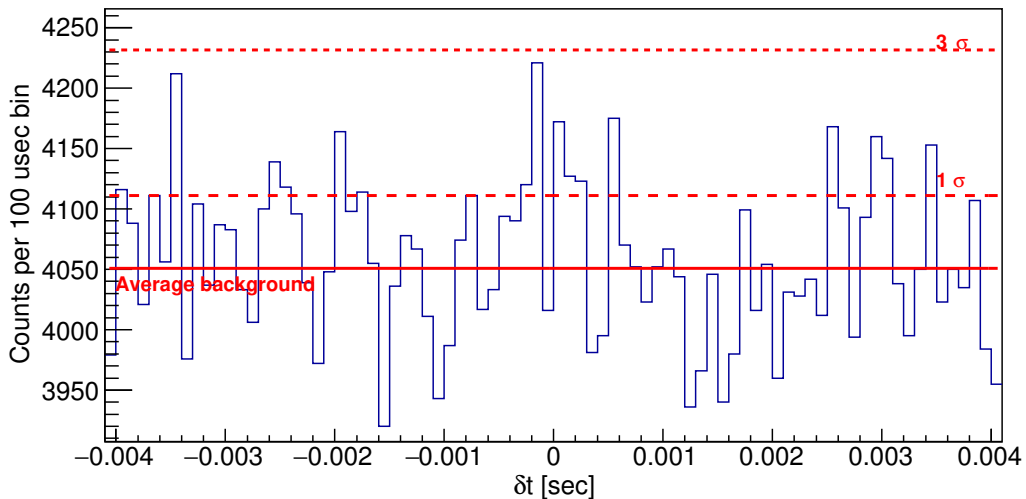


Figure 6.1: Stackplot of counts detected by GRID for 4 554 872 WWLLN detections.

### 6.1.2 Distance between the sub-satellite point and WWLLN detections

It is discussed in Section 3.8 and shown in Figure 6.13, that most of the WWLLN detections associated with TGFs, have a distance to the sub-satellite point within  $\sim 500$  km. As the stackplot in Figure 6.1 did not indicate any TGFs, the distance between the sub-satellite point and the WWLLN detection is plotted in Figure 6.2. The distances are for both GRID associated WWLLN detections, and all WWLLN detections in the TGF FOV. A GRID count may be associated with a WWLLN detection if  $|\delta t| \leq 500 \mu\text{s}$ .

The GRID counts associated to WWLLN detections within 200 km, are higher than for all WWLLN detections in the TGF FOV. The associated detections between 200 km and 350 km are lower. There is not a clear hint of TGFs in this plot, although *Marisaldi et al.*

[2010b] found, independent of WWLLN detections, 8 TGFs in the GRID data between June 2008 and December 2009 .

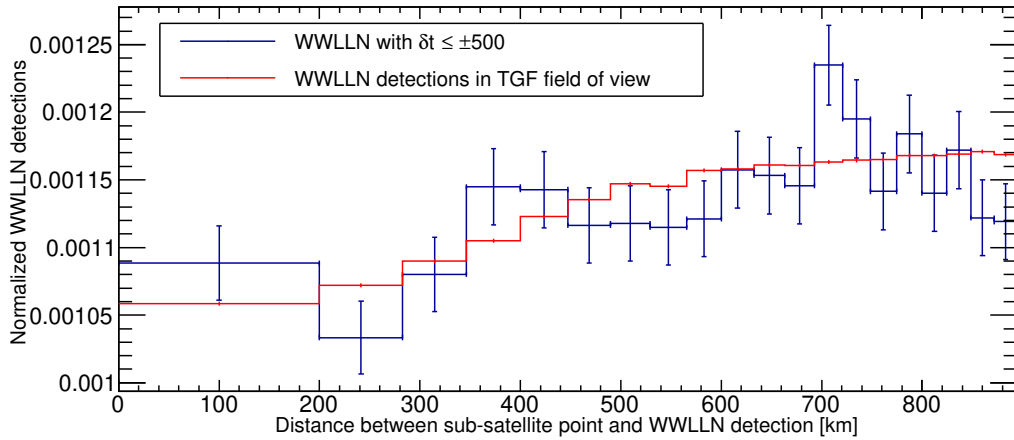


Figure 6.2: WWLLN detections associated with GRID counts in blue, and all WWLLN detections inside the TGF FOV in red. Each distribution is normalized to 1.

### 6.1.3 Reconstruction of particle direction

As the GRID dataset and the REF dataset overlap with three months, it is possible to compare these data. Comparing the GRID data with the TGFs found in the REF period (Section 6.3), there are two photons detected by GRID which match two different TGF candidates, in the MCAL data, within tens of microsecond. GRID can reconstruct particle directions  $\pm 60^\circ$  around the pointing direction of the instrument ( $\mathbf{Z}$  vector in Figure 6.3). Then, for GRID to be able to reconstruct the direction of the TGF associated photons, the angle  $v$ , between  $\mathbf{W}$  and  $\mathbf{Z}$  must be less than  $60^\circ$ .

GRID cannot provide a reliable direction reconstruction for the first photon as, if associated to the TGF,  $v = 130^\circ$ . The second photon has  $v = 48^\circ$  and should be investigated further, comparing the latitude and longitude of the associated WWLLN match and the projected production origin on Earth (or space), where the photon came from. If the photon is associated with the TGF, it should be traced back to the same latitude and longitude as the WWLLN match. This is beyond the scope of this thesis.

A total of two GRID photons were associated with TGFs out of 100 detected by MCAL (see Section 6.3). This is 2% compared to the 6.7% rate reported in *Marisaldi et al.* [2010b]. The lower percentage could be due to the fact that this analysis is based on WWLLN associations, which favours shorter events [Connaughton et al., 2013]. This makes it more likely that the AC-system prevents the photons from being detected by GRID.

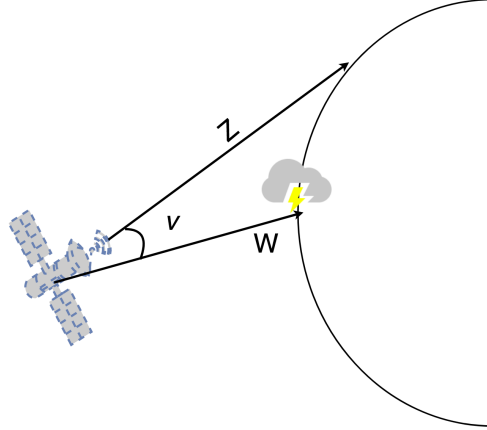


Figure 6.3: Illustration of AGILE and half the Earth.  $\mathbf{Z}$  is perpendicular to the detection plane of the GRID detector,  $\mathbf{W}$  is the direction towards the WWLLN detection, and  $v$  is the angle between  $\mathbf{Z}$  and  $\mathbf{W}$ .

## 6.2 AC-ON period

The AC-ON dataset is collected by the Mini-Calorimeter (MCAL), a gamma-ray detector with an energy range from 300 keV to 100 MeV. MCAL is operated in BURST-mode. The absolute timing accuracy is on  $\mu\text{s}$  level, and the AC-system is active on MCAL. The AC-ON period is between 17.01.2008 and 22.03.2015

In this period, the WWLLN data includes  $1.16 \times 10^9$  detections. There are  $\sim 14.7$  million WWLLN detections in AGILE's TGF FOV. (This number is in the same order of magnitude as expected from Section 5.5.)  $\sim 0.5$  million of these WWLLN detections are associated with MCAL with  $|\delta t| \leq 100$  ms between the MCAL and WWLLN detection. This is 3% of the total WWLLN detections in the TGF FOV. This percentage is much lower for MCAL than for GRID, as GRID has continuous data collection, while MCAL is triggered. The number of WWLLN detections, and MCAL observation time is shown in Table 6.2.

The MCAL observation time is calculated by binning the MCAL data in a histogram with a bin size of 20 ms. The number of filled bins is multiplied by 20 ms to get the total observation time. The bin size of 20 ms is selected as the average count rate is 400 cts/s. In a 20 ms bin, there is an average of 8 counts which gives a low probability of a zero bin when MCAL is observing. The observation time may be overestimated by 1 %.

Table 6.2: WWLLN and MCAL data.

Number of WWLLN detections below satellite	Number of WWLLN detections associated with MCAL	Total MCAL observation time
14 677 795	496 993	1 832 583 sec

### 6.2.1 Stacking analysis

A stackplot of the MCAL data for 496 993 associated WWLLN detections is shown in Figure 6.4. There is no significant peak visible at  $\delta t \approx 0$  in Figure 6.4. The AC-system is completely suppressing the TGF signal as we have  $14.7 \times 10^6 \times 3.8 \times 10^{-4} = 5586$  expected TGFs (number of lightning times the TGF-lightning ratio). As  $1\sigma = 144$  counts, the signal should be clearly visible.

The absence of TGF signal is in agreement with *Marisaldi et al.* [2014], and is explained by the AC-induced dead time, which prevents the detection of brief TGFs, mostly associated with lightning.

As the two stackplots from the GRID and AC-ON period are for approximately the same time period, one could expect them to have the same average background. This is not the case as the two detectors, MCAL and GRID, have different count rate and different exposure time. MCAL is triggered, i.e. data stream is not continuous as for the GRID. The average count rate for GRID is  $\sim 8$  cts/s, and the average count rate for MCAL in the AC-ON dataset is  $\sim 400$  cts/s. The ratio between the count rates is 50.

In Figure 6.1, the average background for the GRID is 4050 counts per 100  $\mu\text{s}$  per WWLLN detection. In Figure 6.4, the average background for MCAL is 20 625 counts per 100  $\mu\text{s}$  per WWLLN detection. There are  $\sim 4.5$  million WWLLN detections in the GRID stackplot and  $\sim 0.5$  million WWLLN detections in the MCAL stackplot. The ratio is then

$$\frac{20625/0.5}{4050/4.5} = 46 \quad (6.1)$$

which is reasonable compared to the estimated ratio of 50.

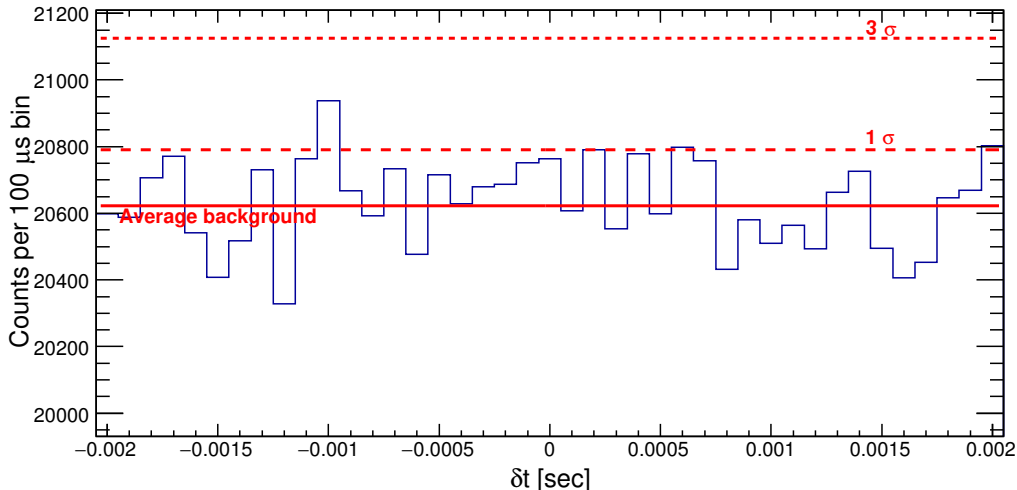


Figure 6.4: Stackplot of counts detected by MCAL for 496 993 WWLLN detections.

## 6.2.2 Distance between the sub-satellite point and WWLLN detections

Figure 6.5 shows the distance between the sub-satellite point for WWLLN detections with  $|\delta t| \leq 500 \mu\text{s}$  (blue), and distance for all WWLLN detections in the TGF FOV (red). Sferics associated with TGFs usually have a distance within  $\sim 350 \text{ km}$ . We can see that the MCAL associated WWLLN detections are higher than for all WWLLN detections in the TGF FOV, within  $\sim 300 \text{ km}$ . This may be a hint of TGFs in these data.

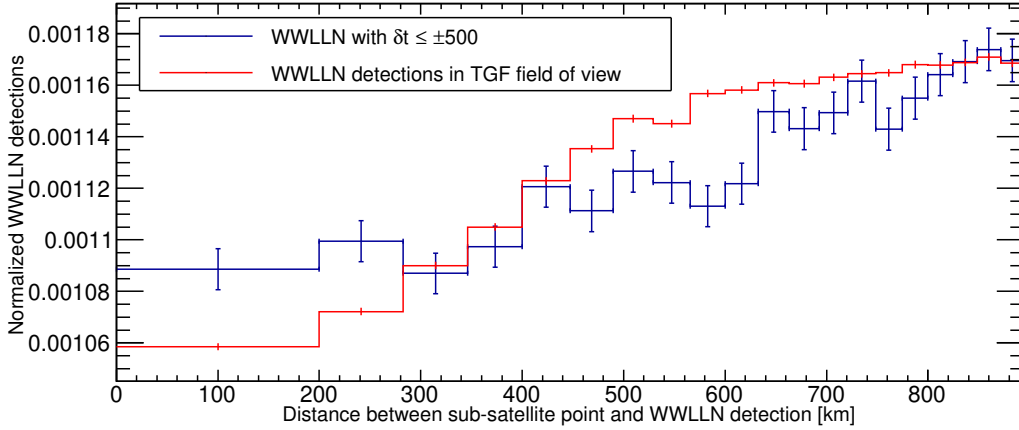


Figure 6.5: WWLLN detections associated with MCAL counts in blue, and all WWLLN detections in the TGF FOV in red. Each distribution is normalized to 1.

Motivated by Figure 6.5, a new stackplot was calculated, including only WWLLN detections within 280 km from the sub-satellite point. This is shown in Figure 6.6, showing a  $3\sigma$  significant signal at  $\delta t = -0.5 \text{ ms}$ , which should be further investigated.

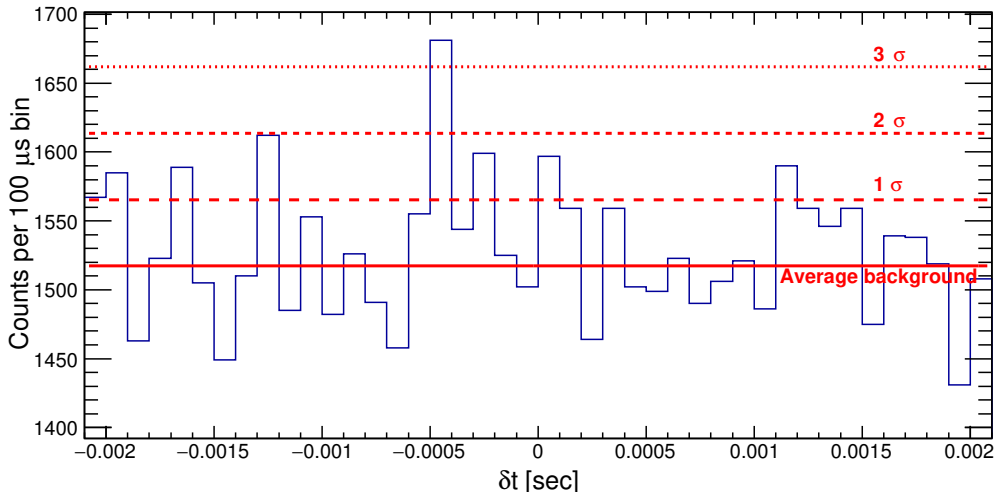


Figure 6.6: Stackplot of counts detected by MCAL for WWLLN detections within 280 km from the sub-satellite point.



### 6.3 REF period

The REF period dataset is collected by MCAL operated in BURST-mode. The difference from the AC-ON period, is that the AC-system is disabled for MCAL. This results in a deadtime of  $\sim 20 \mu\text{s}$  for each of the 30 scintillator bars. The absolute timing accuracy is on  $\mu\text{s}$  level. The REF-period is between 23.03.2015 and 23.06.2015.

In this period, the WWLLN data includes  $62 \times 10^6$  detections. The WWLLN data associated with MCAL data is shown in Table 6.3. There are 849 030 WWLLN detections in the TGF FOV. This number is in the same order of magnitude as expected from Section 5.5.

The number of WWLLN detections which is associated with the MCAL data ( $|\delta t| \leq 100 \text{ ms}$ ), is 9202. This is 1% of the total WWLLN detections in the TGF FOV. In the AC-ON period this percentage is 3%. As MCAL in the REF period is optimized for detecting TGFs, this percentage is expected to be higher compared to the AC-ON period. The difference in the REF period, compared to the AC-ON period, is that WWLLN steadily increased its detection efficiency between the years 2008 to 2013 (Table 4.1). The average number of WWLLN detections per year in the AC-ON period is lower compared to the REF period. This results in a lower fraction of WWLLN detections associated with MCAL, divided by all the WWLLN detections in the TGF FOV for the REF period.

The observation time of the MCAL is calculated by binning the MCAL data in a histogram with a bin size of 10 ms. The number of filled bins was multiplied by 10 ms to get the total observation time. The bin size of 10 ms is selected as the average count rate is  $\sim 600 \text{ cts/s}$ . In a 10 ms bin, there is therefore an average of 6 counts which gives a low probability of a zero bin when MCAL is observing. The observation time may be overestimated by 0.2 %.

The increased count rate from 400 cts/s in the AC-ON period to 600 cts/s in the REF period, is due to charged particles being not rejected by the AC-system anymore.

#### 6.3.1 Stacking analysis

Figure 6.7 shows the stackplot of the MCAL data. The significance of the peak at  $\delta t \approx 0$  is  $24.6\sigma$ , and shows a clear connection between sferics and TGFs. This is further evidence that the AC-system was preventing detection of short-duration gamma-ray bursts, associated to lightning.

The energy of the counts in Figure 6.7 is shown in Figure 6.8. The peak at  $\delta t \approx 0$  indicates the energy range of photons associated with the TGFs, but is not corrected for background, deadtime and eventually other instrumental effects. Though, the energy range is in agreement with *Dwyer and Smith* [2005] and *Marisaldi et al.* [2015].

Figure 6.9 is the same as the plot in Figure 6.7, except that known TGFs from the 2nd AGILE TGF catalog ([www.asdc.asi.it/mcaletgfcats/](http://www.asdc.asi.it/mcaletgfcats/)) are not included. The significance of the peak is  $13.9\sigma$ . This shows that not all TGFs with a WWLLN association are found by the selection algorithm used in *Marisaldi et al.* [2015].

Table 6.3: WWLLN and MCAL data.

Number of WWLLN detections below the satellite	Number of WWLLN detections associated to MCAL	Total MCAL observation time
849 030	9202	86 113 sec

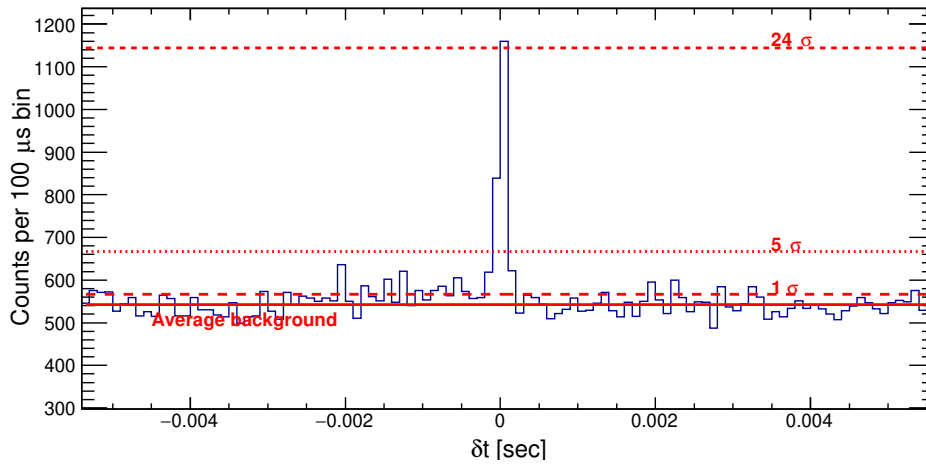


Figure 6.7: Stackplot of MCAL counts for 9 045 WWLLN detections.

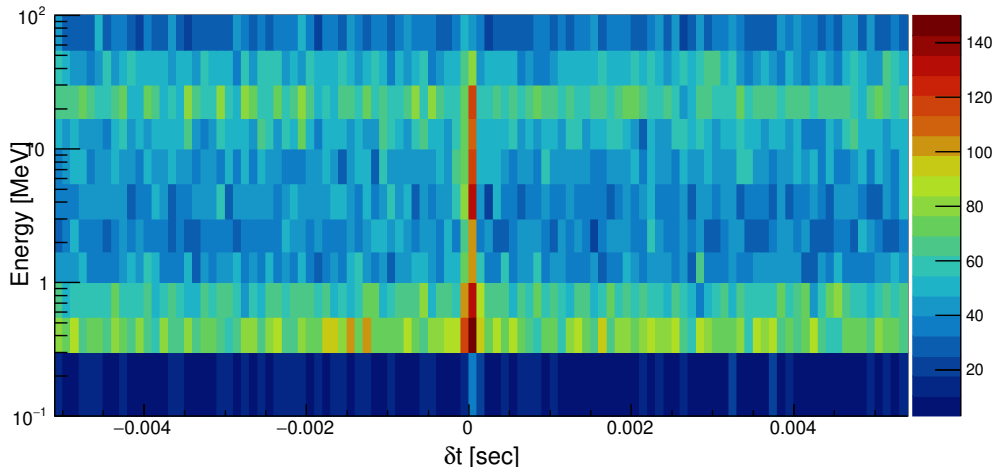


Figure 6.8: Energy of the counts in Figure 6.7, detected by MCAL. The unit of the color scale is counts per 100  $\mu$ s per energy bin.

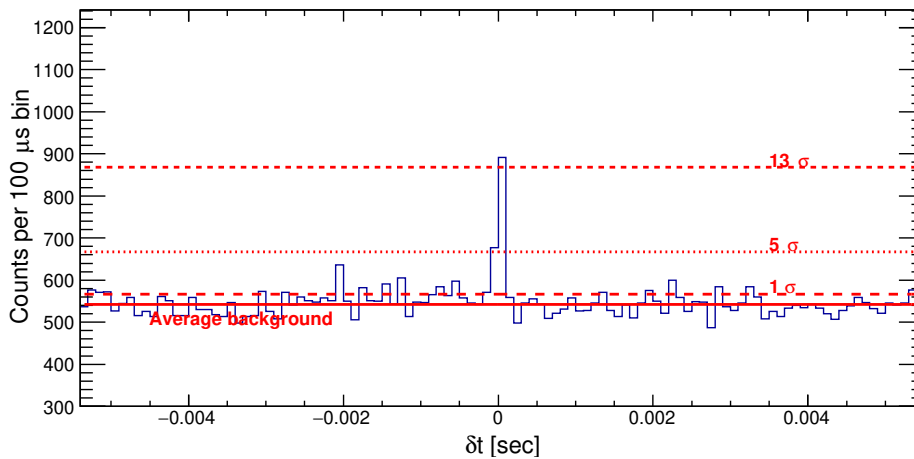


Figure 6.9: Same stackplot as in Figure 6.7 except that known TGFs from the 2nd AGILE TGF catalog are excluded.

### 6.3.2 Identifying TGFs using the search for cluster analysis

The search for cluster analysis (Section 5.4) is used to identify the TGFs in the previous stacking analysis. Figure 6.10 and Table 6.4 are used to determine the best counts per 100  $\mu\text{s}$  bin threshold. The signal includes counts with  $|\delta t| \leq 500 \mu\text{s}$ , and the background includes counts with  $\delta t$  between 3.2 and 3.7 seconds. The Background/Signal fraction is the fraction of the integral of the background and signal, from the selected threshold to 20 counts per 100  $\mu\text{s}$  bin. A threshold of 4 counts per 100  $\mu\text{s}$  bin is selected as this gives 101 TGFs candidates with 2% background to signal ratio. A threshold of 3 counts per 100  $\mu\text{s}$  bin is not used as this gives a large fraction of false positives due to background fluctuation. This is clear from a background to signal ratio of 21% in Table 6.4.

One should note that the distributions in Figure 6.10 are counts per 100  $\mu\text{s}$  bin. Therefore the TGF signal may be distributed in several bins and be underestimated. However, this is also the case for the background signal.

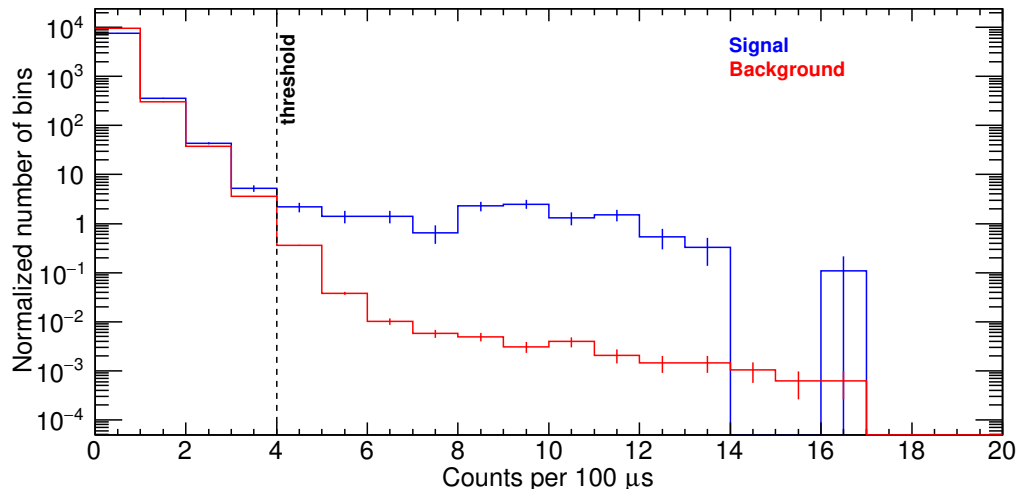


Figure 6.10: Distribution of counts per 100  $\mu\text{s}$  time bin for the REF period. The signal includes counts with  $|\delta t| \leq 500 \mu\text{s}$  and is normalized per 1 ms per 9202 WWLLN detection. The background includes counts with  $\delta t$  between 3.2 and 3.7 seconds and is normalized per 0.5 s per 9670 WWLLN detection.

Table 6.4: The threshold is minimum counts per 100  $\mu\text{s}$ . The time window is the  $\delta t$  interval around the WWLLN detection. The fraction of background/signal, is the ratio of the two integrals from the selected threshold to 20 counts per 100  $\mu\text{s}$ , of the background and signal in Figure 6.10.

Threshold	Time window	TGF candidates	Fraction Background/Signal
3	$\pm 500 \mu\text{s}$	142	0.21
4	$\pm 500 \mu\text{s}$	101	0.03
5	$\pm 500 \mu\text{s}$	96	0.008

In Figure 6.11, the TGF candidates with threshold = 4 is binned in a histogram as a function of  $\delta t$ . By manually checking each light curve and energy vs. time scatter plot of the 101 TGF candidates, 100 seems very likely to be TGFs. 43 of the 100 TGFs are already identified by *Marisaldi et al.* [2015], using TGF selection criteria independent of WWLLN. The plots of the 57 new TGF are found in the git repository in the

folder "Lightcurves/REF". The 43 already identified TGFs are in the subfolder named "also\_found\_by\_Marisaldi".

One of the TGF candidates were counted twice as there were more than 100 us between two associated WWLLN detections, corrected for propagation time. (See step 3 in Section 5.1.) This resulted in two WWLLN detections associated with the same TGF.

As there are 100 TGFs detected, during 93 days, using only correlation with WWLLN, we obtain  $\sim 1$  TGF per day. *Marisaldi et al.* [2015] found 279 TGFs in the same period, based on TGF selection criteria independent of WWLLN, obtaining  $\sim 3$  TGFs per day. 45 of 279 TGFs had a WWLLN association. As this analysis detects more than twice WWLLN associated TGFs as *Marisaldi et al.* [2015], it indicates that their TGF selection criteria are too strict. If a new set of selection criteria is developed based on already found TGFs, including the new 57 TGFs, it may be possible to obtain a new detection rate of maximum 6 TGFs per day in this period. This is discussed in chapter 7.

Figure 6.12 shows the same stackplot as in Figure 6.7, except that the 101 TGF candidates, found by the search for cluster analysis, are excluded. It is evident that there is no significant TGF signal left associated with the 9202 WWLLN sferics. This suggests that the proposed search algorithm identifies all TGFs associated to WWLLN sferics in the dataset.

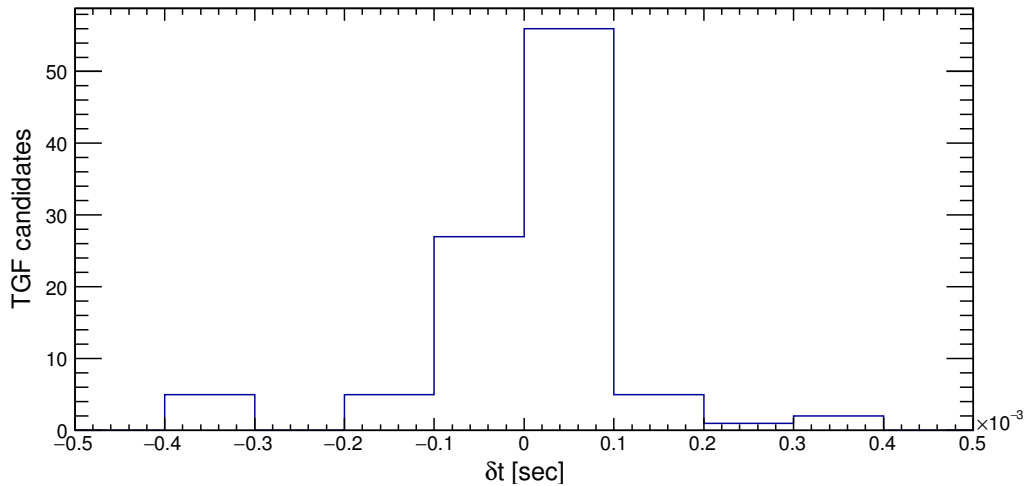


Figure 6.11: TGF candidates with threshold = 4. There are 101 TGF candidates with  $|\delta t| \leq 500 \mu\text{s}$ . The bin size is  $100 \mu\text{s}$ . A Gaussian fit gives a sigma of  $\sigma = 60 \mu\text{s}$

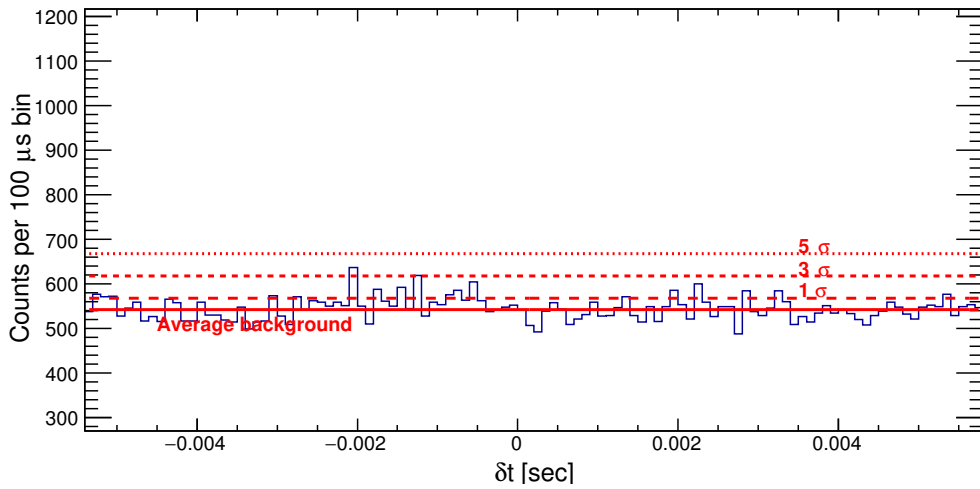


Figure 6.12: Same stackplot as in Figure 6.7 except that the 101 TGF candidates, found by the search for cluster analysis, are removed.

### 6.3.3 Distance between the sub-satellite point and WWLLN detections

Figure 6.13 shows the WWLLN detections associated with the 101 TGF candidates binned as a function of distance from the sub-satellite point. All WWLLN detections in the TGF FOV are also shown in red. The WWLLN detections, associated with MCAL counts, are closer to the sub-satellite point than the approximately flat distribution from all the WWLLN detections in the TGF FOV. It is clear that most of the WWLLN TGF matches are within  $\sim 350$  km from the sub-satellite point, as discussed in Section 3.8.

The two outliers in Figure 6.13, with distance from the sub-satellite point larger than 700 km, are shown in Figure 6.14 and 6.15. Both outliers seem to be TGFs.

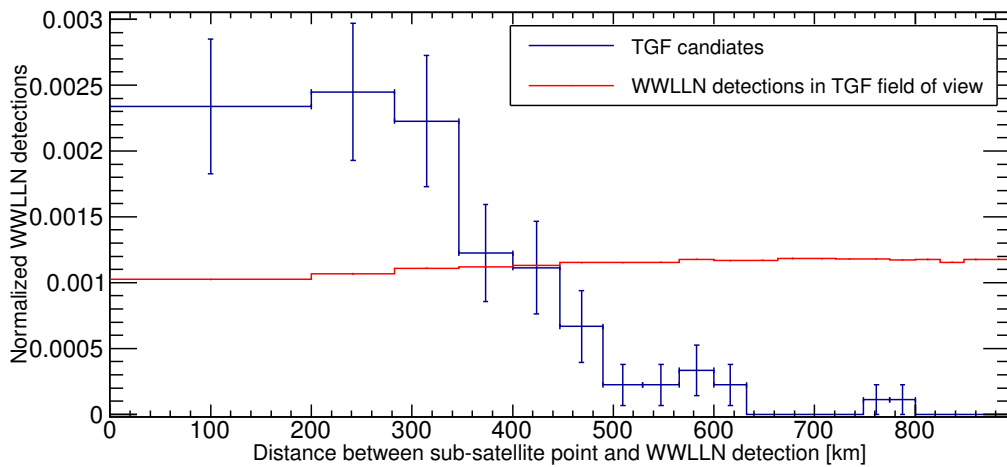


Figure 6.13: Number of TGF candidates, as a function of distance from the sub-satellite point to WWLLN detection, and all the WWLLN detections in the TGF FOV. Each distribution is normalized to 1.

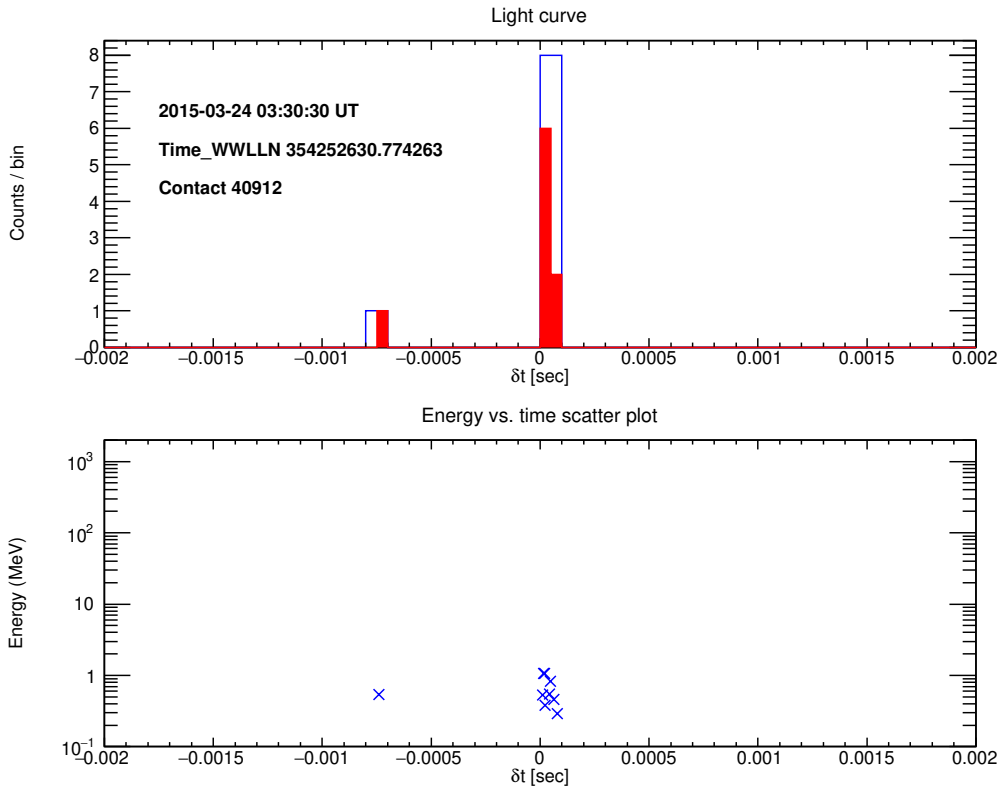


Figure 6.14: Outlier with distance 775 km from the sub-satellite point in Figure 6.13. The light curve has a blue bin size of 100  $\mu$ s, and a red bin size of 50  $\mu$ s.

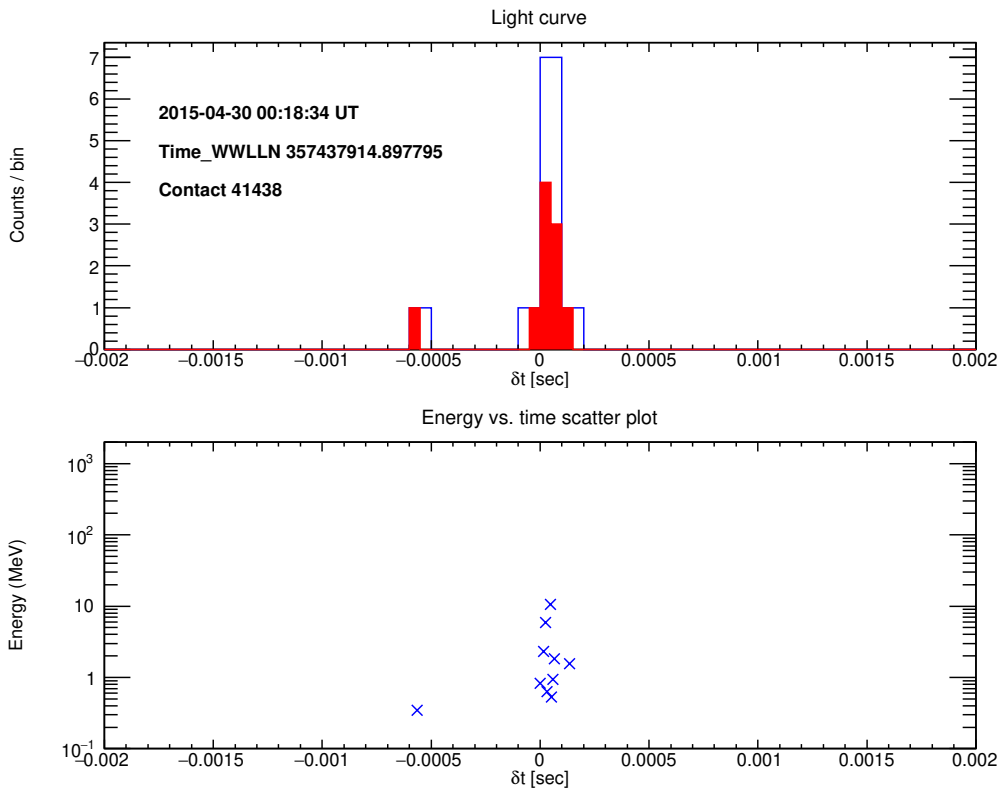


Figure 6.15: Outlier with distance 763 km from the sub-satellite point in Figure 6.13. The light curve has a blue bin size of 100  $\mu$ s, and a red bin size of 50  $\mu$ s.

A double TGF is shown in Figure 6.16. Note that the WWLLN detection is associated with the last TGF peak. This is in agreement with the observations by *Mezentsev et al.* [2016] which reported that in 16 out of 16 double TGFs investigated, the radio signal associated with a lightning flash, always is closer to the last TGF peak. A clear explanation for this is not available yet. Note the high energy counts associated to the 2nd peak, up to 100 MeV. This can be a result of pile-up of lower energy photons [*Marisaldi et al.*, 2018].

Double TGFs are counted as one TGF in this analysis, as they have only one associated WWLLN detection.

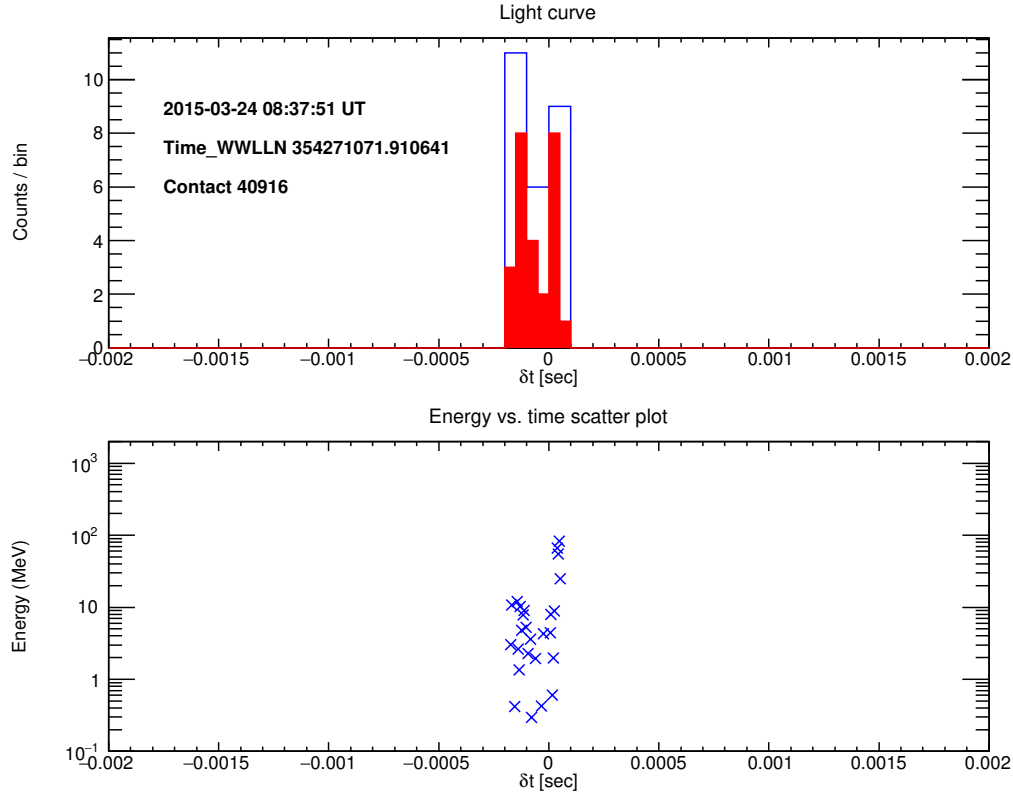


Figure 6.16: A double TGF. The distance to the sub-satellite point is 106 km. The light curve has a blue bin size of 100  $\mu$ s, and a red bin size of 50  $\mu$ s.

### 6.3.4 TGF-lightning ratio in the REF period

There are 100 TGFs identified in this dataset, and there are 9202 WWLLN detections associated with MCAL. The TGF-lightning ratio considering these numbers would be enormous compared to  $3.8 \times 10^{-4}$  TGF-lightning ratio reported in *Briggs et al.* [2013]. However, this would not be correct, as MCAL data is triggered and therefore is more likely to trigger if the lightning produces a TGF.

As most WWLLN associated TGFs occur within a 350 km distance between the sub-satellite point and the WWLLN detection (See Figure 6.13), we will consider the WWLLN associated TGFs and all WWLLN detections inside this radius. Within 350 km, there are 63 WWLLN associated TGFs, and a total of 96 678 WWLLN detections. The TGF-lightning ratio is then  $6.5 \times 10^{-4}$ . For 500 km it is  $4.3 \times 10^{-4}$  and for 600 km it is  $3.2 \times 10^{-4}$ . The values are compatible with  $3.8 \times 10^{-4}$  obtained for Fermi [*Briggs et al.*, 2013]. These are lower limits as there might be more TGFs, not detected at satellite altitude.

### 6.3.5 Timing offset analysis

The TGF candidates found in this thesis are always associated with a WWLLN detection per definition of the analysis. ( $|\delta t| \leq 500 \mu\text{s}$  or 20 ms, to be a TGF candidate, depending on the dataset.)  $\delta t$ , plotted as a function of time for events with number of counts larger than the threshold, should appear as a straight line  $\delta t \approx 0$  with no slope. This is evident in the REF dataset shown in Figure 6.17. The TGF candidates form a clear pattern at  $\delta t \approx 0$ , while background fluctuations seem randomly distributed forming no clear pattern. The Contact number on the x-axis is the number of orbits AGILE has done. As each orbit is  $\sim 92$  minutes, the number of contacts is a proxy for elapsed time.

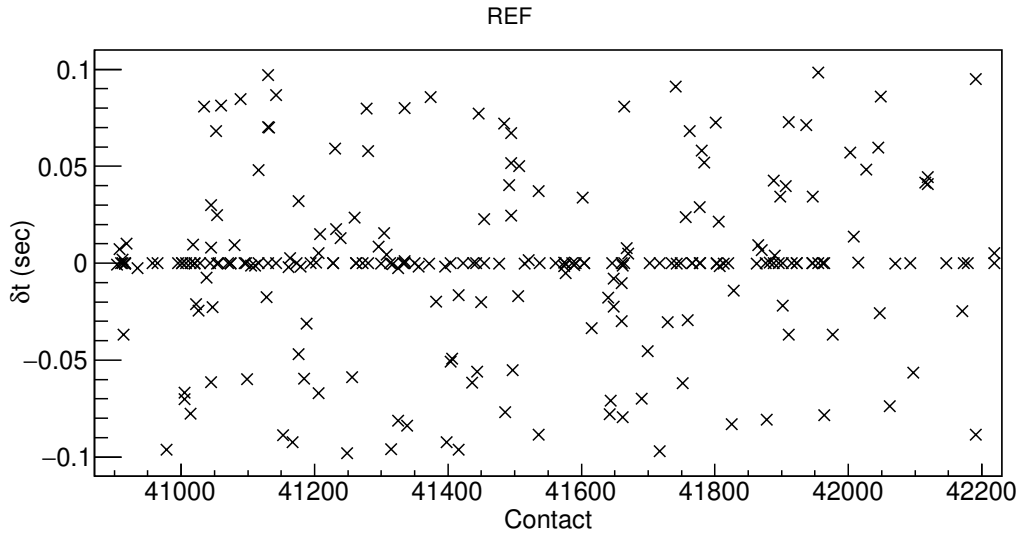


Figure 6.17: REF dataset. Events with threshold = 5. The absolute timing accuracy is on  $\mu\text{s}$  level, and the TGF candidates have a  $\delta t \approx 0$ . The outliers are background fluctuations.



## 6.4 DRIFT period

The DRIFT period dataset is collected by MCAL operated in BURST-mode, with a disabled AC-system. The difference, with respect to the REF period, is that an issue in the onboard GPS caused a degradation in the absolute timing accuracy. The onboard time for this dataset is drifting, but is corrected using housekeeping data. The timing accuracy is therefore assumed to be on ms level. The DRIFT period is between 01.01.2016 and 09.11.2017.

During this period the WWLLN data includes  $390 \times 10^6$  detections. The WWLLN data associated with MCAL data are shown in Table 6.5. There are 4 808 584 WWLLN detections in the TGF FOV. This number is in the same order of magnitude as expected from Section 5.5.

The number of WWLLN detections which is associated with the MCAL data ( $|\delta t| \leq 100$  ms), is 175 129. This is 3.6 % of the WWLLN detections in the TGF FOV. In the REF period this percentage is 1%. The change is due to a configuration change implemented in order to maximize the available telemetry from AGILE. The average count rate has increased from  $\sim 600$  cts/s in the REF period, to  $\sim 700$  cts/s in the DRIFT period.

The observation time of the MCAL is calculated by binning the MCAL data in a histogram with a bin size of 10 ms. The number of filled bins was multiplied by 10 ms to get the total observation time. The bin size of 10 ms is selected as the average count rate is 700 cts/s. In a 10 ms bin, there is therefore an average of 7 counts which gives a low probability of a zero bin when MCAL is observing. The expected MCAL observation time is  $\sim 700\,000$  second if we scale the observation time in the REF period (Table 6.3) to two years. As the observation time is 2 743 686, the difference is due to a configuration change implemented in order to maximize the available telemetry from AGILE, discussed above. The observation time may be overestimated by 0.2 %.

Table 6.5: WWLLN and MCAL data.

Number of WWLLN detections below satellite	Number of WWLLN detections associated to MCAL	Total MCAL observation time
4 808 584	175 129	2 743 686 sec

### 6.4.1 Stacking analysis

Figure 6.18 shows no significant peak at  $\delta t \approx 0$ . This is probably due to the millisecond timing accuracy onboard AGILE. Hence, any potential significant number of counts is spread over a large time interval. There is no visible peak, selecting both larger and smaller bin sizes.

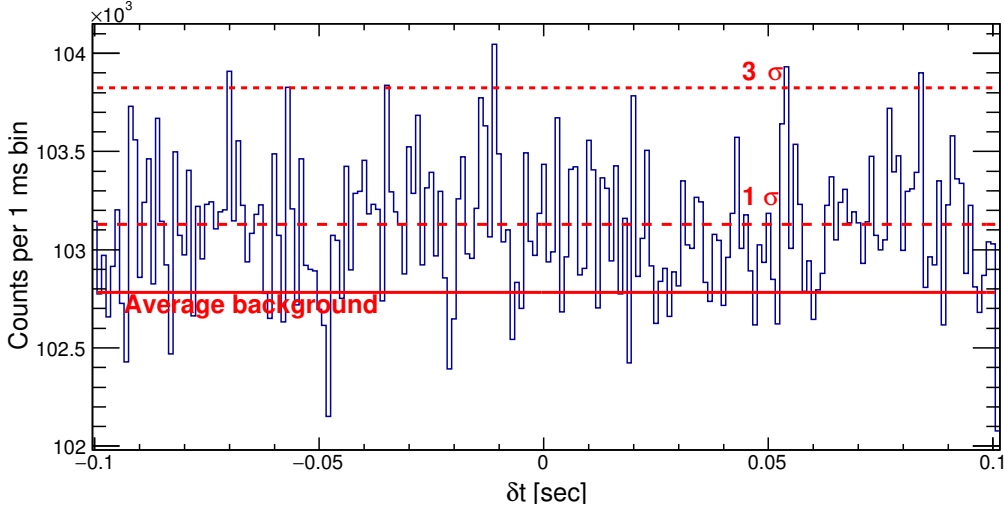


Figure 6.18: Stackplot of MCAL counts for 175 129 WWLLN detections.

### 6.4.2 Identifying TGFs using the search for cluster analysis

As the standard stacking analysis had negative results, the "search for cluster method" was developed. It is described in Section 5.4. The idea is to look at light curves and only keep histogram bars with high counts per  $100 \mu\text{s}$  bin. This increases the chance of identifying TGFs, as they are bright events associated with several counts per unit time, compared with the background radiation.

The distribution of counts per  $100 \mu\text{s}$  time bin, for both the TGF signal and the background, are shown in Figure 6.19. Based on Figure 6.19 and Table 6.6, a threshold of 7 counts per  $100 \mu\text{s}$ , and a time window of  $|\delta t| \leq 20 \text{ ms}$  around each WWLLN detection, is selected. This gives 302 TGF candidates, with a background to signal ratio of 37%. The false positive TGFs are sorted out at a later stage. The number of TGF candidates, the background to signal noise ratio for different thresholds, and time windows, are shown in Table 6.6.

In Figure 6.20, events with threshold = 7 are binned in a histogram as a function of  $\delta t$ . The TGF candidates have  $|\delta t| \leq 20 \text{ ms}$ . As a Gaussian fit to this distribution gives  $\sigma \approx 20 \text{ ms}$ , it is clear that the actual timing uncertainty is much larger than the 1-5 ms timing accuracy previously reported in Section 4.3.4.

By manually checking each light curve, and the energy vs. scatter plot, of the 302 TGF candidates, 300 seems likely to be TGFs. The 300 new TGF light curve and scatter plots are found in the git repository in the folder "Lightcurves/DRIFT".

Two of the TGF candidates were counted twice as there were more than 100  $\mu\text{s}$  between two associated WWLLN detections, corrected for propagation time. (See step 3 in Section 5.1.) This resulted in two WWLLN detections associated with the same TGF.

As all the 302 TGF candidates appear to be TGFs, the estimated 37% background in Table 6.6 is largely overestimated as it is closer to 0. As the TGF signal is normalized per 40 ms instead of 1 ms as in the REF period, this reduces the signal by a factor 1/40. There may also be that there are TGFs in the background signal, as it is not clear how large the time drift offset can be. Considering the background to signal ratio is largely overestimated, a lower threshold should be considered in the future. This will add a maximum of 109 new TGFs with 6 counts per 100  $\mu$ s.

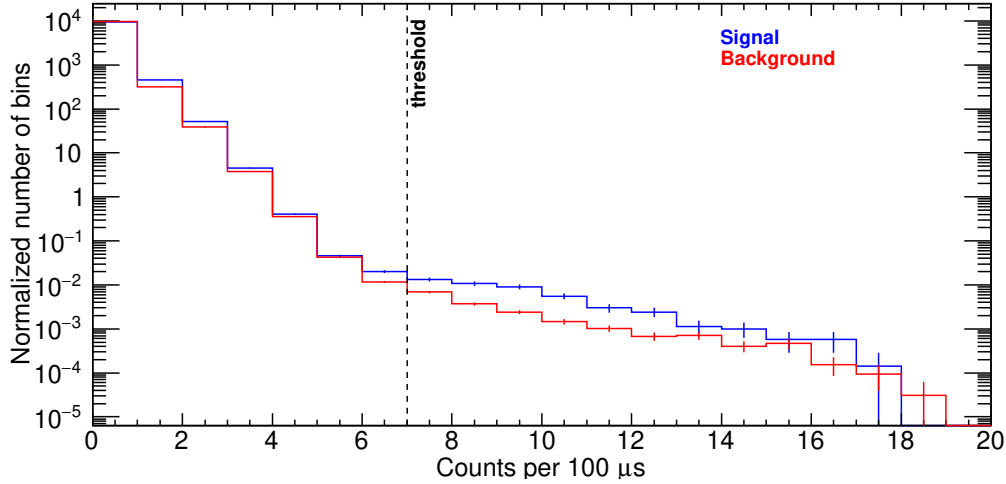


Figure 6.19: Distribution of counts per 100  $\mu$ s time bin for the DRIFT dataset. The signal includes counts with  $|\delta t| \leq 20$  ms, and is normalized per 40 ms per 175 129 WWLLN detections. The background includes counts with  $\delta t$  between 3.2 and 3.7 s, and is normalized per 0.5 s per 64 559 WWLLN detections.

Table 6.6: The threshold is minimum counts per 100  $\mu$ s. The time window is  $\delta t$  around the WWLLN detection. The fraction of background/signal, is the ratio of the two integrals, from the selected threshold to 20 counts per 100  $\mu$ s, of the background and signal in Figure 6.19.

Threshold	Time window	TGF candidates	Fraction Background/Signal
5	$\pm 10$ ms	381	0.57
6	$\pm 10$ ms	243	0.36
7	$\pm 10$ ms	187	0.30
8	$\pm 10$ ms	135	0.26
6	$\pm 20$ ms	411	0.43
<b>7</b>	$\pm 20$ ms	<b>302</b>	<b>0.37</b>
8	$\pm 20$ ms	218	0.32
9	$\pm 20$ ms	148	0.31
10	$\pm 20$ ms	93	0.34
9	$\pm 50$ ms	234	0.50
10	$\pm 50$ ms	152	0.53

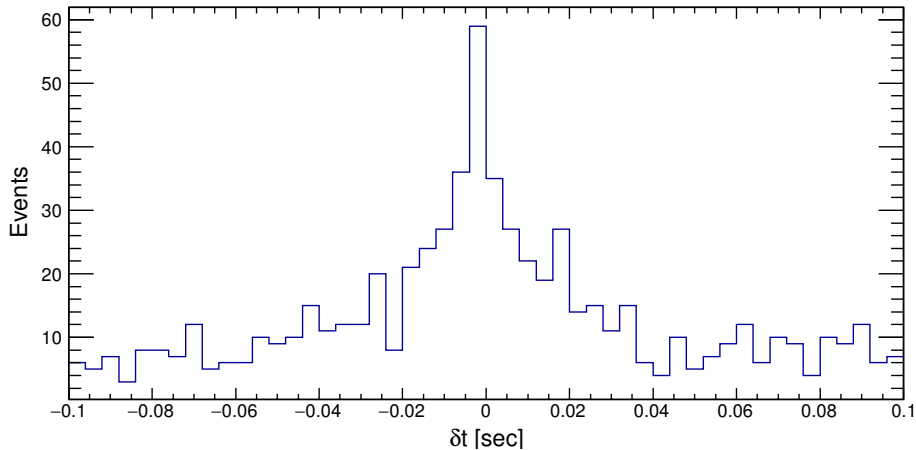


Figure 6.20: Events with threshold = 7. There are 302 TGF candidates between  $-20$  and  $20$  ms. The bin size is 4 ms. A Gaussian fit gives a sigma of  $\sigma \approx 20$  ms

### 6.4.3 Distance between the sub-satellite point and WWLLN detections

Figure 6.21 shows the WWLLN detections associated with the 302 TGF candidates, binned as a function of distance from the sub-satellite point. All the WWLLN detections in the TGF FOV are shown in red. The distribution of the TGF candidates shows that these candidates probably are TGFs, as it is a similar distribution as in Figure 6.13 for the REF period. The larger distribution, outside 500 km in the DRIFT period, can be explained by that the DRIFT period consists of two years of data, while the REF period consists of only three months.

The distribution in Figure 6.21, together with a manual inspection of the lightcurves belonging to each TGF candidate, is a clear indication that these candidates actually are TGFs, and that the search for cluster method works. We conclude that TGFs can be identified with a close to WWLLN detection in this dataset, despite the low onboard timing accuracy. This provides the opportunity to correct the timing of the drift dataset down to accuracies of 100  $\mu$ s. This is discussed further in chapter 7.

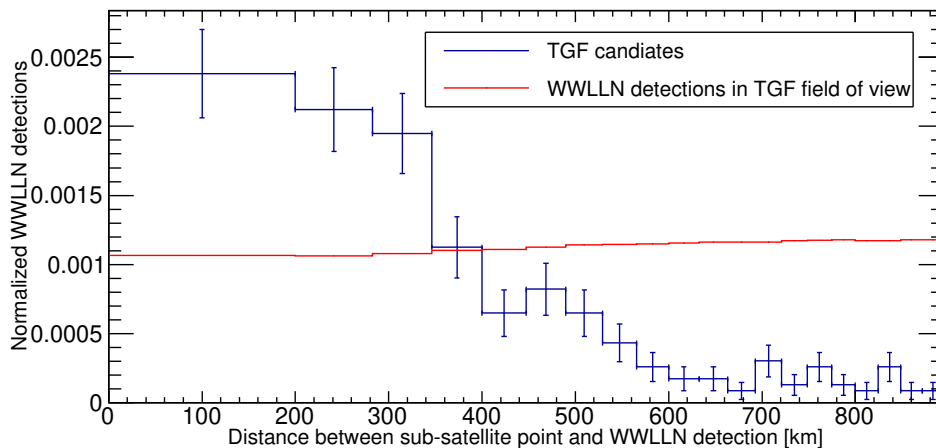


Figure 6.21: Number of TGF candidates, as a function of distance from the sub-satellite point to WWLLN detection, and all the WWLLN detections in the TGF FOV. Each distribution is normalized to 1.

#### 6.4.4 Comparing the background in REF and DRIFT periods

A comparison of the distribution of counts per  $100\ \mu\text{s}$ , for the REF and DRIFT dataset, is shown in Figure 6.22. The distributions are normalized per time window duration, and per number of WWLLN detections. The REF signal is much higher than the DRIFT signal as the timing uncertainty, and therefore the time window defining the REF signal, is much smaller. Note that the background, for counts per  $100\ \mu\text{s}$  larger than 8, in the REF period is significantly larger compared with the "DRIFT background". This is now addressed: The average count rate for the REF data is  $\sim 600\ \text{cts/s}$ , and the average count rate for the DRIFT data is  $\sim 700\ \text{cts/s}$ . The background distribution should therefore be smaller in the REF data compared with the DRIFT data, not opposite.

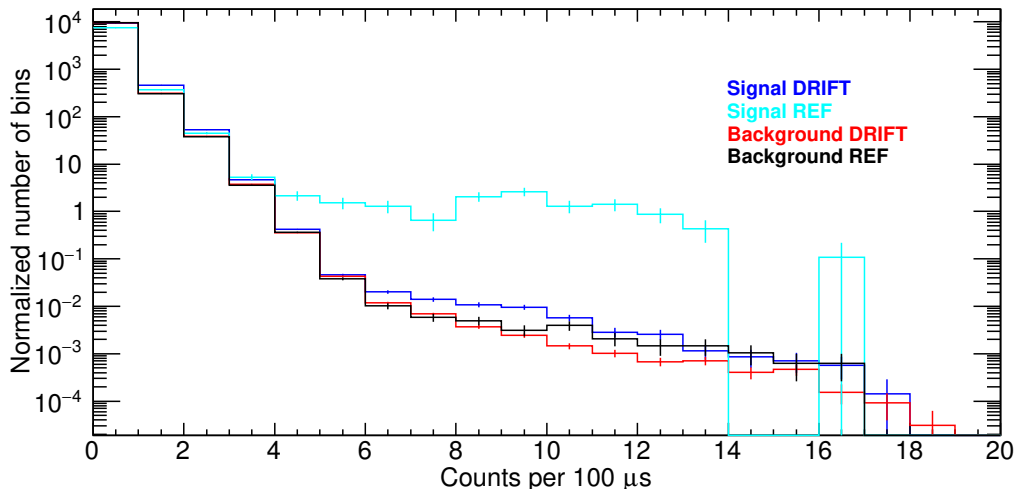


Figure 6.22: Distribution of counts per  $100\ \mu\text{s}$  time bin, comparing the DRIFT dataset (Figure 6.19) and the REF dataset (Figure 6.10).

This is investigated further in Figure 6.23, where the background for the REF period and the background for the DRIFT dataset, between 23.03. - 23.06.2016, are compared. (This is the same season for the DRIFT as for the REF, but for year 2016 instead of 2015.) As the "DRIFT background" in Figure 6.23 is higher than the "REF background" (as expected from the count rates), there seems to be a time dependence in the background signal.

The AGILE team has informed us that there were several AGILE configuration changes in the period between 2016 and 2017. This can be part of the explanation for the observed discrepancies in the background.

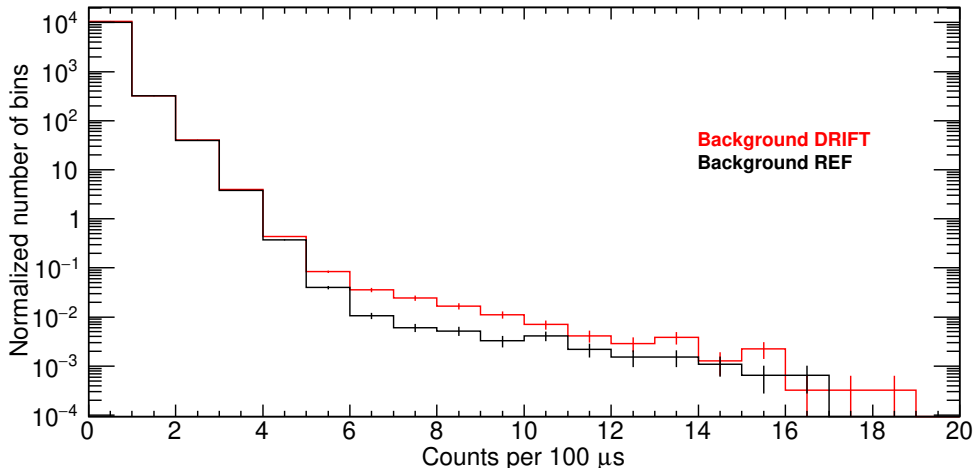


Figure 6.23: Distribution of counts per 100  $\mu\text{s}$  time bin, comparing the backgrounds in the REF dataset with the same season (23.03. - 23.06.2016) in the DRIFT dataset. The REF background is normalized per 0.5 s per 9202 WWLLN detections, and the DRIFT background is normalized per 0.5 s per 6238 WWLLN detections.

As the background in the plots above is taken from  $\delta t$  between 3.2 and 3.7 seconds, this background is dependent on WWLLN detections. To estimate the true background signal, the "distribution of counts per 100  $\mu\text{s}$  bin plot" was calculated for the full MCAL dataset, independent of WWLLN data. That is all MCAL data available. The background plot, for all MCAL data, is shown in Figure 6.24. As expected from the difference in count rates, the DRIFT dataset has more counts per time bin compared with the REF dataset. This means that the DRIFT background in Figure 6.22 is underestimated.

The same season dependent background shown in Figure 6.23, is also apparent in Figure 6.25, where MCAL data for different months in 2016 is plotted. Generally, there are more counts per time bin in the period February-May than June-October, considering counts per time bin between 5 and 20.

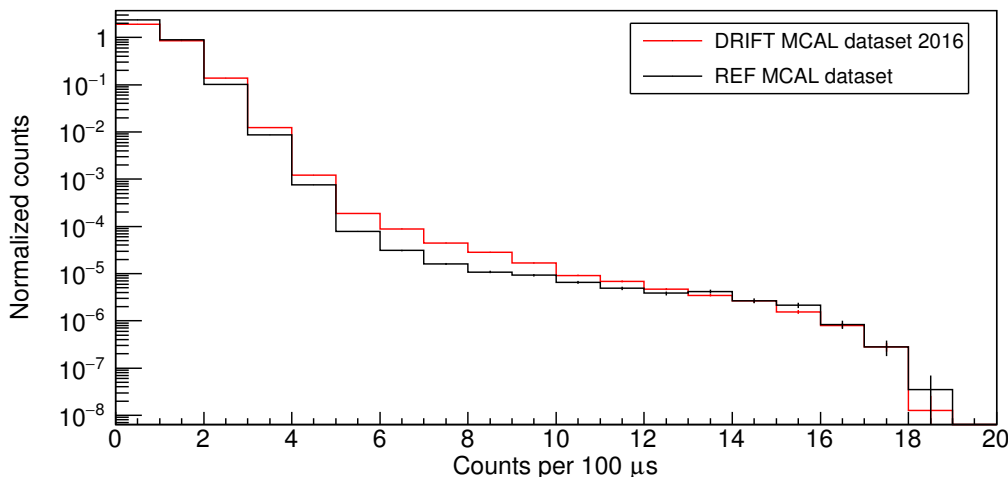


Figure 6.24: Distribution of counts per 100  $\mu\text{s}$  time bin, comparing the full dataset from the DRIFT and REF period. The distributions are normalized per area between 1 and 20.

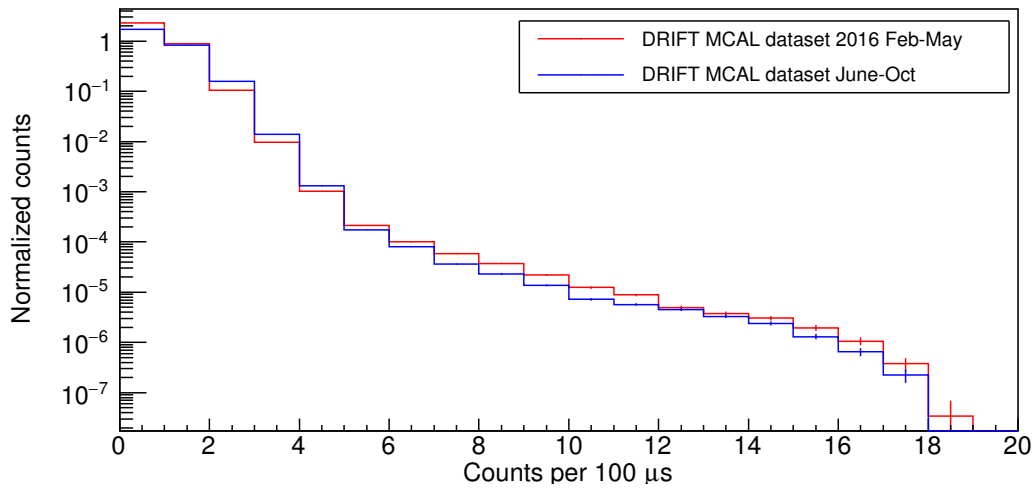


Figure 6.25: Distribution of counts per 100  $\mu\text{s}$  time bin, comparing different month intervals in the DRIFT dataset. The distributions are normalized per area between 1 and 20.

In Figure 6.26, a comparison between the backgrounds in the REF period is shown. The WWLLN dependent background ( $\delta t$  between 3.2 and 3.7 seconds) is shown in blue color, and the full dataset is shown in black color. There is a good agreement between them, meaning that the WWLLN dependent background is a good estimate for the background in the REF period. The discrepancies in counts between 17 and 20 are reasonable, as the full dataset has much more data than the WWLLN-selected one. There were no AGILE configuration changes in the REF period.

In conclusion the observed discrepancies between the background in the REF and DRIFT periods can be associated to: 1) configuration changes, 2) seasonal variability.

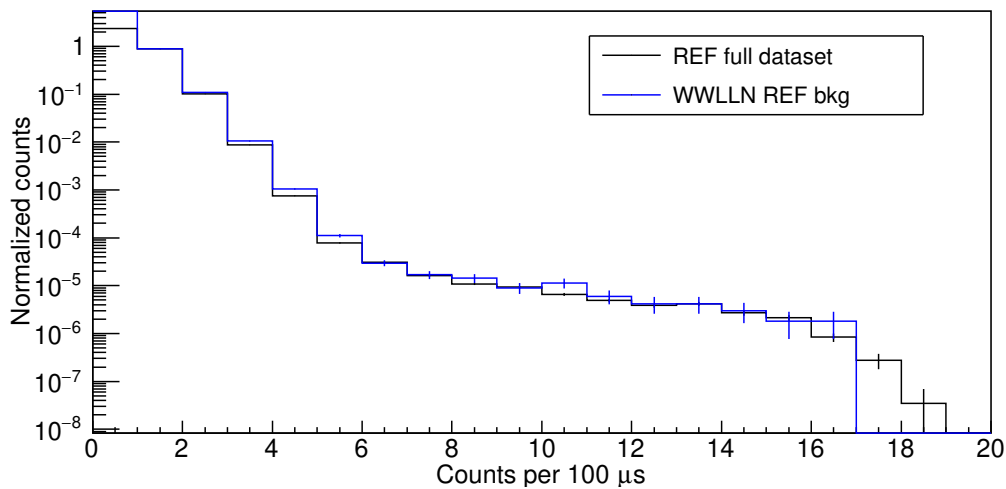


Figure 6.26: A comparison of the WWLLN dependent background and the full REF dataset. The distributions are normalized per area between 1 and 20.

### 6.4.5 Timing offset analysis

For the DRIFT dataset, the  $\delta t$  vs. contact plot is shown in Figure 6.27 and 6.28. The TGF candidates are expected to appear as a straight line with no slope, as for the REF dataset, but with a constant offset due to the AGILE team's time correction algorithm.

In Figure 6.27, some of the contacts in the DRIFT period are shown. Between Contact 46 000 and 48 000, and between 49 000 and 50 000, there are hints of TGF patterns.

In Figure 6.27, especially between Contact 48 000 and 49 000, there is no clear TGF pattern. The reason for this is unknown. The same plot, but with  $|\delta t| \leq 3$ s, shows no TGF pattern. This means that 1) there are no TGFs in this period, which is unlikely, 2) the timing offset is larger than  $\pm 3$ s and the data is not precisely time corrected, 3) the GPS "jumps" to new offsets too often for a clear TGF pattern to appear.

Figure 6.28 is a zoomed view between contacts 49 000 and 50 000, of the events with threshold = 7. The linear structure between Contact 49 200 and 49 800 consists of TGF candidates. Otherwise, we could not explain this correlation feature. The outliers are either background fluctuations, or TGFs with a timing offset forming no clear pattern. A linear fit through the TGF pattern results in a  $\delta t$  change of  $\sim -2$  ms per day. Looking at Figure 6.27, this is the steepest slope.

From Figure 6.28, it is clear that the time drift is not a constant value as expected.

This additional drift was not known prior to this analysis because correlation with WWLLN is a technique much more accurate in terms of timing accuracy, than that based on house-keeping data. The additional time drift partially explains the 20 ms  $\sigma$  observed in Figure 6.20. Figure 6.28 also shows that the TGFs extends beyond the  $\delta t \pm 20$  ms interval considered.

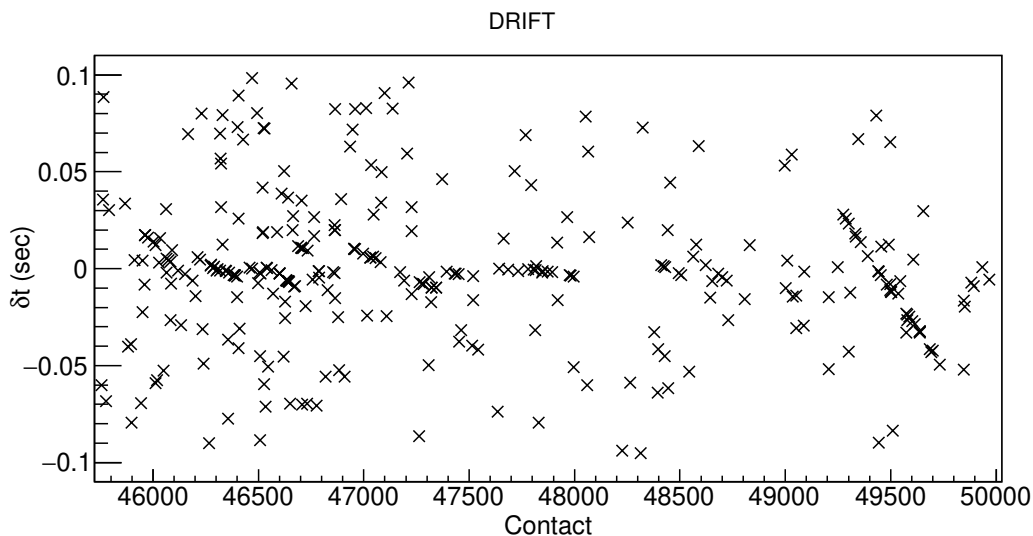


Figure 6.27: Events with threshold = 7.



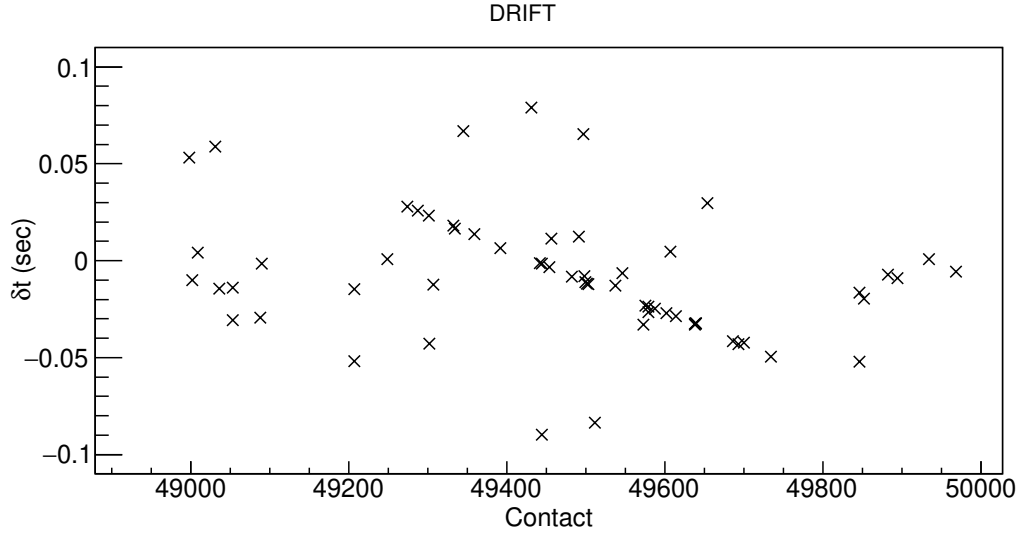


Figure 6.28: Zoomed version of Figure 6.27. Events with threshold = 7. The TGF candidates are visible as a straight line, with a negative slope between Contact 49250 and 49700.

## 6.5 3D-FIX period

This analysis was employed to check the timing accuracy of the AGILE data after the recovery of the GPS, discussed in Section 4.3.5.

The 3D-FIX period dataset is collected by MCAL operated in BURST-mode, with a disabled AC-system. After the DRIFT period, the onboard GPS started partially working again. We analyzed the new MCAL data between 17.01.2018 and 14.04.2018, corrected with the same time correction algorithm as for the DRIFT period.

During this period the WWLLN data includes  $52 \times 10^6$  detections. The WWLLN data associated with MCAL data is shown in Table 6.7. There are 877 147 WWLLN detections in the TGF FOV. (This number is in the same order of magnitude as expected from Section 5.5.) The number of WWLLN detections, which is associated with the MCAL data ( $|\delta t| \leq 100$  ms), is 10 104. This is 1 % of the WWLLN detections in the TGF FOV.

The MCAL observation time is calculated by binning the MCAL data in a histogram with a bin size of 10 ms. The number of filled bins is multiplied by 10 ms to get the total observation time. The bin size of 10 ms is selected as the average count rate is 700 cts/s. In a 10 ms bin, there is an average of 7 counts which gives a low probability of a zero bin when MCAL is observing. The observation time may be overestimated by 1 %.

Table 6.7: WWLLN and MCAL data.

Number of WWLLN detections below satellite	Number of WWLLN detections associated to MCAL	Total MCAL observation time
877 147	10 104	117 783 sec

### 6.5.1 Identifying TGFs using the search for cluster analysis

Selecting a threshold of 6 counts per 100  $\mu\text{s}$  bin, we found 59 TGF candidates using the search for cluster algorithm. The background to signal ratio is 5 % in Figure 6.29. After manually checking the light curve and energy vs. time scatter plots, 57 seem likely to be TGFs. Figure 6.31 also indicates this. The TGF candidates are found in the git repository in the subfolder "Lightcurves/3DFIX".

In Figure 6.30, it is evident that the timing correction is still not accurate.

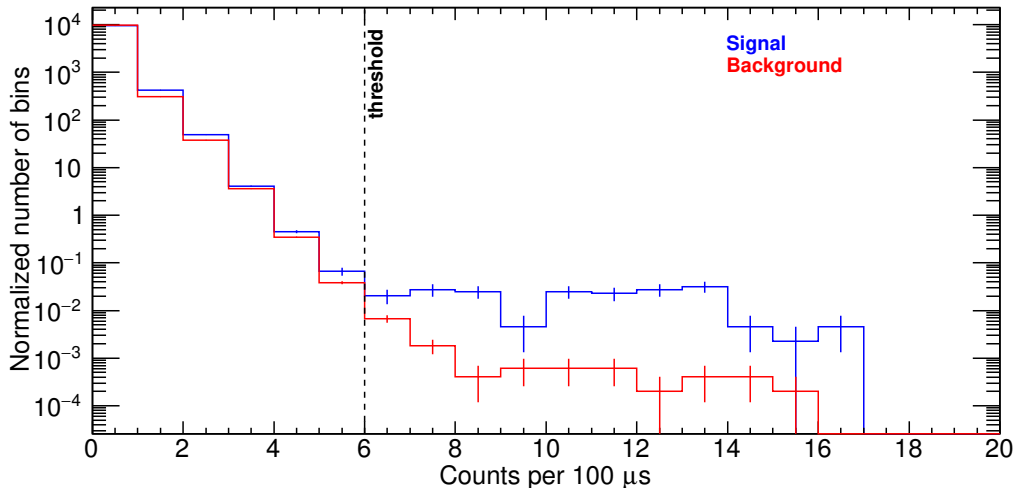


Figure 6.29: Distribution of counts per 100  $\mu\text{s}$  bin. The signal includes counts with  $|\delta t| \leq 20$  ms, and is normalized per 40 ms per 10 104 WWLLN detections. The background includes counts with  $\delta t$  between 3.2 and 3.7 s, and is normalized per 0.5 s per 9842 WWLLN detections.

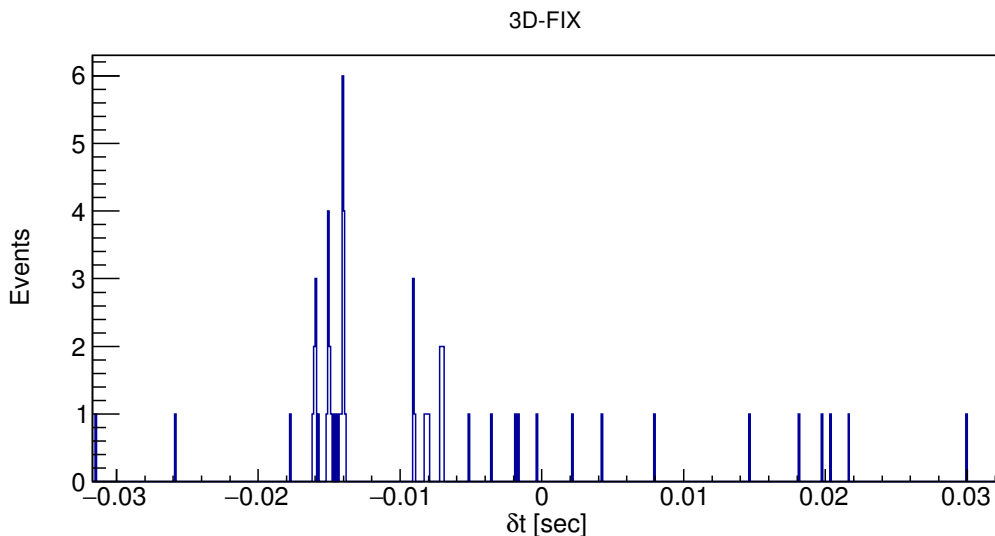


Figure 6.30: Events with threshold = 6. There are 59 TGF candidates between  $-20$  and  $20$  ms. The bin size is  $100 \mu\text{s}$ .

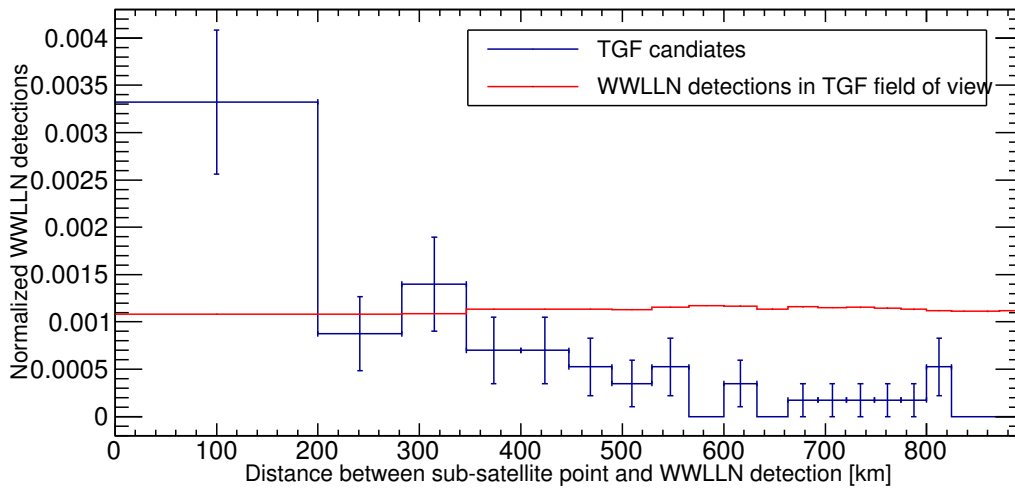


Figure 6.31: Number of TGF candidates, as a function of distance from the sub-satellite point to WWLLN detection, and all the WWLLN detections in the TGF FOV. Each distribution is normalized to 1.

### 6.5.2 Timing offset analysis

The 3D-FIX period is corrected using housekeeping data, meaning this correction has both an integer part and a fractional millisecond part. The average  $\Delta t$  (see Figure 4.3) is calculated as long as the offset is approximately constant. In Figure 6.32, the TGF candidates form a straight line at  $\delta t \approx 0$  with a constant offset, then "jumps" to a new offset. This is particularly clear for the contacts before and after Contact 56 800.

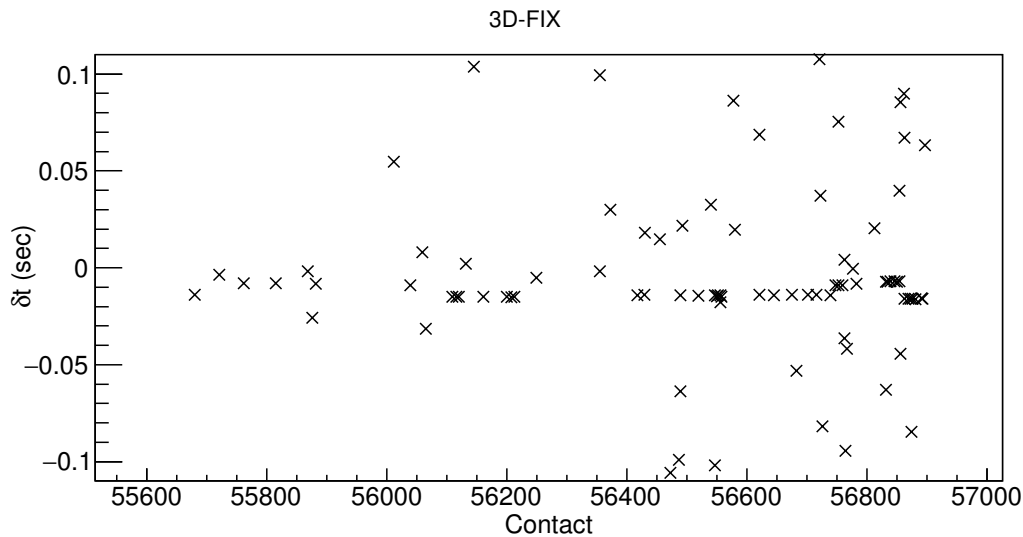


Figure 6.32: Events with threshold = 6

After the recovery of the GPS, the fractional onboard time is back to the accuracy of the REF period, so the timing offset correction should only be corrected using the integer part. As Figure 6.32 is corrected both for the integer and fractional  $\Delta t$ , we need to subtract the fractional correction from  $\Delta t$ .

We received the file used to correct the timing offset using housekeeping data, and reversed

the fractional offset correction, by subtracting the millisecond offset correction from the data. This results in correcting only the integer part, meaning the time correction is done properly as shown in Figure 6.33, 6.34 and 6.35. We conclude that this corrects the data timestamps, leaving only a systematic offset of  $\sim 4$  ms.

The standard deviation of the peak is  $\sigma = 81 \mu\text{s}$  which is compatible to the  $60 \mu\text{s}$  in the REF period. If the data is corrected for the 4 ms systematic error, the timing accuracy is comparable to the REF period as long as the onboard GPS behaves this way.

When we correct the 4 ms systematic error, we find that only 39 of the 57 TGF candidates have  $|\delta t| \leq 500 \mu\text{s}$ . The 18 TGF candidates left have clear TGF signatures in the lightcurve and energy vs. time scatter plots. The 18 TGF candidates has WWLLN matches with  $\delta t$  between a few ms to 55 ms.

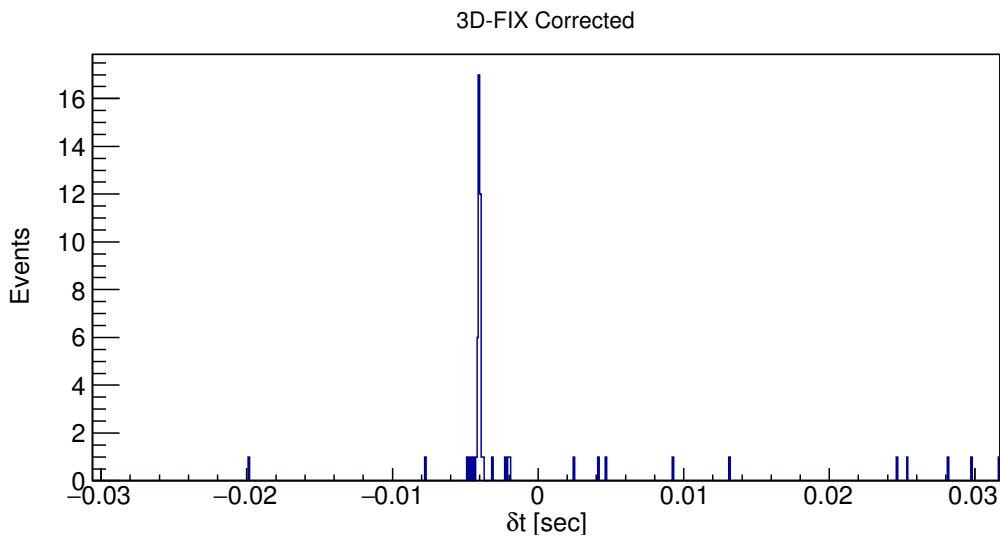


Figure 6.33: Events with threshold = 6. The bin size is  $100 \mu\text{s}$ .

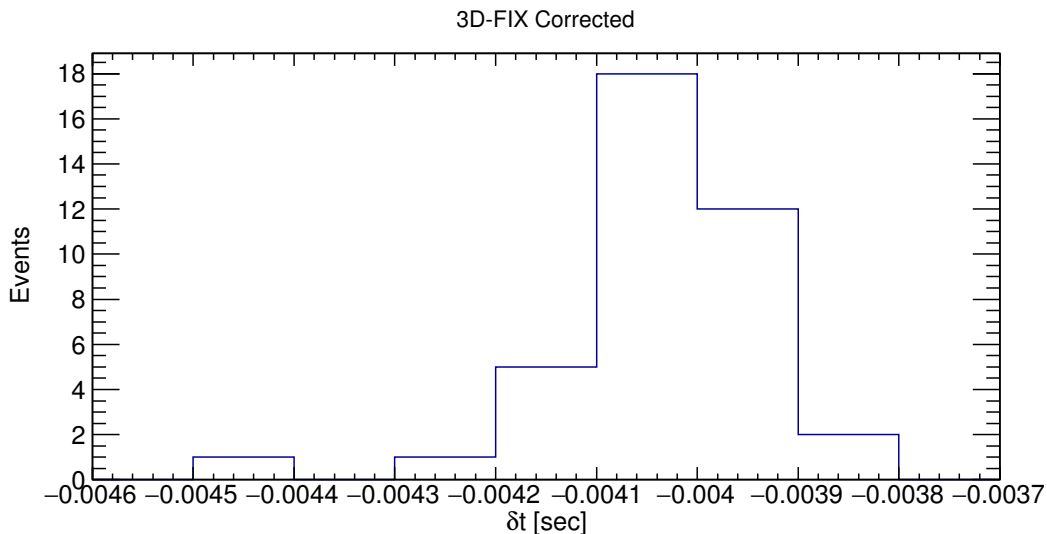


Figure 6.34: 39 events with threshold = 6. The bin size is  $100 \mu\text{s}$ . A Gaussian fit gives a mean  $\delta t = -4.033$  ms, and a sigma of  $\sigma = 81 \mu\text{s}$ .

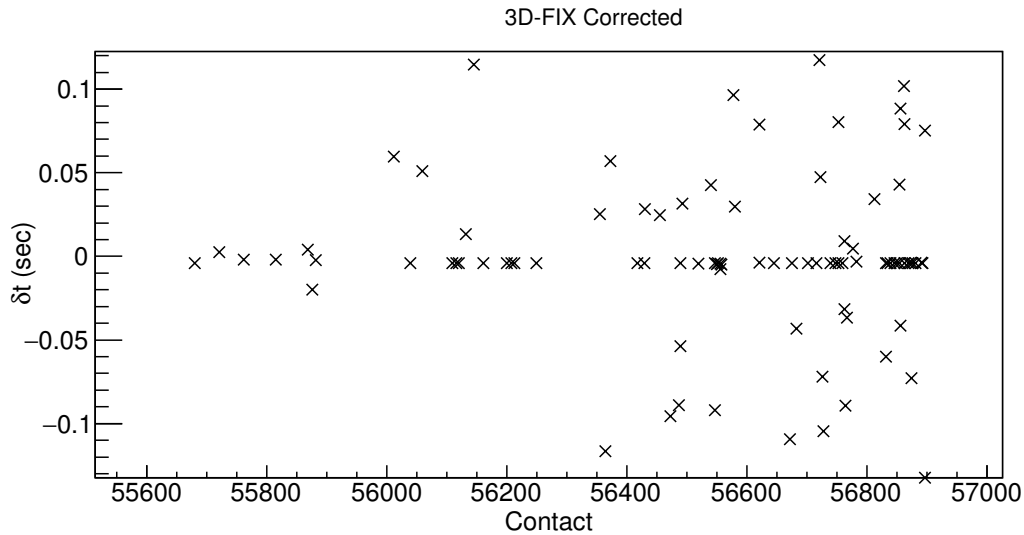


Figure 6.35: TGF candidates with threshold larger than 6 counts per 100  $\mu$ s bin.

## 6.6 Global and monthly distribution of all TGF candidates

A global map of all the WWLLN detections, associated with the TGF candidates, is shown in Figure 6.37. The "TGF belt" clearly shows the inclination angle of AGILE, ( $\pm 2.5^\circ$ ). We do not see TGF candidates with a higher and lower latitude as AGILE do not cover these areas. The longitude distribution of these TGF candidates is shown in Figure 6.36. The TGF candidates are mostly detected in Indonesia, Africa and the Central America, in decreasing order. There are some TGF candidates occurring over the ocean.

Figure 6.38 shows the number of TGF candidates per month between March 2015 and April 2014.

These distributions are consistent with the general characteristics of TGFs.

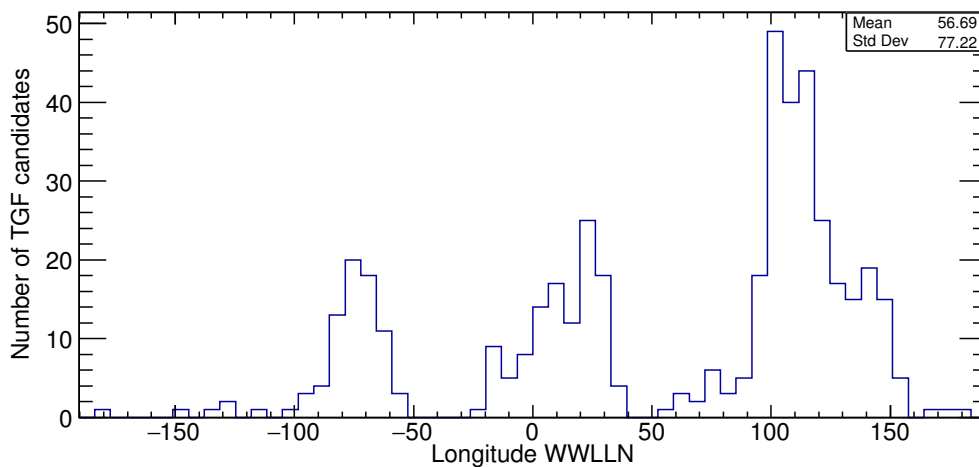


Figure 6.36: Longitude distribution of the WWLLN detections associated with the TGF candidates.

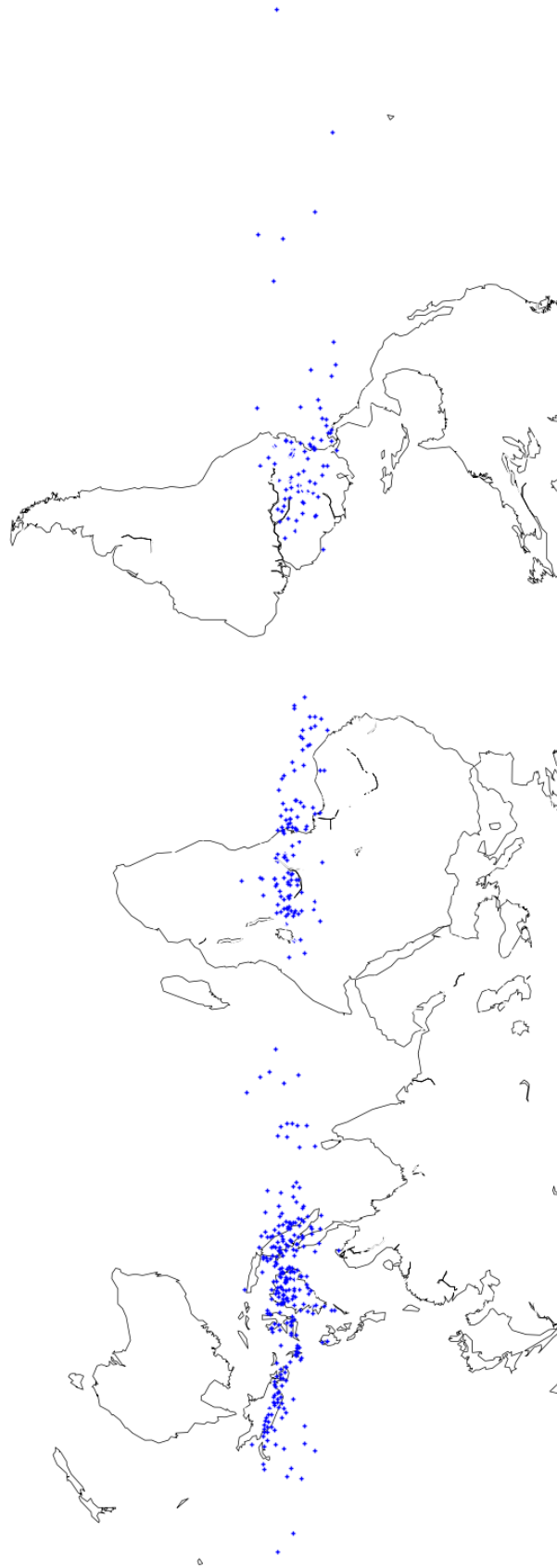


Figure 6.37: Latitude and longitude of WWLLN detections associated with the TGF candidates. Note that the inclination angle of AGILE is  $\pm 2.5^\circ$ .

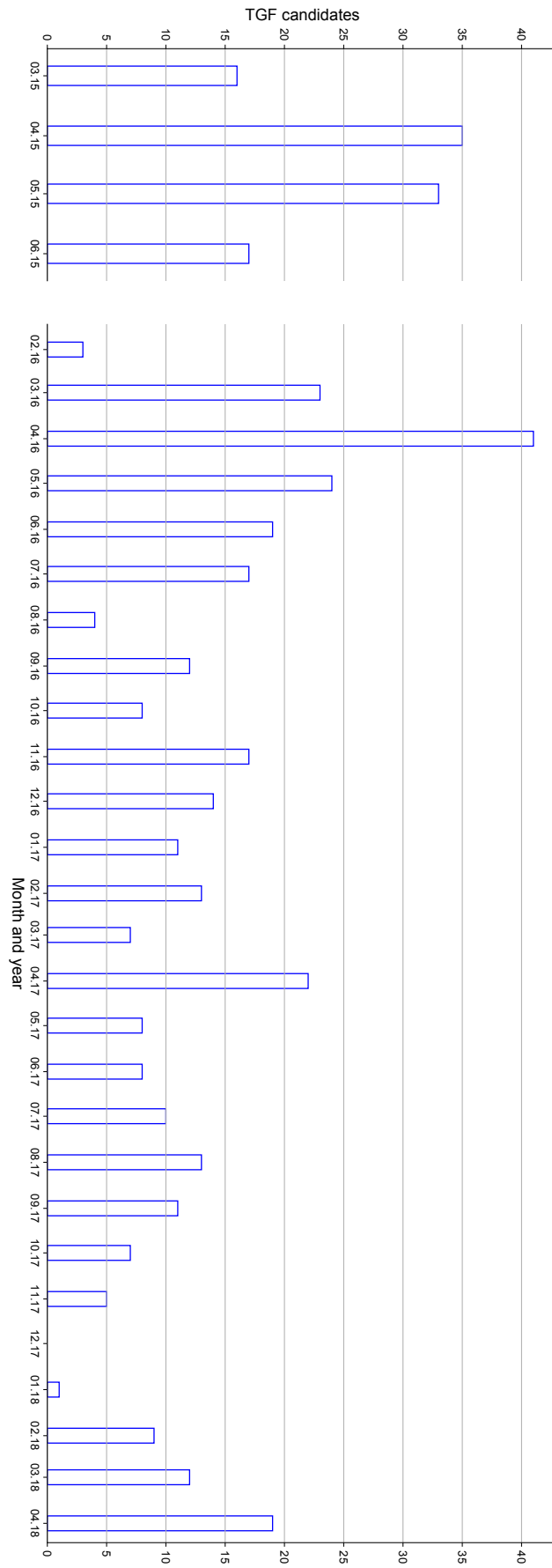


Figure 6.38: Monthly distribution of all the TGF candidates. Note that between 24.06.15 - 01.01.16, and 09.11.17 - 17.01.18, there are no data analyzed.





# Chapter 7

## Summary and Outlook

In this thesis we have applied a systematic search for TGFs, based on correlation between WWLLN sferics and counts detected by AGILE. A dedicated algorithm was specifically designed within the work of this thesis, in order to identify candidate TGFs in datasets with varying systematic timing offset. A total of 439 TGF candidates are identified (43 of these were already identified by *Marisaldi et al.* [2015]). A summary of the TGF candidates is found in Table 7.1.

No TGF candidates were identified in the GRID and AC-ON period when the AC-system was active on both GRID and MCAL. This confirms that the AC-system prevents the detection of TGFs associated to sferics.

In the REF period (AC-system disabled for MCAL, timing resolution of 2  $\mu$ s), 100 TGF candidates were identified. When counts for these 100 TGFs are removed from the dataset, there is no significant TGF signal left (Figure 6.12), concluding that most WWLLN sferics associated with TGFs are identified in the dataset. A double TGF was identified in Figure 6.16, and in agreement with *Mezentsev et al.* [2016], the WWLLN sferic is associated with the last TGF peak. The TGF-lightning ratio is in the order of  $10^{-4}$ , in agreement with *Briggs et al.* [2013].

In the DRIFT period (AC-system disabled, timing resolution of  $\sim$  ms), 300 TGF candidates were identified by the dedicated search for clusters analysis. It was known, and corrected for by the AGILE team, that the onboard time had a varying, systematic timing offset. However, this analysis discovered that there is an additional time drift (Figure 6.28). This was not known before this analysis. The pattern in the offset is sometimes not visible. The reason for this is unknown, but three explanations are suggested: 1) there are no TGFs in this period (which is unlikely), 2) timing offset is larger than  $\pm 3$ s, 3) timing offset changes too often for a clear TGF pattern to appear.

Table 7.1: Summary of the results from the different AGILE datasets.

Dataset	Date	Number of TGF candidates	Minimum counts per 100 $\mu$ s
GRID	01.06.2008 - 23.06.2015	0	n/a
AC-ON	17.01.2008 - 22.03.2015	0	n/a
REF	23.03.2015 - 23.06.2015	100	4
DRIFT	01.01.2016 - 09.11.2017	300	7
3D-FIX	17.01.2018 - 14.04.2018	39	6

When there is a clear drift pattern, the correlation between TGFs and WWLLN sferics can be used to correct AGILE's onboard time during the corresponding period.

In the 3D-FIX period (AC system disabled, GPS working properly but onboard time is still affected by a systematic drift), 39 TGF candidates were identified. These were successfully used to correct the accuracy of AGILE's onboard time from several ms to  $\sim 100 \mu\text{s}$  accuracy. As these satellite data also are used to study other phenomena, like gamma-ray bursts associated to gravitational waves [Verrecchia et al., 2017], high timing accuracy in the dataset is of utmost importance.

This study can be the starting point of several investigations, listed below:

1. The study has identified new TGFs, associated with WWLLN sferics, that have been overlooked by previous selection criteria algorithms. This shows that previous selection criteria are too strict and then are excluding several TGFs. A study should be performed, adjusting, and maybe finding new selection criteria, which includes the previously excluded TGFs. An attempt to use machine learning to recognize TGFs in the satellite data could be performed in addition to adjusting traditional selection criteria.
2. As AGILE's onboard time, since July 2015, is drifting, new TGFs associated with WWLLN should routinely be identified in new AGILE data, correcting future timing offsets. A Gaussian distribution should be fitted to every TGF to find the best estimation of the TGF arrival time ( $time_{satellite}$  in Equation 5.9), replacing the rather crude estimate of  $\sim 100 \mu\text{s}$  accuracy, described in Section 5.4.
3. A direction reconstruction of the GRID photon associated with the TGF, identified by MCAL in the REF period, could be calculated (Section 6.1.3). If the photon is associated with the TGF, it should be traced back to approximately the same latitude and longitude as the associated WWLLN sferic.
4. The  $3\sigma$  significant signal in the AC-ON stackplot (Figure 6.6), should be investigated further, as it may be due to counts associated with the early stage of TGFs before the AC-system suppresses the largest part of the signal.

# Bibliography

- Abarca, S. F., K. L. Corbosiero, and T. J. Galarneau Jr (2010), An evaluation of the Worldwide Lightning Location Network (WWLLN) using the National Lightning Detection Network (NLDN) as ground truth, *J. Geophys. Res.*, *115*, D18,206, doi:10.1029/2009JD013411.
- Bowers, G. S., D. M. Smith, N. A. Kelley, S. A. Cummer, J. R. Dwyer, et al. (2018), A Terrestrial Gamma-Ray Flash inside the Eyewall of Hurricane Patricia, *J. Geophys. Res. Atmos.*, *123*, doi:10.1029/2017JD027771.
- Briggs, M. S., et al. (2010), First results on terrestrial gamma ray flashes from the Fermi Gamma-ray Burst Monitor, *J. Geophys. Res.*, *115*, A07,323, doi:10.1029/2009JA015242.
- Briggs, M. S., et al. (2013), Terrestrial gamma-ray flashes in the Fermi era: Improved observations and analysis methods, *J. Geophys. Res. Space Physics*, *118*, 3805–3830, doi:10.1002/jgra.50205.
- Bürgesser, R. E. (2017), Assessment of the World Wide Lightning Location Network (WWLLN) detection efficiency by comparison to the Lightning Imaging Sensor (LIS), *Q. J. R. Meteorol. Soc.*, *143*, 2809–2817, doi:10.1002/qj.3129.
- Carlson, B. E., N. G. Lehtinen, and U. S. Inan (2007), Constraints on terrestrial gamma ray flash production from satellite observation, *Geophys. Res. Lett.*, *34*(8), 1–5, doi:10.1029/2006GL029229.
- Celestin, S., and V. P. Pasko (2011), Energy and fluxes of thermal runaway electrons produced by exponential growth of streamers during the stepping of lightning leaders and in transient luminous events, *J. Geophys. Res. Sp. Phys.*, *116*, doi:10.1029/2010JA016260.
- Cohen, M. B., U. S. Inan, R. K. Said, and T. Gjestland (2010), Geolocation of terrestrial gamma-ray flash source lightning, *Geophys. Res. Lett.*, *37*, doi:10.1029/2009GL041753.
- Coleman, L. M., and J. R. Dwyer (2006), Propagation speed of runaway electron avalanches, *Geophys. Res. Lett.*, *33*, doi:10.1029/2006GL025863.
- Collier, A. B., T. Gjestland, and N. Østgaard (2011), Assessing the power law distribution of TGFs, *J. Geophys. Res.*, *116*, A10,320, doi:10.1029/2011JA016612.
- Connaughton, V., et al. (2010), Associations between Fermi Gamma-ray Burst Monitor terrestrial gamma ray flashes and sferics from the World Wide Lightning Location Network, *J. Geophys. Res.*, *115*, doi:10.1029/2010JA015681.
- Connaughton, V., et al. (2013), Radio signals from electron beams in terrestrial gamma ray flashes, *J. Geophys. Res. Space Physics*, *118*, 2313–2320, doi:10.1029/2012JA018288.
- Cummer, S. A., Y. Zhai, W. Hu, D. M. Smith, L. I. Lopez, and M. A. Stanley (2005), Measurements and implications of the relationship between lightning and terrestrial gamma ray flashes, *Geophys. Res. Lett.*, *32*, doi:10.1029/2005GL022778.

- Cummer, S. A., G. Lu, M. S. Briggs, V. Connaughton, S. Xiong, G. J. Fishman, and J. R. Dwyer (2011), The lightning-TGF relationship on microsecond timescales, *Geophys. Res. Lett.*, *38*, L14,810, doi:10.1029/2011GL048099.
- Cummer, S. A., M. S. Briggs, J. R. Dwyer, S. Xiong, V. Connaughton, G. J. Fishman, G. Lu, F. Lyu, and R. Solanki (2014), The source altitude, electric current, and intrinsic brightness of terrestrial gamma ray flashes, *Geophysical Research Letters*, *41*(23), doi:10.1002/2014GL062196.
- Dowden, R. L., J. B. Brundell, and C. J. Rodger (2002), VLF lightning location by time of group arrival (TOGA) at multiple sites, *Journal of Atmospheric and Solar-Terrestrial Physics*, *64*, 817–830, doi:https://doi.org/10.1016/S1364-6826(02)00085-8.
- Dwyer, J. R. (2003), A fundamental limit on electric fields in air, *Geophys. Res. Lett.*, *30*(20), doi:10.1029/2003GL017781.
- Dwyer, J. R. (2008), Source mechanisms of terrestrial gamma-ray flashes, *J. Geophys. Res.*, *113*, doi:10.1029/2007JD009248.
- Dwyer, J. R., and D. M. Smith (2005), A comparison between monte carlo simulations of runaway breakdown and terrestrial gamma-ray flash observations, *Geophysical Research Letters*, *32*, doi:10.1029/2005GL023848.
- Dwyer, J. R., D. M. Smith, and S. A. Cummer (2012), High-energy atmospheric physics: Terrestrial gamma-ray flashes and related phenomena, *Space Sci. Rev.*, *173*, 133–196, doi:10.1007/s11214-012-9894-0.
- ESA (Accessed 20.05.2018), Iss utilization: Asim (atmosphere-space interactions monitor), url = <https://earth.esa.int/web/eoportal/satellite-missions/i/iss-asim>.
- Fishman, G., et al. (2011), Temporal properties of terrestrial gamma-ray flashes from the Gamma-Ray Burst Monitor on the Fermi Observatory, *J. Geophys. Res.*, *116*, doi:10.1029/2010JA016084.
- Fishman, G. J., et al. (1994), Discovery of intense gamma-ray flashes of atmospheric origin., *Science (New York, N.Y.)*, *264*(5163), 1313–1316, doi:10.1126/science.264.5163.1313.
- Gjesteland, T., N. Østgaard, P. H. Connell, J. Stadsnes, and G. J. Fishman (2010), Effects of dead time losses on terrestrial gamma ray flash measurements with the Burst and Transient Source Experiment, *J. Geophys. Res.*, *115*, doi:10.1029/2009JA014578.
- Gjesteland, T., N. Østgaard, a. B. Collier, B. E. Carlson, C. Eyles, and D. M. Smith (2012), A new method reveals more TGFs in the RHESSI data, *Geophysical Research Letters*, *39*(5), doi:10.1029/2012GL050899.
- Grefenstette, B. W., D. M. Smith, B. J. Hazelton, and L. I. Lopez (2009), First RHESSI terrestrial gamma ray flash catalog, *J. Geophys. Res.*, *114*, A02,314, doi:10.1029/2008JA013721.
- Gurevich, A. V., G. M. Milikh, and R. Roussel-Dupre (1992), Runaway electron mechanism of air breakdown and preconditioning during a thunderstorm, *Phys. Lett. A*, *165*, 463–468, doi:10.1016/0375-9601(92)90348-P.
- Hare, B. M., et al. (2016), Ground-level observation of a terrestrial gamma ray flash initiated by a triggered lightning, *Journal of Geophysical Research: Atmospheres*, *121*, 6511–6533, doi:10.1002/2015JD024426.

- Hutchins, M. L., R. H. Holzworth, J. B. Brundell, and C. J. Rodger (2012), Relative detection efficiency of the world wide lightning location network, *Radio Science*, *47*(6), n/a–n/a, doi:10.1029/2012RS005049, rS6005.
- Hutchins, M. L., R. H. Holzworth, K. S. Virts, J. M. Wallace, and S. Heckman (2013), Radiated vlf energy differences of land and oceanic lightning, *Geophysical Research Letters*, *40*(10), 2390–2394, doi:10.1002/grl.50406.
- Inan, U. S., S. C. Reising, G. J. Fishman, and J. M. Horack (1996), On the association of terrestrial gamma-ray bursts with lightning and implications for sprites, *23*(9), 1017–1020, doi:https://doi.org/10.1029/96GL00746.
- Inan, U. S., M. B. Cohen, R. K. Said, D. M. Smith, and L. I. Lopez (2006), Terrestrial gamma ray flashes and lightning discharges, *Geophys. Res. Lett.*, *33*(18), doi:10.1029/2006GL027085.
- Jayarathne, E. R., C. P. R. Saunders, and J. Hallett (1983), Laboratory studies of the charging of soft hail during ice crystal interactions, *Quarterly Journal of the Royal Meteorological Society*, *109*, 609–630, doi:10.1002/qj.49710946111.
- Karwasz, G. P., M. Barozzi, R. S. Brusa, and A. Zecca (2002), Total cross sections for positron scattering on argon and krypton at intermediate and high energies, *Nuclear Instruments and Methods in Physics Research Section B: Beam Interactions with Materials and Atoms*, *192*(1), 157 – 161, doi:https://doi.org/10.1016/S0168-583X(02)00857-1.
- Labanti, C., et al. (2009), Design and construction of the mini-calorimeter of the agile satellite, *Nuclear Instruments and Methods in Physics Research Section A: Accelerators, Spectrometers, Detectors and Associated Equipment*, *598*(2), 470 – 479, doi:https://doi.org/10.1016/j.nima.2008.09.021.
- Lu, G., et al. (2010), Lightning mapping observation of a terrestrial gamma-ray flash, *Geophys. Res. Lett.*, *37*, doi:10.1029/2010GL043494.
- Mallick, S., et al. (2014), Evaluation of the WWLLN Performance Characteristics Using Rocket-Triggered Lightning Data, *International Conference on Grounding and Earthing and 6th International Conference on Lightning Physics and Effects, Manaus Brazil*.
- Marisaldi, M., et al. (2010a), Detection of terrestrial gamma ray flashes up to 40 MeV by the AGILE satellite, *J. Geophys. Res.*, *115*, A00E13, doi:10.1029/2009JA014502.
- Marisaldi, M., et al. (2010b), Gamma-Ray Localization of Terrestrial Gamma-Ray Flashes, doi:10.1103/PhysRevLett.105.128501.
- Marisaldi, M., et al. (2013), Terrestrial gamma-ray flashes, *Nuclear Instruments and Methods in Physics Research*, *720*, 83–87, doi:10.1016/j.nima.2012.12.029.
- Marisaldi, M., et al. (2014), Properties of terrestrial gamma ray flashes detected by AGILE MCAL below 30 MeV, *J. Geophys. Res. Space Physics*, *119*, 1337–1355, doi:10.1002/2013JA019301.Received.
- Marisaldi, M., et al. (2015), Enhanced detection of terrestrial gamma-ray flashes by agile, *Geophysical Research Letters*, *42*(21), 9481–9487, doi:10.1002/2015GL066100.
- Marisaldi, M., et al. (2018), Implications for Terrestrial Gamma-ray Flashes spectrum, flux and fine time structure at source based on the high-energy events observed by AGILE, *EGU, Vienna, April 2018*.

- McTague, L. E., S. A. Cummer, M. S. Briggs, V. Connaughton, M. Stanbro, and G. Fitzpatrick (2015), A lightning-based search for nearby observationally dim terrestrial gamma ray flashes, *J. Geophys. Res. Atmos.*, *120*, doi:10.1002/2015JD023475.
- Meegan, C., et al. (2009), The fermi gamma-ray burst monitor, *Astrophys. J.*, *702*, 791–804, doi:10.1088/0004-637X/702/1/791.
- Mezentsev, A., N. Østgaard, T. Gjesteland, K. Albrechtsen, N. Lehtinen, M. Marisaldi, D. Smith, and S. Cummer (2016), Radio emissions from double RHESSI TGFs, *J. Geophys. Res. Atmos.*, *121*, doi:10.1002/2016JD025111.
- Moss, G. D., V. P. Pasko, N. Liu, and G. Veronis (2006), Monte Carlo model for analysis of thermal runaway electrons in streamer tips in transient luminous events and streamer zones of lightning leaders, *Journal of Geophysical Research*, *111*(2), 1–37, doi:10.1029/2005JA011350.
- NASA (Accessed 14.05.2018), Batse triggers, url = <https://gammaray.nsstc.nasa.gov/batse/misc/triggers.html>.
- Østgaard, N., T. Gjesteland, R. S. Hansen, a. B. Collier, and B. Carlson (2012), The true fluence distribution of terrestrial gamma flashes at satellite altitude, *J. Geophys. Res.*, *117*, A03,327, doi:10.1029/2011JA017365.
- Østgaard, N., T. Gjesteland, B. E. Carlson, A. B. Collier, S. A. Cummer, G. Lu, and H. J. Christian (2013), Simultaneous observations of optical lightning and terrestrial gamma ray flash from space, *Geophys. Res. Lett.*, *40*, doi:10.1002/grl.50466.
- Østgaard, N., K. H. Albrechtsen, T. Gjesteland, and A. Collier (2015), A new population of terrestrial gamma-ray flashes in the RHESSI data, *Geophys. Res. Lett.*, *42*, doi:10.1002/2015GL067064.
- Preece, R. D., M. S. Briggs, R. S. Mallozzi, G. N. Pendleton, W. S. Paciesas, and D. L. Band (1999), The BATSE Gamma-Ray Burst Spectral Catalog. I. High Time Resolution Spectroscopy of Bright Bursts using High Energy Resolution Data, doi:10.1086/313289.
- Raizer, Y. P. (1991), *Gas Discharge Physics*, Springer-Verlag, Berlin Heidelberg Germany.
- Rakov, V. A., and M. A. Uman (2003), *Lightning: Physics and Effects*, The Press Syndicate of the University of Cambridge, The Pitt Building, Trumpington Street, Cambridge, United Kingdom.
- Roberts, O. J., et al. (2018), The First Fermi-GBM Terrestrial Gamma-ray Flash Catalog, *Journal of Geophysical Research: Space Physics*, doi:10.1029/2017JA024837.
- Rudlosky, S. D., and D. T. Shea (2013), Evaluating WWLLN performance relative to TRMM/LIS, *Geophys. Res. Lett.*, *40*, 2344–2348, doi:10.1002/grl.50428.
- Segre, E. (1965), *Nuclei and Particles, An Introduction to Nuclear and Subnuclear Physics*, W.A. Benjamin, INC., New York.
- Shao, X. M., T. Hamlin, and D. M. Smith (2010), A closer examination of terrestrial gamma-ray flash-related lightning processes, *J. Geophys. Res.*, *115*, doi:10.1029/2009JA014835.
- Skeltved, A. B. (2018), Evaluating production scenarios of terrestrial gamma-ray flashes, Ph.D. thesis, University of Bergen.
- Skeltved, A. B., N. Østgaard, B. Carlson, and T. Gjesteland (2014), A study of the

- runaway relativistic electron avalanche and the feedback theory using GEANT4, *119*, 9174–9191, doi:doi:10.1002/2014JA020504.
- Skogseide, Y., et al. (2012), BGO Front-End Electronics and Signal Processing in the MXGS Instrument for the ASIM Mission, in *Conf. Rec. - IEEE Instrum. Meas. Technol. Conf.*, doi:10.1109/I2MTC.2012.6229186.
- Smith, D. M., et al. (2002), The RHESSI spectrometer, *Solar Physics*, *210*(1-2), 33–60, doi:10.1023/A:1022400716414.
- Smith, D. M., L. I. Lopez, R. P. Lin, and C. P. Barrington-Leigh (2005), Terrestrial Gamma-Ray Flashes Observed up to 20 MeV, *Science*, *307*(5712), 1085–1088, doi:10.1126/science.1107466.
- Smith, D. M., et al. (2011), The rarity of terrestrial gamma-ray flashes, *Geophys. Res. Lett.*, *38*, L08,807, doi:10.1029/2011GL046875.
- Smith, D. M., P. Buzbee, N. Kelley, A. Infanger, R. H. Holzworth, and J. R. Dwyer (2016), The rarity of terrestrial gamma-ray flashes: 2. RHESSI stacking analysis, *J. Geophys. Res. Atmos.*, *121*, doi:10.1002/2016JD025395.
- Takahashi, T. (1978), Riming electrification as a charge generation mechanism in thunderstorms, *Journal of the Atmospheric Sciences*, *35*, 1536–1548, doi:10.1175/1520-0469(1978)035<1536:REAACG>2.0.CO;2.
- Tavani, M., et al. (2009), The AGILE Mission, *Astronomy and Astrophysics*, *502*, 995–1013, doi:https://doi.org/10.1051/0004-6361/200810527.
- Tavani, M., et al. (2011), Terrestrial gamma-ray flashes as powerful particle accelerators, *Phys. Rev. Lett.*, *106*, doi:10.1103/PhysRevLett.106.018501.
- Tran, M. D., V. A. Rakov, S. Mallick, J. R. Dwyer, A. Nag, and S. Heckman (2015), A terrestrial gamma-ray flash recorded at the Lightning Observatory in Gainesville, Florida, *J. Atmos. Solar-Terrestrial Phys.*, *136*, doi:10.1016/j.jastp.2015.10.010.
- Ursi, A., C. Guidorzi, M. Marisaldi, D. Sarria, and F. Frontera (2017), Terrestrial gamma-ray flashes in the BeppoSAX data archive, *Journal of Atmospheric and Solar-Terrestrial Physics*, doi:10.1016/j.jastp.2017.02.014.
- Verrecchia, F., et al. (2017), AGILE Observations of the Gravitational-wave Source GW170817: Constraining Gamma-Ray Emission from an NS–NS Coalescence, *The Astrophysical Journal Letters*, doi:https://doi.org/10.3847/2041-8213/aa965d.
- Williams, E. R. (1989), The tripole structure of thunderstorms, *Journal of Geophysical Research: Atmospheres*, *94*(D11), 13,151–13,167, doi:10.1029/JD094iD11p13151.
- Wilson, C. (1924), The electric field of a thundercloud and some of its effects, *Proc. Phys. Soc. London*, *37*, 32D–37D.